2022

From interparticle interactions to emergent behavior of smart fluids

BOSTON UNIVERSITY

COLLEGE OF ENGINEERING

Dissertation

FROM INTERPARTICLE INTERACTIONS TO EMERGENT BEHAVIOR OF SMART FLUIDS

by

ABIGAIL RENDOS

B.S., Boston University, 2017
M.S., Boston University, 2021

Submitted in partial fulfillment of the

requirements for the degree of

Doctor of Philosophy

2022

Approved by

First Reader

Keith A. Brown, Ph.D.
Assistant Professor of Mechanical Engineering
Assistant Professor of Materials Science and Engineering
Assistant Professor of Physics

Second Reader

Tommaso Ranzani, Ph.D.
Assistant Professor of Mechanical Engineering
Assistant Professor of Materials Science and Engineering
Assistant Professor of Biomedical Engineering

Third Reader

Mark W. Grinstaff, Ph.D.
Distinguished Professor of Translational Research
Professor of Biomedical Engineering
Professor of Chemistry
Professor of Materials Science and Engineering
Professor of Medicine

Fourth Reader

Xi Ling, Ph.D.
Assistant Professor of Chemistry

ACKNOWLEDGEMENTS

First, I would like to express my thanks to my PhD Advisor, Professor Keith Brown, for his support, guidance, and mentorship. I joined the KABlab in Professor Brown's first semester at Boston University as an undergraduate student, stayed for my PhD, and have immensely enjoyed watching the lab grow and produce excellent research under Professor Brown's leadership. His creativity and passion for research are what makes the KABlab a flourishing and productive group. Professor Brown, along with my undergraduate advisor Professor Greg McDaniel and lab (and life) mentor Dr. Nourin Alsharif, were my main supporters in pursuing a graduate degree, and I would not have applied without their belief in my research ability.

I would like to thank each of my committee members, Professor Tommaso Ranzani, Professor Xi Ling, and Professor Mark Grinstaff, for their advice and feedback throughout my PhD. Each of you served an important role in the completion of this degree, whether through collaboration or project support, and I greatly appreciate your help.

Next, a huge thank you to all of our collaborators including Professor Ranzani, Kevin McDonald, Professor Ling, Ran Li, Professor Allison Dennis, Dr. Peggy Chern, Professor Rob Macfarlane, and Dr. Daryl Yee without which many of the projects in this dissertation would not have been possible. Working with such a broad range of scientists was one of the highlights of my PhD and so I am incredibly grateful for all the engaging projects that resulted from these collaborations.

I would like to thank the past and current members of the KABlab that have not only helped in research, but also helped keep me sane: Dr. Nourin Alsharif, Dr. Le Li, Dr.

Wenhan Cao, Dr. Aldair Gongora, Verda Saygin, Stephanie Woodman, Brian Kim, Kelsey Snapp, and Harley Quinn. In particular, thank you to Aldair and Verda for everything, I am so lucky to have met both of you and spent my graduate school days with the two of you. Also, I want to give a special thanks to my cohort from the MSE division, including Michelle, Karthika, Ben, Peco, and Wes, who were an amazing support system throughout graduate school and the past and current members of the GWISE board who were a pleasure to work with and made my time outside of lab so enjoyable.

Next, I am thankful for all the staff at BU that either trained me on equipment or maintained the lab spaces which were essential to my work. Specifically, thank you to Paul Mak, Dr. Xin Brown, Anlee Krupp, and all the custodial staff that worked throughout these two years of COVID to keep our work space as safe as possible. I also really appreciate the support from the BU Nanotechnology Fellows and program directors, Brenda Hugot and Professor Grinstaff, for the wonderful opportunity to be a part of this fellowship. Thank you to the MSE division staff, including Ruth Mason & Elizabeth Flagg, who have been not only immensely helpful, but very kind and understanding admins for our division. A special thanks to Elizabeth Flagg for enabling me to meet and adopt Donut, I can't imagine what these last couple years of grad school would have been like without him.

And of course, a massive thank you to my parents, friends, and partner who support me in everything that I do. Thanks for checking in on me and reminding me to take breaks. A special thank you to my partner, Lucas, who had been my number one fan and cheerleader throughout the ups and downs of graduate school. Off to Portland we go!

This work was supported in part by the donors of the American Chemical Society

Petroleum Research Fund under award 57452-DNI9, Further acknowledgement of support is made to the Boston University Nanotechnology Innovation Center and the Boston University Photonics Center.

FROM INTERPARTICLE INTERACTIONS TO

EMERGENT BEHAVIOR OF SMART FLUIDS

ABIGAIL RENDOS

Boston University College of Engineering, 2022

Major Professor: Keith Brown, Ph.D., Assistant Professor of Mechanical Engineering, Assistant Professor of Materials Science and Engineering, Assistant Professor of Physics

ABSTRACT

Functional nano or microparticles in solution can form stimuli-responsive smart fluids that exhibit drastic property changes in the presence of magnetic or electric fields that originate from the interparticle interactions. For example, the most commonly utilized type of particle-based smart fluid are magnetorheological fluids (MRF) that contain ferromagnetic microparticles that allow them to reversibly solidify when they experience a magnetic field. The tunable nature of these materials not only make them useful in a variety of industries, but also make them a versatile system in which to study the influence of interparticle interactions on emergent behaviors. In this dissertation, we explore methods for tuning interparticle interactions with applied fields, additives, and functionalized particles and develop, through both experimentation and modeling, design rules for realizing new classes of smart fluids.

First, we address a common limitation on the performance of MRF, namely slip failure, through the use of a shear-thickening additive to reinforce MRF particle chains as slip begins. Through flow- and oscillation-mode rheology, we find that a shear-thickening MRF has 60% higher yield stress than a conventional shear-thinning MRF. The shear-

thickening additive allows us to affect the microstructure of the fluid in order to increase bulk performance by changing its failure mode.

Next, we explore the hypothesis that highly anisotropic 2D sheets can reinforce conventional MRF as an additive by supporting the particle chains. Interestingly, the 2D sheets affect the performance of the fluid minimally in a boundary-driven flow because of the alignment of the sheets in the fluid velocity profile. However, we find that the 2D sheets increase MRF performance in pressure-driven flows by up to 45%. We determine through modeling that this performance improvement stems from the anisotropic sheets physically reinforcing the particle chains. This work has consequences for the design of MRF for applications using pressure-driven flows, such as soft robotics.

In addition to studying the additives as a path to strengthening MRF, we investigate whether the magnetic particles themselves can be modified to chemically adhere to one another, thus providing additional attractive forces to supplement the magnetic force between particles. Using flow- and oscillation-mode rheology, we quantify the performance using both the yield stress and chain stiffness as performance metrics. By developing two different adhesive MRF, we find that linked chains exhibit a 40% increase in yield stress and a 100% increase in stiffness. Using thymine-functionalized particles, we present a dynamic method for linking particles in an MRF for increased performance.

Finally, a system of polarizable nanoparticles is investigated after it is observed to exhibit a macroscopic cellular phase with particle-poor voids and particle-rich walls in a fluid cell when applying an AC and DC field. By tuning the applied AC and DC fields, we identify the conditions necessary for the phase transition using fluorescence microscopy.

We also find through Cahn-Hilliard analysis and additional experiments that the cellular phase is the result of various types of electrically-induced interactions. Specifically, electrophoresis causes the particles to accumulate on one electrode, then electroosmotic and electrohydrodynamic flows occur and exert attractive and repulsive forces on the particles. When the electrohydrodynamic flow dominates, voids nucleate at high field regions at which point spinodal decomposition into the cellular phase occurs. This understanding allows us to explore ways to tune this behavior such as using photolithography to control the location of the voids, and thus the structure of the material.

TABLE OF CONTENTS

LIST OF TABLES

LIST OF FIGURES

LIST OF ABBREVIATIONS

2DMRF	Magnetorheological fluid with 2D sheets
AC	Alternating current
APTES	(3-Aminopropyl)triethoxysilane
cMRF	Conventional magnetorheological fluid
DC	Direct current
DNA	Deoxyribonucleic acid
EF	Electrically responsive fluid
EMRF	Electromagneto-rheological fluids
ERF	Electrorheological fluids
FEA	Finite element analysis
GERF	Giant electrorheological fluids
MRF	Magnetorheological fluids
α-$Ni(OH)_2$	Alpha phase Nickel Hydroxide
pMRF	Phosphonate group functionalized magnetorheological fluid
QDs	Quantum dots
SLA	Stereolithography
stMRF	Shear-thickening magnetorheological fluids
tMRF	Thymine group functionalized magnetorheological fluid
tMRF + mel	Thymine group functionalized magnetorheological fluid and linked with melamine

CHAPTER 1: INTRODUCTION

1.1 Materials by design approach

Modern materials engineering is often inspired by the materials-by-design approach which draws from structure-property relationships to rapidly realize new, high performing materials. This approach, first poised by Eberhardt *et al*. in 1985(Eberhardt, Hay et al. 1985) and further developed by Olson,(Olson 2000), takes advantage of the four interconnected elements of materials science: processing, structure, properties, and performance, and flexible, fundamental building blocks with which to build new materials. Specifically, the way these building blocks are combined can lead to entirely new families of materials, and by understanding and then prioritizing their structure-property relationships, scientists can design materials to exhibit desirable behaviors or performance.(Eberhardt, Hay et al. 1985, Olson 2000, Ahmad 2004, Sumpter, Vasudevan et al. 2015) For example, atoms are often considered the fundamental building blocks of materials and by selecting a class of elements, such as metals, arranging them in a crystal lattice, and adding defects, materials scientists can realize metals that are strong, brittle, pliable, or corrosion-resistant.(Krauss 2015) However, not all of these properties are needed at once and so it is important to design with function in mind. This example highlights the importance of having a versatile set of building blocks with flexible design rules to realize materials by design.

When this approach was first introduced, tuning a material's structure was often referencing its atomic structure and the ability of defects to elicit different properties. Examples of leveraging defects include doping semiconductors to tailor their electronic

properties or quickly quenching steel to ensure a strong martensite structure supersaturated with carbon.(Newman 1982, Eberhardt, Hay et al. 1985, Olson 2000) However, changing a material's structure now has a much broader meaning in that various hierarchies of structure are deliberately architected, from the atomic scale to the mesoscale and ultimately the macroscale.(Gerberich, Jungk et al. 2003, Montemayor, Chernow et al. 2015) The ability to alter structure at all levels of a material can lead to the development new, potentially transformative, classes of materials making materials by design a fascinating and useful lens through which to view materials science.

1.2 Colloids as a subset of designer materials

A materials space in which the materials-by-design approach is particularly powerful is colloidal systems due to the versatility of colloidal particles as building blocks of new materials. Colloids are broadly defined as particle suspensions where the particles range from 10 nm to 100 μm and are utilized in a vast range of industries including food science, cosmetics, and pharmaceuticals.(Aranson 2013, Dickinson 2015) Recently, robust methods have been developed to synthesize colloidal particles that vary in size, shape, and composition thus comprising an extensive materials design space.(Glotzer, Solomon et al. 2004, Lu and Yin 2012, Li, Yang et al. 2019) Further adding to the versatility of these systems, nanoparticles often have unique electric, magnetic, or optical properties not exhibited on larger scales that can be leveraged when developing new materials.(Landman, Barnett et al. 1992, Hodes 2007) For example, ferrite, a polymorph of iron oxide, is a ferromagnetic material, but iron oxide nanoparticles exhibit superparamagnetic behavior by which the magnetization can randomly reverse due the thermal energy being on the

order of the energy required for the magnetization direction to change.(Hodes 2007) As a result of these vast and interconnected avenues of tunability, colloids are a promising medium with which to explore materials design.

In addition to designing the particles themselves, colloidal particles are often functionalized to promote assembly, alter interparticle interactions, or even impart entirely new functionality such as stimuli-responsive behavior. For example, coating colloidal particles with a charged moieties causes the particles to repel one another at short distances and is commonly used to reduce particle aggregation.(Nelson and Braun 2007) Additionally, surface functionalization can make an already stimuli-responsive colloid, such as a magnetic particle suspension, even more versatile. An exciting exploration of this idea was realized using DNA-functionalized magnetic particles to make artificial micro-swimmers by linking the magnetic particles into filaments whose movement was controlled with a time-varying magnetic field.(Dreyfus, Baudry et al. 2005) Furthermore, the interactions of functionalized colloidal particles can be tailored by their environment, for example through changes in surfactants, solvents, and temperature, making the design space even more flexible and exciting.(Lu and Yin 2012, Sacanna, Pine et al. 2013) These methodologies have been used to assemble ordered structures from colloidal particles(Glotzer, Solomon et al. 2004, Lee, Chan et al. 2004, Li and Fu 2006) much like atoms in a lattice, which has led to colloidal particles being considered “artificial atoms” in the materials design space.(Hong, Cacciuto et al. 2006, Buck, Bondi et al. 2011, Lu and Yin 2012)

1.3 Reductionism versus emergence in colloidal materials

1.3.1 Success of reductionism for determining material properties

An important aspect of designing materials is either determining or predicting structure-property relationships so that the designer can produce a material with specific functionalities or emergent behaviors. Traditionally, a reductionist approach quantifies material properties by considering the material to be a sum of its elementary building blocks. Reductionism is frequently used in determining and predicting material properties because, in many cases, it can do so successfully. (Anderson 1972, Gallagher, Appenzeller et al. 1999, Pietronero 2008) A simple example of a material property that is additive is density because it can be determined by summing the weighted densities of each atom present. Within magnetic colloidal systems specifically, an additive material property is the magnetic saturation of the suspension M_s which scales with the volume fraction φ of magnetic particles and follows the relationship,(Ginder and Davis 1994)

$$M_s = \varphi \mu_0 M \tag{1.1}$$

where $\mu_0 = 4\pi * 10^{-7}$ H/m is the vacuum permeability and M is the magnetic saturation of the magnetic particles, typically expressed in A/m. Essentially, this equation is a form of the rule of mixtures, which can generally be applied to suspensions and composite materials when properties scale with the volume fraction of a particular constituent of the material.

1.3.2 Emergent properties resulting from interparticle interactions

While reductionism is successful in predicting some material properties, not all ensembles act as a sum of their basic elements and follow the rule of mixtures, but instead

exhibit emergent behaviors. This idea of emergence or "more is different" was first conceptualized by P. W. Anderson in the 1970s as a potential consequence of the interactions between the fundamental elements of a material, (Anderson 1972) whether that be atoms, molecules, or colloidal particles. This is a particularly important concept when considering colloids because their collective behavior can be difficult to understand with a reductionist mindset. For example, while Einstein's equation for viscosity,(Mardles 1940)

$$\eta = \eta_0(1 + 2.5\varphi) \tag{1.2}$$

predicts the viscosity η of a colloid accurately based on the viscosity of the medium η_0 in dilute suspensions, it does not hold at high φ. Instead, jamming occurs where particles are in such close contact, they cannot move around each other. This causes a discontinuity in η so that the suspension becomes much more viscous, often exhibiting a yield stress ($\eta \rightarrow \infty$) due to the interacting particles. (Trappe, Prasad et al. 2001, Nelson and Ewoldt 2017) Thus, the suspension acts like a solid instead of a liquid, a phase change that cannot be captured by Eq. 1.2, or smooth corrections to this equation, and is important when designing yield stress fluids for applications in cosmetics, food science, and many other industries. (Coussot 2005) This example of a colloidal phase transition highlights the relevance of interparticle interactions in driving emergent behavior.

1.3.3 Designing emergent behavior in smart fluids

Here, we explore a stimuli-responsive subset of colloids described as smart fluids that respond to electric or magnetic fields due to the suspended functional particles. The application of a magnetic or electric field tunes the interparticle interactions and affects their collective behavior, making smart fluids an excellent model system in which to study

the influence of various interactions on emergent properties. Using the materials-by-design approach, we design smart fluids with colloidal particles as the building blocks, as shown in Fig. 1.1 (a) and take advantage of their flexibility and the strong connection between interparticle interactions on the nanoscale and performance on the macroscale, which is depicted in Fig. 1.1 (b).

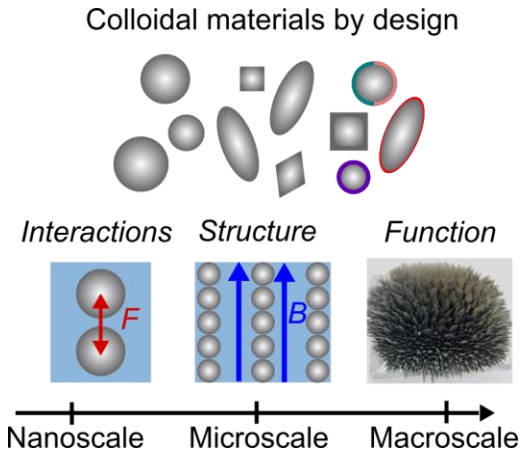

Figure 1.1 Overview of materials-by-design approach applied to development of novel smart fluids. (a) Colloidal particles serve as the building blocks when designing smart fluids. They can be tuned through changes in size, shape, or surface functionalization. (b) The interparticle interactions or force *F* between particles determine their assembly into a structure on the microscale. This structure, which is predominately dictated by magnetic field *B* in the case of magnetorheological fluids, governs the function or performance of the material on the macroscale. We can develop new classes of materials and better performing materials by utilizing the flexible design rules within colloidal systems.

In this work, we focus on two types of smart fluids: MRF, or those that solidify in the presence of a magnetic field, and an electrically responsive fluid (EF) that exhibits spinodal decomposition upon the application of an electric field. MRF are composed of functional microparticles where dipole-dipole interactions tend to dominate whereas the EF we study is comprised of a suspension of nanoparticles, allowing thermal energy and

other interactions to play a larger role. We first explore ways to improve the performance of MRF by tuning interparticle interactions with additives in Chapters 4 and 5 followed by functionalizing the particles to enable chemical linking in Chapter 6. Then, we explore emergent phase behavior in EF by applying both an AC and DC field and using each as an experimental knob to tune interparticle interactions in Chapter 7.

1.4 Overview of chapters

In Chapter 2, we delve into the theory used to describe interparticle interactions and consider various forces that influence these interactions. First, field induced interactions are discussed in terms of defining the force between two particles in the presence of either a magnetic field or an electric field. Then, we consider the influence of thermal energy and why it must be considered as an important energetic contributor in nanoparticle suspensions. Additionally, the influence of hydrodynamic and electrohydrodynamic forces are considered. Given the relative strength of each of field induced interactions to the other forces discussed, phase transformations can occur in both magnetically and electrically responsive systems which is considered in section 2.2.1. Lastly, the continuum properties of MRF are outlined in order to highlight the relevant constitutive models used to parameterize their bulk behavior.

The methodologies utilized throughout Chapters 4-7 are outlined in detail in Chapter 3. First, the formulations for each smart fluid are described along with a discussion detailing how they were prepared. The smart fluids are: the conventional MRF, shear-thickening MRF, MRF with 2D plates, chemically-linked MRF, and finally the quantum dot suspension. Next, the methodologies for both flow-mode and oscillation-mode

rheology are outlined along with a discussion of important considerations for the rheology of MRF in Section 3.2.3. While rheology is a boundary-driven flow, we also characterized MRF in a pressure-driven flow in Chapter 5. Thus, we include Section 3.3 to discuss the characterization of MRF in pressure-driven flow using a custom apparatus that features a syringe pump, movable magnets, and pressure sensors.

The influence of shear thickening on MRF behavior and performance is discussed in Chapter 4 to determine whether slip failure could be prevented through the use of shear-thickening additives. First, the importance of additives in determining MRF behavior is discussed along with the few examples of prior work on shear-thickening MRF. To determine the role of shear thickening, the rheological properties of a typical, shear-thinning MRF were compared to a shear-thickening MRF. Their formulations and basic rheological properties are outlined first, followed by their performance in terms of both yield stress and crossover stress which revealed that the shear-thickening MRF exhibited a 60% improvement in performance, as defined by the maximum shear stress. It was hypothesized that this performance improvement may be due to the prevention of slip by the shear-thickening additive, thus altering the failure mode of the MRF. To explore this hypothesis, we formulated a dipole-dipole model of MRF and use this model to interpret the rheology results. This analysis confirmed the ability of a shear-thickening additive to prevent slip, and the presence of slip in the conventional MRF that was found by repeating measurements at various gap heights of the rheometer. Through this analysis and the results from oscillation-mode rheology, we showed that the conventional MRF undergoes both

slip and affine failure whereas the shear-thickening MRF fails only once, at the strain predicted by the dipole-dipole model for affine failure.

Chapter 5 explores the hypothesis that anisotropic additives will reinforce particle chains by determining the performance of MRF with highly anisotropic 2D sheet additives This chapter begins with an overview of the current understanding of the influence of anisotropic additives on the performance of MRF which is muddled by observations of these additives both improving and hindering performance and a lack of prior modeling to explain the observed results. In order to address this knowledge gap and test the influence of the highly anisotropic 2D sheets, flow mode rheology was conducted and the results are outlined in Section 5.2. Next, the performance was also tested in a pressure-driven flow due to this flow type being relevant in many MRF applications. These experiments showed a flow-rate dependent enhancement in performance due to the 2D sheets, which at best provided 45% improvement in saturation pressure, and was further investigated through modeling based on the Buckingham-Reiner equation in Section 5.4. This modeling revealed the importance of the additive length scale on the ability of the 2D sheets to improve the performance in a boundary-driven flow.

In Chapter 6, guided by the performance improvements seen in Chapters 4 and 5 when chains are supported or reinforced, we hypothesized that adhesive magnetic particles would increase both the yield stress and stiffness of the MRF. While there is limited prior work on chemically-adhesive MRF, the few examples are discussed which include one that utilized hydrogen bonding and two that included covalent bonding between particles. Then, we explored the potential of chemical bonds to influence and strengthen interparticle

interactions, thus potentially improving the bulk performance of the MRF. To test the influence of chemically-linked MRF, rheology was conducted on an MRF with particles functionalized using etidronic acid which are expected to interact through hydrogen bonding in Section 6.3. The performance improvement was quantified for both flow- and oscillation-mode rheology, which showed 100% increase in MRF stiffness due to the chemical bonds between particles. By leveraging chemistry, another system of adhesive particles was studied in which a small molecule could be dynamically added to functionalized particles when linking is desired. The performance of the dynamically linked MRF was compared to an MRF without the linking molecule and we found a similar increase in both yield stress and stiffness. This suggested that both systems have particles with similar adhesive strength and showed the potential of linked particles to realize smart fluids with tailored performance.

In Chapter 7, typical electric field-induced particle assembly parallel to the field is discussed first followed by examples of prior work where a unique macroscopic cellular phase was observed due to particle assembly normal to the field with particle-poor voids are surrounded by particle-rich walls. The assembly of the cellular phase in our quantum dot suspension observed using the fluid cell outlined in Chapter 3 was explored in detail in Section 7.3. This phase required application of both a DC and AC field and varied with particle volume fraction. The results of these experiments are shown and then the mechanism of formation is discussed. In order to understand the formation of this phase, a Cahn-Hilliard analysis was conducted which helped identify the role of electrophoresis, electroosmotic flow, and electrohydrodynamic flow in determining the phase behavior of

this system. Finally, these results helped determine commonalities between our system and the prior work which led to the formation of the cellular phase.

In Chapter 8, the major results from this body of work on the influence of interparticle interactions on the emergent behavior of smart fluids is summarized. Then, a discussion on the implications of this work for designing smart materials is included with emphasis on the importance of understanding and modeling interparticle interactions. An application of this work in designing new materials is also described in which we used the knowledge gained from our studies of MRF performance to develop a smart fluid formulation used to actuate soft robots which highlights the advantages of using colloidal particles as building blocks in materials by design. This work ends with considerations for potential future work based on the discoveries and understanding gained in Chapters 4-7. Examples of potential directions include leveraging particle functionalization to synthesize MRF that are multifunctional, introducing a photo-crosslinking polymer to create permanent cellular structures and enable further study of their structure, and developing magnetically responsive formulations with rheological properties appropriate for SLA 3D printing to enable printing of magnetorheological elastomers. These directions will apply the fundamental understanding gained through this work to both studying and designing next-generation smart materials.

CHAPTER 2: THEORY

2.1 Interparticle interactions

2.1.1 Field induced interactions

Due to the importance of interparticle interactions in determining the behavior and performance of smart fluids, we define a system of two particles in Fig 2.1 (a) with radius *R* separated by a distance *r* in the *x*-*y* plane in order to discuss the influence of different interactions where the interparticle interaction force is along $\hat{r}$. For smart fluids, the interactions caused by a magnetic or electric field are an important, and often dominant, force affecting particle assembly and so we start our discussion with field induced particle interactions.

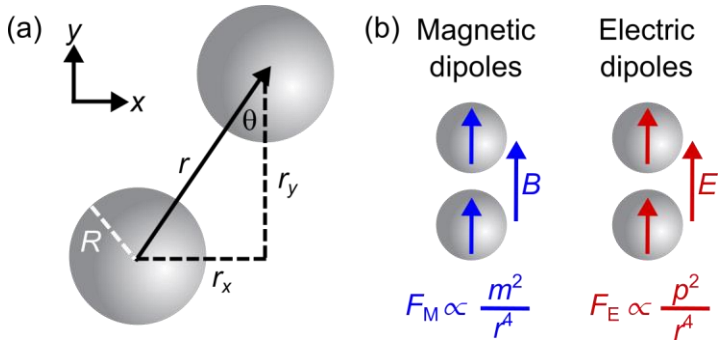

Figure 2.1. (a) Coordinate system for two particles of radius *R* separated by distance *r* with one particle offset at an angle θ. *r* can be decomposed into its *x* and *y* components r_x and r_y. (b) When $\theta = 0$ as is the case when MRF and ERF form particle chains in the presence of magnetic field *B* and electric field *E*, respectively, the dipoles are aligned with the field and experience an attractive force. For both sets of dipoles, the attractive force is proportional to r^{-4}.

For MRF, interparticle interactions are dominated by the magnetic dipole-dipole force F_m induced by magnetic field *B* between neighboring magnetic dipoles $\boldsymbol{m}_1$ and $\boldsymbol{m}_2$ described by(Ferraro 1962, Han, Feng et al. 2010)

$$\boldsymbol{F_M} = \frac{3\mu_0}{4\pi r^5}\left[(\boldsymbol{m}_1 \cdot \boldsymbol{r})\boldsymbol{m}_2 + (\boldsymbol{m}_2 \cdot \boldsymbol{r})\boldsymbol{m}_1 + (\boldsymbol{m}_1 \cdot \boldsymbol{m}_2)\boldsymbol{r} - \frac{5(\boldsymbol{m}_1 \cdot \boldsymbol{r})(\boldsymbol{m}_2 \cdot \boldsymbol{r})}{r^2}\boldsymbol{r}\right], \quad (2.1)$$

where bold variables are vectors, μ_0 is magnetic permeability of free space, and *m* is the strength of the magnetic moment. In the case of a typical MRF, $\boldsymbol{m}_1$ and $\boldsymbol{m}_2$ are equal in magnitude and aligned in the *y*-direction, parallel to the applied field and the attractive F_M can be simplified to,(Han, Feng et al. 2010)

$$F_{M,r} = \frac{3\mu_0 m^2}{4\pi r^4}(3\cos^2\theta - 1) \quad (2.2)$$

which is the force between magnetic dipoles along $\hat{r}$. In the case of MRF, it is desirable to calculate the dipole-dipole force in the direction of an applied shearing motion (*x*-direction) $F_{M,x}$,

$$F_{M,x} = \frac{3\mu_0 m^2}{2\pi r^4} \cdot \sin(\theta)(3\cos^2\theta - 1), \quad (2.3)$$

because this force is directly related to the yield stress τ_0 of the MRF. $F_{M,x}$ provides a resistance against shear deformation of the particle chains, thus dictating the bulk performance of the smart fluid. Similar analytical dipole-dipole models have been presented in the MRF literature due to their success in predicting τ_0.(Ginder and Davis 1994, Ginder, Davis et al. 1996, Jolly, Carlson et al. 1996, Bossis, Lemaire et al. 1997) To estimate τ_0, we simply divide $F_{M,x}$ by the relevant area $A = \frac{(2R)^2\pi}{6\varphi}$ that depends on the volume fraction φ which describes a theoretical maximum yield stress for the MRF with respect to θ and set $r = 2R$ to simplify

$$\tau_0 = \max\left(\frac{9\mu_0 m^2 \varphi}{64\pi^2 R^6} sin(\theta)\,(3\cos^2\theta - 1), \theta\right). \quad (2.4)$$

Equation (2.4) is an example of applying our understanding of interparticle interactions to

predict performance which is a powerful tool when designing materials.

In systems of polarizable particles, the presence of electric field *E* will cause particles to behave as electrical dipoles in analogy with how *B* induces dipoles in magnetically responsive particles. In this case, the force between two particles with parallel dipole moments *p* aligned along the *y*-direction as seen in Fig. 2.1 (b) in a medium with permittivity $\varepsilon_m$is defined as,(Davis 1992)

$$F_{E,r} = \frac{3p^2}{2\pi\varepsilon_0\varepsilon_m r^4}(3\cos^2\theta - 1), \tag{2.5}$$

where ε_0 is the permittivity of free space and *p* is defined as,(Davis 1992)

$$p = 4\pi\varepsilon_0\varepsilon_m R^3 E\frac{(\varepsilon_p - \varepsilon_m)}{\varepsilon_p + 2\varepsilon_m}, \tag{2.6}$$

where ε_p is the permittivity of the particles. We see from Eqns. 2.2 and 2.5 that both F_{M} and F_{E} decay as r^{-4} and depend on the properties of the particle, either *m* for magnetic dipoles or *p* for electric dipoles. Both systems are depicted in Fig. 2.1 (b) with magnetic dipoles in blue and electric dipoles in red.

2.1.2 Influence of thermal energy

Thermal energy is the internal energy matter contains due to its temperature *T* and the cause of Brownian motion of particles in solution. Interestingly, thermal energy can hinder the assembly of particles into ordered structures when it is on the order of other interparticle interaction energies and is defined as,

$$U_T \lesssim k_b T. \tag{2.7}$$

where k_b is Boltzmann's constant. For example, for nanoscale particles, thermal energy often dominates the dipolar interactions discussed in the previous section. In order to

understand this, we examine the non-dimensional ratios of the dipole interaction energy to thermal energy for systems with either *B* or *E*. For magnetic particles with magnetic saturation *M*, this ratio is,(Rosensweig 1985)

$$\Lambda_{\mathrm{M}} = \frac{\mu_0 M^2 \pi R^3}{9 k_B T}. \tag{2.8}$$

For the MRF studied here, the 4 μm carbonyl iron particles have $M = 1.7{*}10^6$ A/m(Yang, Yu et al. 2017) resulting in $\Lambda_{\mathrm{M}} \sim 1 * 10^9$ which is much larger than one indicating that dipolar interactions will dominate. However, if the particles were instead iron oxide ($M \sim 4.0{*}10^5$ A/m) and reduced in size three orders of magnitude to 4 nm (Guardia, Labarta et al. 2011) , then $\Lambda_{\mathrm{M}} \sim 0.1$ so thermal energy is higher than the magnetic interaction energy which allows Brownian motion of the particles to prevent significant aggregation. This is the case for ferrofluids that do not experience solidification in the presence of an applied magnetic field.

For systems where *E* is applied, the non-dimensional ratio is,

$$\Lambda_{\mathrm{E}} = \frac{\alpha E^2}{8 k_B T}, \tag{2.9}$$

where α is the particle polarizability. For the suspension under study in Chapter 7, we estimate $\Lambda_{\mathrm{E}} \sim 0.008$, indicating that induced dipole mediated assembly should not occur and that other interactions must have driven the observed particle assembly. Thus, it is important to consider thermal energy when studying interparticle interactions because it determines when a given interaction will have a significant influence on the behavior of the colloidal particles.

2.1.3 Influence of hydrodynamic and electrohydrodynamic forces

In addition to interactions between the particles themselves, the interactions between the particles and their fluidic medium can also influence assembly. Hydrodynamic forces are the forces exerted on particles by the fluid and are related to the fluid's viscosity η and local velocity v. The hydrodynamic force F_{H} in smart fluids is often approximated using Stokes' drag equation due to typical flows being at low Reynold's number,(Han, Feng et al. 2010, de Vicente, Klingenberg et al. 2011)

$$F_H = 6\pi R\eta v. \tag{2.10}$$

By increasing or decreasing η with additives, the magnitude of this force can be modulated to influence particle movement. Additionally, as is seen in Chapter 5, movement of anisotropic particles is influenced by the non-uniform velocity profiles in the system due to presence of a boundary- or pressure-driven flow which is another way hydrodynamic forces can play a role in colloidal systems.

In the case of charged particles in an electric field, the free charges in the screening layer around the particle move in the direction of the electric field, thus causing the particle to move in the opposite direction. This force is called electrophoresis and the velocity of particles due to electrophoresis v_p can be expressed in terms of E and the electrophoretic mobility μ_p,(Dickerson and Boccaccini 2012)

$$v_p = \mu_p E. \tag{2.11}$$

Importantly, μ_p is defined using the Helmholtz-Smoluchowski equation,(Dickerson and Boccaccini 2012)

$$\mu_p = \frac{\varepsilon_m \zeta}{\eta} \text{ for } \kappa R \gg 1 \tag{2.12}$$

with ζ being the zeta potential of the particle and κ being the Debye length of the particle. Combining Eqns. 2.11 and 2.12, we find

$$v_p = \frac{\varepsilon_m \zeta}{\eta} E \text{ for } \kappa R \gg 1, \tag{2.13}$$

for a particle undergoing electrophoresis. Thus, we can use Eq. 2.13 to estimate the v_p of the quantum dot (QD) particles used in Chapter 7 that experience electrophoresis with the application of a DC field. The QDs are suspended in 3.125 mM borate buffer, κ = 0.18 nm^{-1} and R = 8.5 nm, so $\kappa R > 1$. Therefore, based on Eq. 2.13, these particles with $\zeta_p \cong$ -30 mV (Mahendra, Zhu et al. 2008) at room temperature in water will move ~0.2 mm/s when 2 V is applied across 200 µm. Thus, the application of 2 V can assemble the QDs onto the positive electrode as shown in Fig. 2.2 (a) within ~1 s due to the electrophoretic force on the particles.

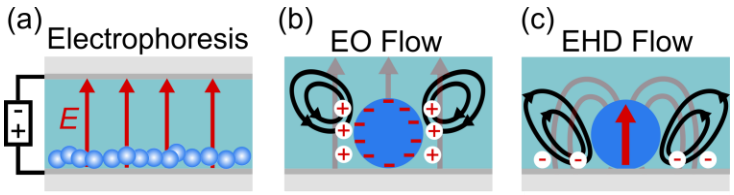

Figure 2.2 (a) Electrophoresis of the negatively charged particles onto the positive electrode with electric field *E* oriented normal to the electrodes. (b) Electroosmotic (EO) flow due to the ions in the Debye layer of the positively charged particle which is purely attractive. (c) Electrohydrodynamic (EHD) flow due to the interaction of the induced dipole with the ions accumulated on the electrode which is short-range attractive, long-range repulsive. *E* is directed vertically for (a) – (c).

Beyond the basic hydrodynamic forces between particles and their host fluid, electrically-induced flows from electrohydrodynamic forces can play an important role in electrically mediated particle assembly. The presence of electrohydrodynamic forces is related to the ions in the medium that move and accumulate around charged particles in the

Debye layer and on the electrode surface in the electric double layer. There are two electrically-induced flows that result, namely electroosmotic (EO) flow and electrohydrodynamic (EHD) flow as shown in Fig. 2.2.(Ristenpart, Aksay et al. 2007) EO flow is purely attractive when particles are assembled on an electrode via electrophoresis as is seen in Fig. 2.2 (b) and will cause particles to aggregate on the surface of the electrode. In Fig. 2.2 (c), assuming positive polarizability of the particle, EHD flow is attractive at short ranges and repulsive at long ranges which can mediate particle assembly into a porous cellular structure due to these unique interparticle interactions which will be discussed in detail in Chapter 7. The presence of electrohydrodynamic forces add to the myriad methods in which particle assembly, and thus smart fluid behavior, can be tuned through interparticle interactions.

2.2 Emergent behavior of fluid-particle systems

2.2.1 Phase transformations in particle suspensions

Smart fluids are known for their phase transformations in the presence of a field, such as the reversible solidification that is typical of an MRF or electrorheological fluids (ERF). As discussed, this is due to the dipole-dipole interactions between the particles. However, particle assembly can result in other, uncommon phase transformations which is the case in Chapter 7 as the nanoparticle suspension undergoes spinodal decomposition upon the application of a DC and AC field. Initially, particles assemble due to electrophoresis as described in Section 2.1.3 and thus the system is restricted to 2D space. This phase separation results in areas with high and low particle concentration with a structure determined by the interparticle interactions.

In general, spinodal decomposition is well modeled by a Cahn-Hilliard analysis and can be used to understand the onset of phase separation in colloids. This analysis begins with the convection-diffusion equation,(Stocker 2011)

$$\frac{\partial n(\boldsymbol{l},t)}{\partial t} + \boldsymbol{\nabla} \cdot [n(\boldsymbol{l},t)\boldsymbol{v}(\boldsymbol{l},t)] = D\nabla^2 n(\boldsymbol{l},t), \tag{2.14}$$

where the first term describes the change in particle areal concentration *n* with time *t* at a location $\boldsymbol{l}$ on a surface as we constrain our analysis to occur in a two-dimensional system after electrophoresis occurs. The second term describes the convection of particles due to *v*, and the final term represents the diffusion of the particles with diffusion coefficient *D*, which is assumed to be constant. The total number of particles in our system does not change and begins at an initial concentration of particles n_0 so no source or sink term is included.

In order to understand the onset of the phase change, a plane wave perturbation n' is applied and the growth or decay of this term will determine the stability of the film. This leads to an expression,

$$n(\boldsymbol{l},t) = n_0 + a(t)\mathrm{e}^{ikx}, \tag{2.15}$$

where *a*(*t*) is the amplitude of the wave perturbation, *k* is the non-dimensional wave vector normalized by *R*, and *x* is a direction along the electrode. We assume that initially the perturbation n' is small compared to n_0. Due to this perturbation, the flow field can be separated into $\boldsymbol{v} = \boldsymbol{v}_0 + \boldsymbol{v}'$ where $\boldsymbol{v}_0$ is due to n_0 and $\boldsymbol{v}'$ is due n'. However, we assume the initially uniform distribution of particles indicates that $\boldsymbol{v}_0 = 0$. Thus, Eq. 2.14 can be linearized to show,

$$\frac{\partial n'}{\partial t} + n_0 \nabla \cdot \boldsymbol{v}' = D\nabla^2 n'. \tag{2.16}$$

By introducing Eq. 2.15 into Eq. 2.16 and simplifying, the expression becomes,

$$e^{ikx} a'(t) + n_0 \nabla \cdot \boldsymbol{v}' = Da(t)\nabla^2 e^{ikx}. \tag{2.17}$$

Drawing from the analysis performed by Hardt *et al*,(Hardt, Hartmann et al. 2020) we define $\boldsymbol{v}'$ generally using the integral,

$$v' = \frac{-\mathrm{a(t)} e^{ikx} i}{4\pi\eta} \int_{-\pi}^{\pi} \int_{0}^{\infty} \sin(kl\cos\theta)\cos(\theta) \cdot v(l)\, dr d\theta, \tag{2.18}$$

where $v(l)$ is the flow velocity as a function of the magnitude of the location *l* in the x-y plane and θ describes the direction of *l*.

When solving, v' should represent the flow in the system under study and can be interchanged to understand the onset of spinodal decomposition for different flows. For the system under study, the two flows that are present were outlined in Section 2.1.3 and are EO and EHD flow. The EHD velocity $v_{EHD}(l)$ and EO velocity $v_{EO}(l)$ can be defined as,

$$v_{EHD}(l) = V^2 \gamma_{EHD} f_{EHD}(l) \tag{2.19}$$

and

$$v_{EO}(l) = V_{DC} \gamma_{EO} f_{EO}(l), \tag{2.20}$$

where the functions $f(l)$ describe the flow at a point *l* away from a single particle based on the flow profiles in Fig. 2.3 (a) which were replotted from theory described by Ristenpart *et al*.(Ristenpart, Aksay et al. 2007) and the constants γ describe the strength of the flow field with subscripts denoting EHD and EO flow. It is known that EHD flow is proportional to the voltage squared, whereas EO flow scales directly with the applied voltage(Ristenpart, Aksay et al. 2007) as described in Eqs. 2.19 and 2.20. For each flow,

the integral in Eq. 2.18 was solved numerically as a function of *k*. Thus, Eq. 2.18 can be expressed as,

$$v'(k) = \frac{-a(t)e^{ikx_i}}{4\pi\eta}(V^2\gamma_{EHD}W_{EHD}(k) + V_{DC}\gamma_{EO}W_{EO}(k)), \tag{2.21}$$

where $W_{EHD}(k)$ and $W_{EO}(k)$ are the result of the double integral described by Eq. 2.18 for f_{EHD} and f_{EO}, respectively. The plot of $W(k)/k$ in Fig. 2.3 (b) for EHD shows that at low k (or high wavelength λ) repulsion between particles is expected.

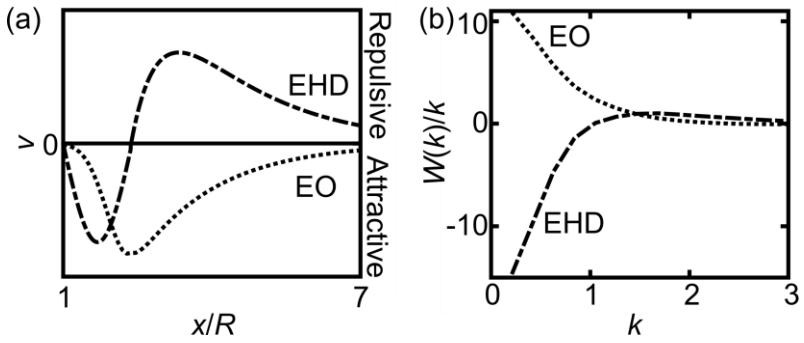

Figure 2.3 (a) Flow velocity *v* versus non-dimensional distance *x*/*R* from the center of a stationary particle, replotted from Ristenpart *et al.*(Ristenpart, Aksay et al. 2007) (b) $W(k)/k$ plotted versus wavenumber *k* for both EHD and EO flows.

To apply this understanding to the particle assembly described in Chapter 7, Eq. 2.21 was introduced into Eq. 2.17 and simplified,

$$a'(t) = a(t)(-Dk^2 + \frac{kn_0}{4\pi\eta}(V^2\gamma_{EHD}W_{EHD}(k) + V_{DC}\gamma_{EO}W_{EO}(k))), \tag{2.22}$$

which describes the evolution of the amplitude over time. When the term multiplied by $a(t)$ is positive, the perturbation grows, leading to spinodal decomposition. Thus, Eq. 2.22, can be used to compute a critical voltage V^* at which an instability will occur which is found to be,

$$V^* = \sqrt{\frac{4\pi\eta Dk}{n_0\gamma_{EHD}W_{EHD}(k)} - \frac{\gamma_{EO}W_{EO}(k)V_{DC}}{\gamma_{EHD}W_{EHD}(k)}}. \tag{2.23}$$

Using the Stokes-Einstein equation for *D*,(Spagnolie 2015)

$$D = \frac{k_B T}{6\pi\eta R}, \tag{2.24}$$

where k_B is Boltzmann's constant and *T* is temperature, Eq. 2.23 can be simplified to,

$$V^* = \sqrt{\frac{2k_B T k}{3Rn_0\gamma_{EHD}W_{EHD}(k)} - \frac{\gamma_{EO}W_{EO}(k)V_{DC}}{\gamma_{EHD}W_{EHD}(k)}}. \tag{2.25}$$

Importantly, Eq. 2.25 shows that V^* is inversely related to n_0, which implies that as the volume fraction increases, the necessary voltage to observe the cellular phase will decrease. Additionally, V^* must be expanded into its AC and DC components,

$$V^* = V_{AC}^* + bV_{DC}, \tag{2.26}$$

where the dimensionless constant *b* allows V_{AC} and V_{DC} to contribute to EHD with intensities reflecting the different complex conductivities at DC and high frequencies.(Ristenpart, Aksay et al. 2007) Additionally, due to electrophoresis assembling the particles onto one electrode, the initial areal concentration n_0 on the positively charged electrode is given by,

$$n_0 = \frac{3\varphi_0 H}{4\pi R^3}, \tag{2.27}$$

where H is the electrode spacing and φ_0 is the initial volume fraction. Incorporating Eq. 2.26 and 2.27 into Eq. 2.25 yields,

$$V_{AC}^* = \sqrt{\frac{8\pi k k_B T R^2}{9H\varphi_0\gamma_{EHD}W_{EHD}(k)} - \frac{\gamma_{EO}W_{EO}(k)V_{DC}}{\gamma_{EHD}W_{EHD}(k)}} - bV_{DC}, \tag{2.28}$$

which was simplified to the functional form used to fit the data in Chapter 7, Fig. 7.3,

$$V_{AC}^* = \sqrt{\frac{1}{\beta_{EHD}\varphi_0} - \frac{\beta_{EO}V_{DC}}{\beta_{EHD}}} - bV_{DC}. \tag{2.29}$$

where b, β_{EHD}, and β_{EO} are fitting parameters. Eq. 2.29 captures the behavior in our experimental determination of V_{AC}^{*} shown in Fig. 7.3 and confirms that as V_{AC}^{*} increases, φ_0 and V_{DC} decrease. This analysis led to our understanding of the interplay of EO and EHD flow in mediating particle assembly of the system and allows us to predict and thus tune the onset of this phase transformation.

2.2.2 Continuum properties of MRF

The phase transformation from liquid-like to solid-like that occurs in MRF has resulted in a common, continuum approach to modeling their behavior which considers the MRF as an effective medium. The vast majority of continuum studies describe MRF using well-established constitutive models such as the Bingham plastic, Casson, and Herschel-Bulkley models to provide empirical fits to experimental data.(Claracq, Sarrazin et al. 2004, Goncalves, Koo et al. 2006, Whiteley, Gordaninejad et al. 2010, de Vicente, Klingenberg et al. 2011, Ashtiani, Hashemabadi et al. 2015) Each model describes the shear stress τ as a function of the shearing strain rate $\dot{\gamma}$ with constitutive parameters such as viscosity η and yield stress τ_0. Of the three models, the Bingham plastic has no curvature and is linear with a non-zero τintercept while the others have curvature that increases as $\dot{\gamma}$ decreases.

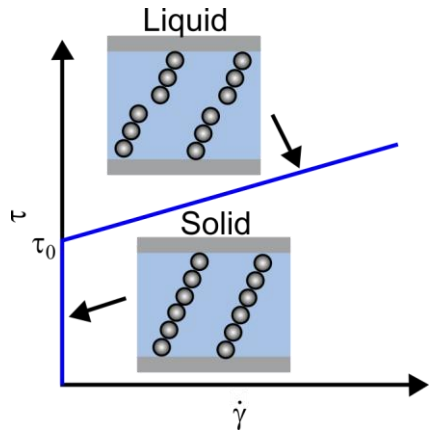

Figure 2.4 Shearing stress τ vs. shearing strain rate $\dot{\gamma}$ for a Bingham plastic. At yield stress τ_0, the solid melts and returns to the liquid state.

The most widely used of the three is the Bingham plastic model,

$$\tau = \eta_B + \dot{\gamma} \cdot \tau_0 \tag{2.30}$$

where η_B is the Bingham viscosity. This model is used most frequently because it fits experimental data very well(Weiss, Duclos et al. 1993, Claracq, Sarrazin et al. 2004, de Vicente, Klingenberg et al. 2011, Ghaffari, Hashemabadi et al. 2014, Ashtiani, Hashemabadi et al. 2015, Wereley, Chaudhuri et al. 2016) and provides a critical experimental metric: τ_0. Though the fluid contains particles and additives in addition to the fluid, its bulk behavior can be thought of as one material that acts as a Bingham plastic with solid-like behavior below τ_0 and liquid-like behavior above τ_0 (Fig. 2.4). A typical range of $\dot{\gamma}$ for which MRF behavior is quantified is 10 – 1000 s^{-1} due to its relevance to rates used in real world applications and restrictions of the testing apparatus itself, which is typically a rheometer with maximum $\dot{\gamma}$ ~ 1000-5000 s^{-1}.(Carlson 2005, Wang and Gordaninejad 2006, Sherman 2016) The Bingham plastic model is most accurate at intermediate $\dot{\gamma}$; however, it tends to miss behavior at low $\dot{\gamma}$ (< 50 s^{-1}) where the Casson and Herschel-Bulkley models may be needed.(Laun, Gabriel et al. 2009, Ghaffari,

Hashemabadi et al. 2014, Ashtiani, Hashemabadi et al. 2015, Sherman 2016, Asiaban, Khajehsaeid et al. 2020) The Herschel-Bulkley model is also able to capture discrepancies at high $\dot{\gamma} > 1000\ s^{-1}$ due to having a third fitting parameter and is used to model MRF that will be operated in that range.(Ghaffari, Hashemabadi et al. 2014) Despite these notable deviations, the Bingham plastic equation successfully describes the vast majority of MRF and is used to quantify τ_0 in Chapters 4, 5, and 6.

CHAPTER 3: METHODS

3.1 Preparation of smart fluids

3.1.1 Conventional MRF

The conventional MRF (cMRF) was prepared using deionized water, carbonyl iron particles (3–5 μm size, Skyspring Nanomaterials, 0990JH), and xanthan gum (Sigma Aldrich, G1253). The same carbonyl iron was used in all MRF formulations including those in Sections 3.1.2 – 3.1.4. Xanthan gum, sodium carboxymethyl cellulose, and oleic acid were considered for the stabilizing additive because they are commonly used as additives in smart fluids.(Weiss, Duclos et al. 1993, Yang, Yu et al. 2017, Morillas and de Vicente 2019) Xanthan gum was chosen because it was not observed to react with the iron particles, unlike oleic acid, and reduced sedimentation more effectively than sodium carboxymethyl cellulose. A shear-thinning stock solution was prepared by mixing 0.25 wt% xanthan gum in DI water and allowing the xanthan gum to dissolve at room temperature. This stock solution was then mixed with 14.2 vol% iron microparticles to form the cMRF and vortexed until homogeneous. The cMRF was used in experiments detailed in Chapters 4 and 5.

3.1.2 Shear-thickening MRF

Shear-thickening MRF (stMRF) samples were prepared using deionized water, carbonyl iron particles, and corn starch (McMaster Carr, 3190K543). Corn starch was selected as a shear-thickening additive because it is widely studied in the context of shear-thickening aqueous solutions.(Kumar, Paul et al. 2019) A shear-thickening stock solution was prepared using 33.3 wt% corn starch and 0.04 wt% xanthan gum in DI water. This

stock solution was vortexed until homogenous and mixed with 14.2 vol% iron microparticles to form the stMRF which was used to compare to the cMRF, which is found to be shear thinning in Chapter 4.

3.1.3 MRF with 2D sheets

The a-$Ni(OH)_2$ 2D sheets were synthesized based on a method developed by D. Jia *et al.*(Jia, Gao et al. 2017) Specifically, 0.35 g (5.83 mM) urea and 0.22 g (0.759 mM) nickel nitrate hexahydrate were dissolved into ethylene glycol/DI water (14 mL/2 mL) solution under vigorous magnetic stirring. Then the mixture was transferred into a 25 mL Teflon-lined autoclave, sealed and heated in an oven at 80 °C for 24 hrs. After cooling down to room temperature, the obtained products were collected by filtration and washed with ethanol three times and subsequently water three times. Finally, the products were dried in a vacuum oven at 60 °C and then dispersed in water for storage.

To prepare the 2D MRF (2DMRF) using the α-$Ni(OH)_2$ sheets, 0.13 wt% xanthan gum and 0.17 wt% α-$Ni(OH)_2$ sheets were dispersed in DI water, then 14.2 vol% iron particles were added and the solution was vortexed until homogenous. The 2DMRF is compared to the cMRF in Chapter 5.

3.1.4 Phosphonate group functionalized MRF

To synthesize an MRF with adhesive particles, a method was adapted from Othmani *et al.*(Othmani, Aissa et al. 2013) to functionalize the carbonyl iron particles with phosphonate groups that can chemically bond when in close contact. Specifically, a 100 µM etidronic acid solution was made by adding 1.72 µL of etidronic acid (Sigma Aldrich, H6773) to 50 mL DI water which was neutralized to pH of seven using sodium hydroxide

(Sigma Aldrich, S8045). Then, 0.5 g of carbonyl iron was added and the vial was rotated on a mechanical spinner for 48 hours. Additional samples were made with 1 mM etidronic acid corresponding to 17.2 µL of acid in 50 mL DI water and again neutralized to pH of seven. After spinning, the particles were washed five times with DI water and then dried overnight. Particles were then added to DI water with 10 mM NaCl to ensure particles do not repel at short distances due to the added charge from the etidronic acid on the surface at volume fractions of 2, 4, 8, or 14.2 vol% to form the phosphonate MRF (pMRF). Samples were sonicated for 2 min prior to testing to break up any particle aggregates that resulted from the drying process. Then, the samples were immediately pipetted onto the rheometer plate where a uniform field was applied to promote linking of particle chains which is further described in 3.2.1.

3.1.5 Dynamically linkable thymine functionalized MRF

To prepare the thymine functionalized particles, we first synthesized a thymine-terminated polystyrene polymer with a phosphonate anchor group according to the procedure reported previously by Santos and Macfarlane.(Santos and Macfarlane 2020) In brief, we first synthesized the thymine-functionalized atom transfer radical polymerization (ATRP) initiator and the propagyl phosphate cyclohexamine salt. The thymine ATRP initiator was then used to synthesize a 10kDa polystyrene polymer via ATRP. Following which, the alkyne functionalized phosphonate was added to the polymer via copper(I) catalyzed azide alkyne cycloaddition to yield the final thymine-functionalized polymer.

To graft the thymine-functionalized polymers onto the carbonyl iron particles, we first activated the surface of the particles by treating them with 0.5 M hydrochloric

acid:(Belyavskii, Mingalyov et al. 2006) 2.0 g of particles were added to 30 mL of 0.5M hydrochloric acid and then mechanically shaken for 40 minutes. The treated particles were washed eight times with DI water and then dried overnight under vacuum. To make each batch of thymine-functionalized particles, 250 mg of activated particles, 39 mg of thymine-functionalized polymer, and 1.5 mL of toluene were added to a 1.5 mL Eppendorf tube. The mixture was sonicated briefly to ensure that the polymers were fully dissolved in toluene before being mechanically shaken at 700 RPM at 70 ˚C for 15 hours. The thymine-functionalized particles were then washed six times with toluene and then dried overnight under high vacuum. Finally, particles were added to anisole to make 2, 4, and 8 vol% samples of tMRF.

In order to link the thymine functionalized particles, melamine was used as a small linking molecule. First, a 99 mM melamine solution was made by mixing 25 mg of melamine (Sigma Aldrich, M2659) with 1mL dimethylsulfoxide (Sigma Aldrich, D8418) and sonicating the solution for 10 min to fully dissolve the melamine. Then 1mL of dimethylformamide (Sigma Aldrich, 72438) was added to the solution and vortexed until mixed. Directly before an experiment, 5μL of the melamine solution was added to 995 μL of anisole (Sigma Aldrich, 123226) to form a 495 μM solution of melamine. Then, particles were added to the 495 μM melamine solution to make 2, 4, and 8 vol% samples and immediately used in the rheometer where the field was applied in order to promote linking between particles in chains through hydrogen bonding, thus making the tMRF+mel.

3.1.6 Quantum dot suspension

Poly(maleic anhydride-alt-1-octadecene) (PMAO)-coated CdSe/CdS quantum dots (QDs) were synthesized using methods described by Chern *et al.* and Nasilowski *et al*. (Nasilowski, Spinicelli et al. 2015, Chern, Nguyen et al. 2017) Typically, the QDs were suspended in a 3.125 mM borate buffer solution (Debye screening length = 5.5 nm)(Cao, Chern et al. 2019) at a volume fraction of 6×10^{-5} which corresponds to a QD concentration of 25 nM. Additional experiments discussed in Chapter 7 were conducted at volume fractions of 1.5×10^{-5}, 3×10^{-5}, and 12×10^{-5}. Quantum dot solutions were refrigerated between experiments.

3.2 Rheology of MRF

3.2.1 Flow-mode rheology

Rheology is conducted in a rheometer with moving top plate and stationary bottom plate where the sample is contained between the two plates separated by gap height h as shown in Fig. 3.1 (a). Flow-mode rheology depicted in Fig 3.1 (b) is used to determine material properties of complex fluids by varying the $\dot{\gamma}$ and measuring the τ required to shear a given sample. Rheological testing in flow mode consisted of pipetting samples onto the rheometer bottom plate after samples were redispersed by vortexing for 30 s. Samples were 163 µL for rheometer gap height h = 500 µm and 85 µL for h = 250 µm. The rheometer (TA Instruments, DHR-1 with TA Instruments Magnetorheology accessory) collected data at $\dot{\gamma}$ = 20–200 1/s with seven points per decade, each averaged over 30 s. This moderate range of $\dot{\gamma}$ was chosen to avoid the low shearing strain rate region where the fluid behavior tends to deviate from the Bingham plastic model which was used to fit the

data as described in Chapter 4.(Weiss, Duclos et al. 1993, Bossis, Lemaire et al. 1997, Zhao, Fu et al. 2019, Asiaban, Khajehsaeid et al. 2020) Flow-mode measurements discussed in Chapters 4 and 5 were conducted with h = 500 µm, while those in Chapter 6 were conducted with h = 250 µm to reduce the volume of fluid required per experiment. Flow-mode measurements were typically completed at logarithmically spaced induced fields B between 0.005 and 1 T. For the chemically-linked MRF described in section 3.1.4, B was applied prior to the experiment for 8 min total (1 min each at linearly spaced B from 0.1 and 0.8 T) to ensure sufficient time for linking between particles to occur.

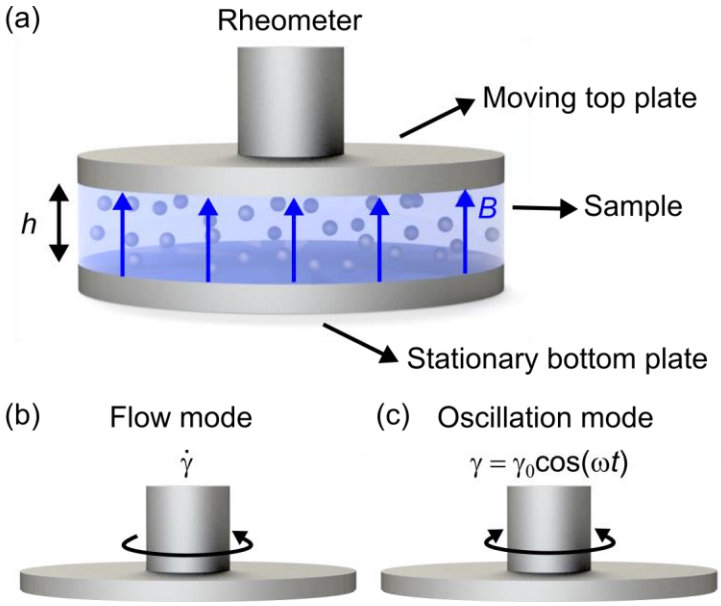

Figure 3.1 (a) Scheme of rheometer with a sample between two plates with the top plate moving either in flow mode (b) or oscillation mode (c). Bottom plate is stationary and the plates are separated by height h with magnetic field B applied vertically between the plates. (b) For flow mode rheology, the top plate is continuously rotating at different shearing strain rates $\dot{\gamma}$. (c) Oscillation mode rheology with top plate oscillating at a time varying strain γ with amplitude γ_0 and angular frequency ω. Figure adapted from Rendos *et al.*(Rendos, Woodman et al. 2020)

3.2.2 Oscillation-mode rheology

Oscillation-mode rheology involves shearing the sample at increasing amplitude or frequency of oscillation in order to determine the material's storage modulus G' and loss modulus G''. For these experiments, the top plate oscillated at a time varying strain γ with amplitude γ_0 and angular frequency ω as shown in Fig 3.1 (c). At low γ_0, the MRF is expected to behave like a solid such that $G' > G''$. However, when the chains begin to fail, G' and G'' will cross and then the material will exhibit liquid-like behavior ($G' < G''$). For the experiments discussed in Chapter 4, oscillation measurements were taken using a constant frequency of 1 rad/s as the torque was increased. Torque ranges were selected to encompass the region where G' and G'' were observed to intersect and varied for each field and fluid tested. Data was collected at 30 points per decade to accurately determine the crossover and were typically completed at logarithmically spaced fields between 0.005 and 1 T. The moduli crossover was analyzed in TA instruments TRIOS software using a linear/cubic interpolation. Oscillation measurements were taken at h = 250, 500, and 1000 μm for the study conducted in Chapter 4. Data points with negative loss modulus were removed as they are not physically meaningful, and only occurred after chains had failed.

3.2.3 Important considerations for rheology of MRF

When conducting rheology of MRF either in flow mode or oscillation mode there are some experimental considerations to ensure successful and repeatable experiments. First, the rheometer user must set-up an experimental procedure on the TA Instruments software TRIOS. Because MRF can exhibit residual magnetization when a magnetic field is turned off or decreased, it is desirable to conduct experiments from low field to high

field. Another way to eliminate the effects of residual magnetization, which is particularly useful when testing from high field to low field is necessary, is to select the demagnetization option on the TRIOS software which quickly alternates the field from positive to negative values at low values of field and can be selected whenever the field changes in the experimental procedure. Another consideration when setting up a rheological experiment is the gap height of the rheometer. Due to MRF being dense iron microparticle suspensions, a gap height that is too small will scratch and damage the plates of the rheometer or lead to unwanted particle aggregates. Typically, it is considered safe to use a gap height at least 10× larger than the diameter of the particles in suspension.(Davies and Stokes 2008, Lin, Cheng et al. 2014) Finally, the TRIOS software displays a minimum sample volume for the selected gap height, however that minimum sample volume is often too low to completely fill the rheometer gap. From experience, you will typically need 5-8 μL of additional fluid to fill the gap and if the gap overfills it is possible to remove the access with a wipe so it is preferable use a slightly larger sample volume than a smaller sample volume. Consideration of each of these guidelines prior to experiments is important to avoid inaccurate data.

3.3 Characterization of MRF in pressure-driven flow

Characterization in pressure-driven flow was performed using a custom flow apparatus (Fig. 3.2) and was used to characterize cMRF and 2DMRF discussed in Chapter 5. The fluid was loaded into a syringe pump (World Precision Instruments, Aladdin Single-Syringe Pump) and pumped through a 2 mm inner diameter tube (McMaster-Carr, 2129T24). Along the flow path, a pressure sensor (Digi-Key Electronics, P7100-103G-

M5) was read using a DAQ (National Instruments, USB-6001) at a sampling rate of 25 Hz and analyzed using MATLAB. Two permanent magnets (CMS Magnetics, NB0205-42NM) were used to apply uniform magnetic field perpendicular to the flow and their distance from the tube was modulated using a micrometer. A gaussmeter (Lake Shore Cryotronics, Model 425) was used to generate a calibration for the field as a function of distance from the permanent magnets which was used to estimate the field present during experiments. The root mean squared of the field was used as the field in calculations. COMSOL simulations of permanent magnets was used to determine the high field length along the tube. An example simulation is shown in Fig. 3.2 (b) and the plot of the field along the tube which is located between the two magnets is plotted in Fig. 3.2 (c). In order to determine the high field length, the full width at half maximum of the curve was calculated from the data in Fig. 3.2 (c).

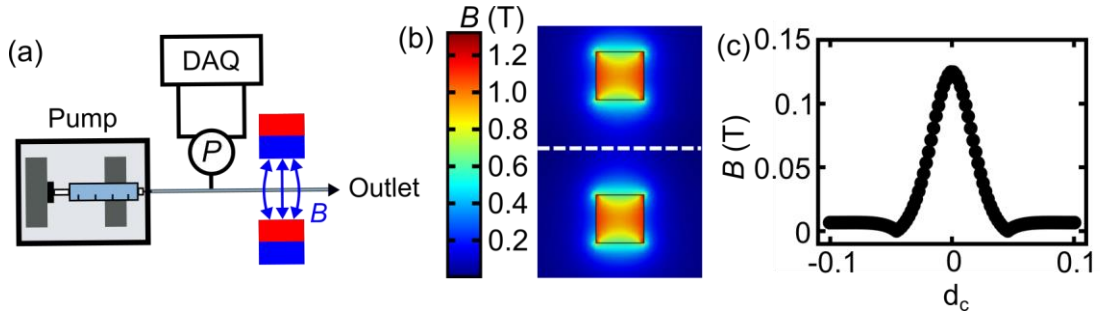

Figure 3.2 (a) Scheme of pressure-driven flow set-up incorporating syringe pump, pressure sensor to measure pressure *P*, magnets with magnetic field *B*, and the tube outlet. The signal from the pressure sensor was read through the DAQ into MATLAB for data processing. Figure reproduced from Rendos *et al.*(Rendos, Li et al. 2020) © WILEY. Reproduced with permission. All rights reserved. (b) Example of COMSOL simulation of *B* between two 1" square magnets positioned 3" apart. (3) Plot of *B* as a function of the central distance d_c along the central line between the magnets indicated in (b) with a white dashed line. $d_c = 0$ is located at the center of that line and is where *B* is at a maximum.

3.4 Fluid cells for observing phase changes

3.4.1 Assembly of fluid cell

In a typical experiment to observe phase changes in the nanoparticle suspension described in section 3.1.5, indium tin oxide (ITO) slides (2277 - University Wafer, 703176 – Sigma Aldrich) were prepared by sonicating them in acetone and subsequently isopropanol for 5 min each before drying them under an N_2 stream. Then, the ITO slides were placed into a 3D printed frame as pictured in Fig. 3.3 (a). A laser-cut polyimide spacer (2271K72 – McMaster) with thickness of 177 ± 1 μm was then placed onto one of the ITO slides. Finally, a 4 µL drop was pipetted onto the middle of the ITO slide with the spacer and then the other slide and top half of the 3D printed frame was seated on top and screwed together, completing the fluid cell in Fig. 3.3 (b).

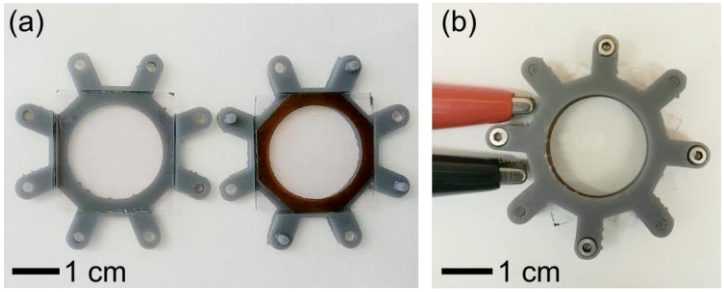

Figure 3.3 (a) Top and bottom of 3D printed fluid cell frame designed to hold one-inch square indium tin oxide (ITO)-coated glass slides. ITO-glass slides are shown with the polyimide spacer on one slide. Arms were used to align the cell and screw cell together. (b) Fully assembled fluid cell with glass slides, droplet, spacer, screws, and leads.

3.4.2 Fluid cell testing and characterization

The complete fluid cell was transferred to an Olympus BX43 microscope with a GS3-U3-120S6M-C Grasshopper camera. A filter cube with an emission wavelength at 642 nm, 75 nm BW (67-036 – Edmund Optics Inc.), a short-pass excitation filter with a

cutoff at 500 nm (84-706 – Edmund Optics Inc.), and a dichroic with cutoff at 550 nm (DMLP550R – ThorLabs Inc.) were used to visualize the photoluminescent QDs. Alligator-clip leads were attached to a corner of each ITO-coated slide as shown in Fig. 3.3 (b) in order to apply an AC voltage with amplitude V_{AC} and frequency f along with a DC offset voltage V_{DC} across the fluid cell using a Keysight 33521B waveform generator. For all experiments, f = 500 kHz while V_{AC} and V_{DC} were varied. Fluorescence micrographs were taken using 5× magnification with a 500 ms exposure time and 14 dB gain to have sufficient contrast.

CHAPTER 4: SHEAR THICKENING PREVENTS SLIP IN MRF

4.1 Importance of additives in determining MRF behavior

Key to our understanding and utilization of MRF is the incorporation of additives in the fluid in addition to the magnetic particles**.** Additives are essential to the fluid stability, but also have the ability to affect smart fluid performance. For example, commercially available MRF typically utilize surfactants and thixotropic agents to prevent sedimentation and irreversible aggregation of magnetic particles.(Ashour, Kinder et al. 1997, Carlson 2016) More recently, the variety of additives tested has expanded to include nanoparticles, nanowires, 2D materials, and non-magnetic microparticles.(Chin, Park et al. 2001, Zhang and Choi 2014, Ashtiani, Hashemabadi et al. 2015) Such additives have been observed to improve the key performance metric inherent to MRF, which is τ_0 when $B > 0$.(Chin, Park et al. 2001, Bell, Karli et al. 2008, Zhang and Choi 2012, Shah and Choi 2014, Wereley, Chaudhuri et al. 2016) Thus, the inclusion of additives in MRF formulations is an important and often successful method to improving MRF properties and performance.

4.2 Overview of prior work and our work on shear-thickening additives

One class of additives that has recently come to the forefront in magnetic complex fluids is shear-thickening agents.(Jolly and Bender 2006, Zhang, Li et al. 2008, Zhang, Li et al. 2010, Peng, Li et al. 2014, Jiang, Hu et al. 2015, Wang, Wang et al. 2016, Tian and Nakano 2017, Lin, Guo et al. 2018) In particular, previous work has focused on the addition of silica nanoparticles into fluids, elastomers, and gels. Despite this attention, it is not clear whether shear-thickening additives improve the performance of MRF or, if they do, the mechanism through which this improvement would arise. Additionally, smart fluids are

typically shear thinning due to the thixotropic agents used to prevent particle sedimentation, but a comparison has never been made between a shear-thinning and shear-thickening smart fluid which might reveal performance differences important to synthesizing new types of smart fluids.

In this chapter, we test the influence of a shear-thickening additive on the performance of an MRF and find that shear thickening improves τ_0 in a manner that we attribute to a change in the mechanism of chain failure. To explore the consequences of shear thickening, we synthesized and compared a shear-thickening MRF (stMRF) and a conventional MRF (cMRF) that was shear thinning. Through testing both fluids using oscillation and flow mode rheology, the stMRF was found to exhibit a 60% higher τ_0 despite having the same volume fraction of magnetic particles. To understand the origin of this increase, we studied the viscoelastic properties of the fluids and found that the cMRF failed at lower strains in a manner that is consistent with chain slip, while the stMRF failed at higher strain with a magnitude that agreed with affine failure of the chains. These results were consistent with a proposed model wherein the shear-thickening additive prevents slip failure of the chains. The performance improvement can be used to synthesize a stMRF that contains less iron but has the same performance as the cMRF, which is highly beneficial to applications in soft robotics and other fields where the weight of the fluid is a drawback. In addition to laying the scientific groundwork for stMRF, the proposed connection between the rheological model and the particle-level model motivates further rheological tuning of MRF to optimize their performance. This work was published in *Smart Materials and Structures*.(Rendos, Woodman et al. 2020)

4.3 Rheological characterization in flow mode rheology

Understanding the influence of a shear-thickening additive required the synthesis of two directly comparable MRF with similar viscosity ranges and the same iron content. Initially, a conventional fluid cF and shear-thickening fluid stF were synthesized and characterized in flow mode rheology where the stF exhibited an increase in effective viscosity η_{eff} at shearing strain rate $\dot{\gamma}$ > 200 1/s as shown in Fig. 4.1 (a). Notably, the typical thixotropic additives used for MRF are shear-thinning and thus the cF included a shear-thinning additive, xanthan gum. Upon the addition of 14.2 vol% iron microparticles to the stF and cF, we realized stMRF and cMRF, respectively. These fluids retained their shear-thickening and shear-thinning character and had similar viscosities as plotted in Fig. 4.1 (b) when measured in flow mode with $B = 0$. More information on the materials and method of formulating stMRF and cMRF were included in Section 3.1.1 and 3.1.2.

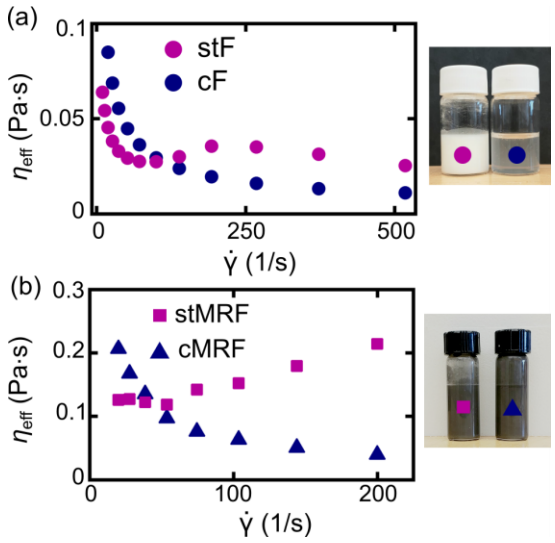

Figure 4.1 (a) Effective viscosity η_{eff} vs. shearing strain rate $\dot{\gamma}$ for a conventional fluid (cF) containing xanthan gum and a shear-thickening fluid (stF) containing both xanthan gum and corn starch. (b) η_{eff} vs. $\dot{\gamma}$ for conventional MR fluid (cMRF) and shear-thickening MR fluid (stMRF). Both have 14.2 vol% carbonyl iron particles.

4.4 Performance of shear-thickening MRF in flow and oscillation mode

In order to determine whether shear thickening improved the performance of MRF, we performed magnetorheology of both MRF. In particular, both were tested in flow mode which is depicted in Fig. 4.2 (a) where the top plate continuously rotated at constant $\dot{\gamma}$ while B was applied along the axes of rotation. The resultant stress τ vs. $\dot{\gamma}$ curves were fit to the Bingham plastic model from Eqn. 2.30. The results of a typical measurement at B = 125 mT shown in Fig. 4.2 (b) revealed that τ_0 is higher for the stMRF than the cMRF. Repeating this process with B varied from 0.005 to 1 T, resulted in τ_0 vs. B for both MRF. In Fig. 4.2 (c), the MR fluids exhibited increasing τ_0 with B and saturation became apparent at large B. Importantly, the stMRF exhibited a marked increased τ_0 at high B, with a 60% increase in τ_0 over the cMRF at B = 1 T.

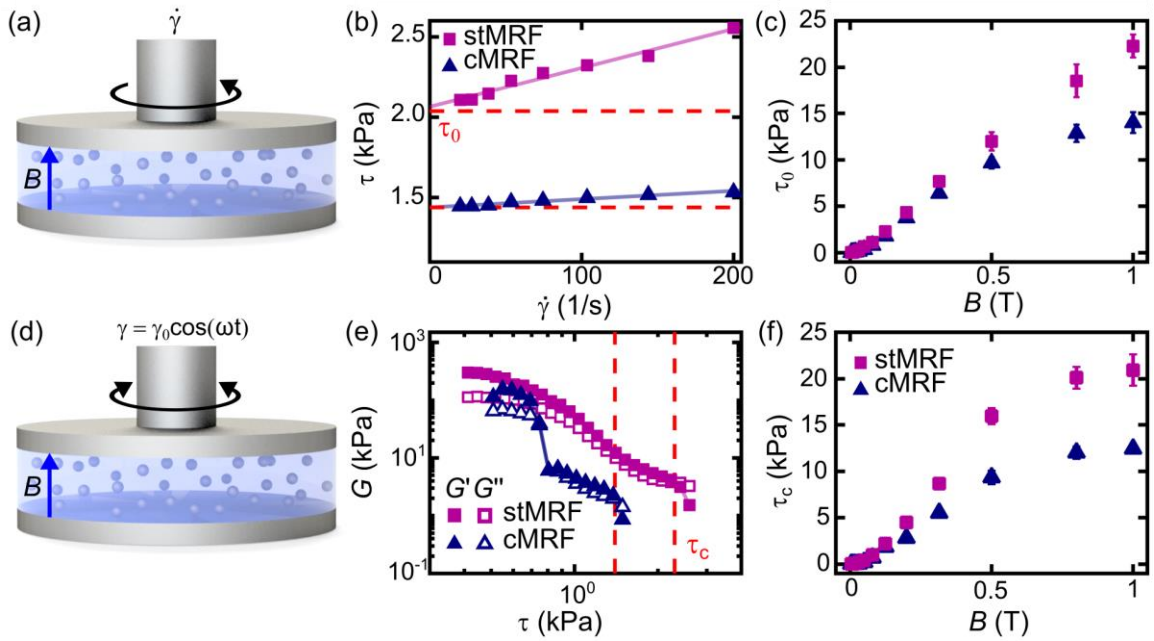

Figure 4.2 (a) Flow mode magnetorheology with constant $\dot{\gamma}$. (b) τ vs. $\dot{\gamma}$ for cMRF and stMRF at 125 mT with linear Bingham plastic fit. τ_0 is indicated as the y-intercept. (c) τ_0 vs. B for cMRF and stMRF. (d) Oscillation-mode magnetorheology with time varying

strain γ varying based upon strain amplitude γ_0 and frequency ω. (e) Storage modulus G' and loss modulus G'' vs. τ for cMRF and stMRF at 125 mT with crossover at stress τ_c indicated. (f) τ_c vs. B for cMRF and stMRF. Error bars on (c) and (f) represent the standard deviation.

While flow mode is conventionally used to characterize MRF, the constant velocity requires that chains are consistently broken and reformed. In contrast, one can explore the response of an MRF in oscillation mode depicted in Fig. 4.2 (d) where the platen rotates in an oscillatory fashion with a constant frequency ω but increasing strain amplitude γ_0. As the amplitude was programmed to begin small and increase, the chains likely remained intact until the amplitude exceeded a critical value. In this mode, the torque needed to maintain a specific γ_0 and the phase lag δ between the motion and the torque were measured and used to report the storage moduli G' and loss moduli G'', where data points with negative G'' were removed as they are not physically meaningful, and only occurred after chains had failed.

In a typical measurement shown in Fig. 4.2 (e), the magnitudes of G' and G'' decreased with increasing stress τ in a manner that illustrates shear melting. At low τ, the material behaved as a solid (i.e. $G' > G''$). In contrast, at high τ, the material behaved as a liquid (i.e. $G'' > G'$). Here, crossover stress τ_c represents the stress at which G'' becomes equal to G' and indicates a change in the microstructure as chains are predominately broken after this point.(Shah and Choi 2014, Vinod, John et al. 2017) The stMRF exhibited larger τ_c than did the cMRF with a 68% improvement seen again at B = 1 T in Fig. 4.2 (f).

The qualitative and quantitative agreement between flow and oscillation-mode testing further confirmed the improvement inherent to stMRF. It is worth emphasizing that both of these fluids had the same iron content, which is a critical feature for comparing

them in a quantitative manner as τ_0 is expected to be proportional to the magnetic particle volume fraction. However, the cause of this improvement was not clear. Interestingly, the difference in moduli curves in Figure 4.2 (e) suggests a change in the failure mode between the two fluids. Specifically, the cMRF shows a rapid decline in both G' and G'' prior to ultimate failure that may be the result of slip, which is known to occur in MRF and has been mitigated in the past using experimental changes such as using roughened or ferromagnetic plates.(Ocalan and McKinley 2012, Jiang, Hu et al. 2015) Strikingly, the stMRF did not exhibit this slip phenomena, which we hypothesized was due to the shear-thickening nature of the fluid.

4.5 Determination of failure mode for shear-thickening and shear-thinning MRF through dipole-dipole model

To investigate this hypothesis, we explored a discrete dipole model describing the magnetic dipole-dipole interactions between ferromagnetic particles in a chain that undergoes shearing to predict τ_0 for comparison with experiment.(Ginder and Davis 1994, Ginder, Davis et al. 1996, Jolly, Carlson et al. 1996, Tang and Conrad 2000, Goncalves, Koo et al. 2006, Si, Peng et al. 2007, Morillas and de Vicente 2019) Shearing the chain increases its overall length, which results in the particles moving apart from their neighbors. However, their dipoles remain pinned in the direction of the applied field. As seen in Fig. 4.3 (a), the shear stress τ initially increases linearly as the chain angle θ increases due to more of the dipole-dipole force being oriented in the shear direction. Further increasing θ results in a peak in τ, which ideally corresponds to the τ_0 of the chain. At a particle concentration of 14.2 vol%, this analysis led to a predicted yield stress τ_0 = 52 kPa at a critical angle $\theta_c = 23^{\circ}$. It is worth emphasizing that the chains will only reach this

point of affine failure if they experience a constant $\dot{\gamma}$ along the vertical distance y between plates as seen in Fig. 4.3 (b). However, the chain may break prematurely causing a lower than predicted τ_0. We hypothesized that this was the case during slip failure shown in Fig. 4.3 (c) where $\dot{\gamma}$ increased dramatically at the location of slip as the chain shears apart. This local increase in $\dot{\gamma}$ provides an explanation for why shear-thickening additives may prevent this mode of failure as shear-thickening fluids experience an increase in η_{eff} when $\dot{\gamma}$ increases, which may arrest slip as it begins to occur.

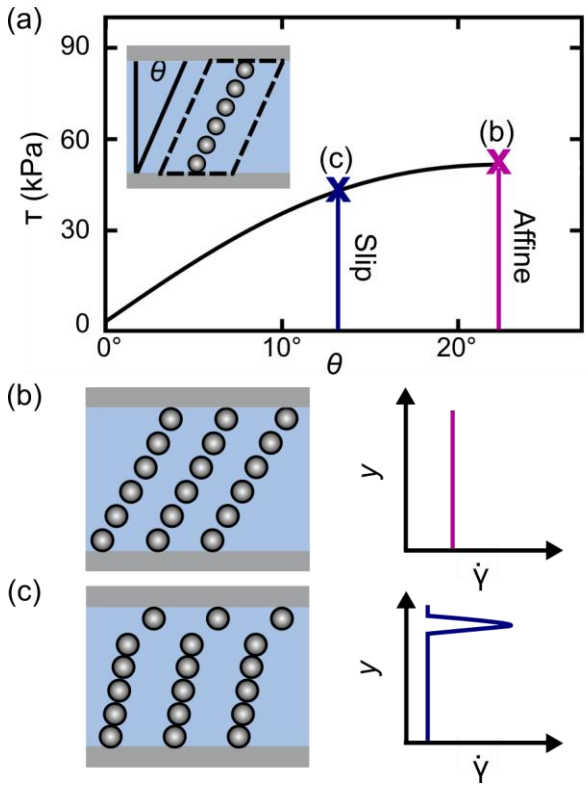

Figure 4.3 (a) When sheared, particle chains rotate by an angle θ and produce τ that can be estimated using a discrete dipole model. (b) Affine failure occurs at the maximum $\tau = \tau_0$ when further chain deformation results in decreasing τ. In this case, $\dot{\gamma}$ vs. height between the plates y should be constant. (c) For slip failure, particles will shear off the chain prior to the maximum possible τ_0 causing $\dot{\gamma}$ to increase significantly at the location of slip. As shear-thickening fluids exhibit increasing η_{eff} with increasing $\dot{\gamma}$, we hypothesize that this prevents slip failure.

In order to further explore the mechanism through which shear thickening improves MRF performance, we revisited the oscillation measurements to analyze them at greater depth and compare them to our model. In particular, we calculated phase lag $\delta = \tan^{-1}\left(\frac{G''}{G'}\right)$ for the two fluids which is plotted in Fig. 4.4 (a) and (b) as this is a measure of whether the material has a solid-like or fluid-like character. The trendline was generated using a Gaussian process regression (Machine Learning toolbox— MATLAB) with hyperparameters were initialized at one tenth of the range of each variable. Upon examination of δ vs. γ_0, a major difference was observed where the stMRF exhibited a monotonic increase and the cMRF had a local maximum above 45° (denoted by an arrow). We hypothesize that this low-strain shear melting could be related to slip failure. Critically, this low strain shear melting feature was absent for the stMRF in Fig. 4.4 (c) and present for all field strengths for the cMRF in Fig. 4.4 (d).

To confirm that the low strain shear melting of cMRF was due to slip failure, we performed a series of experiments at three gap heights h = 250, 500, and 1000 μm. In rheology, slip is a common experimental issue with particle suspensions and testing additional h is a way to determine the influence of slip.(Clasen and McKinely 2004, Meeker, Bonnecaze et al. 2004) Surface plots for all three h and both fluids revealed that the crossovers in Fig 4.4 (c) are unchanging with h for stMRF but decrease in strain with increasing h for the cMRF in Fig. 4.4 (d). In order to quantify this trend more precisely, the crossover strain (strain at which δ = 45°) was computed for the stMRF, converted to an angle using $\theta_c = \tan^{-1}(\gamma_0)$, and then plotted vs. h in Fig. 4.4 (e). Not only was this angle unchanging, but it was also within error of the 23° angle predicted by the chain model from

Fig. 4.3 (a), suggesting that stMRF fail in an affine manner. Here, error bars were obtained by averaging over all data in B > 0.03 T.

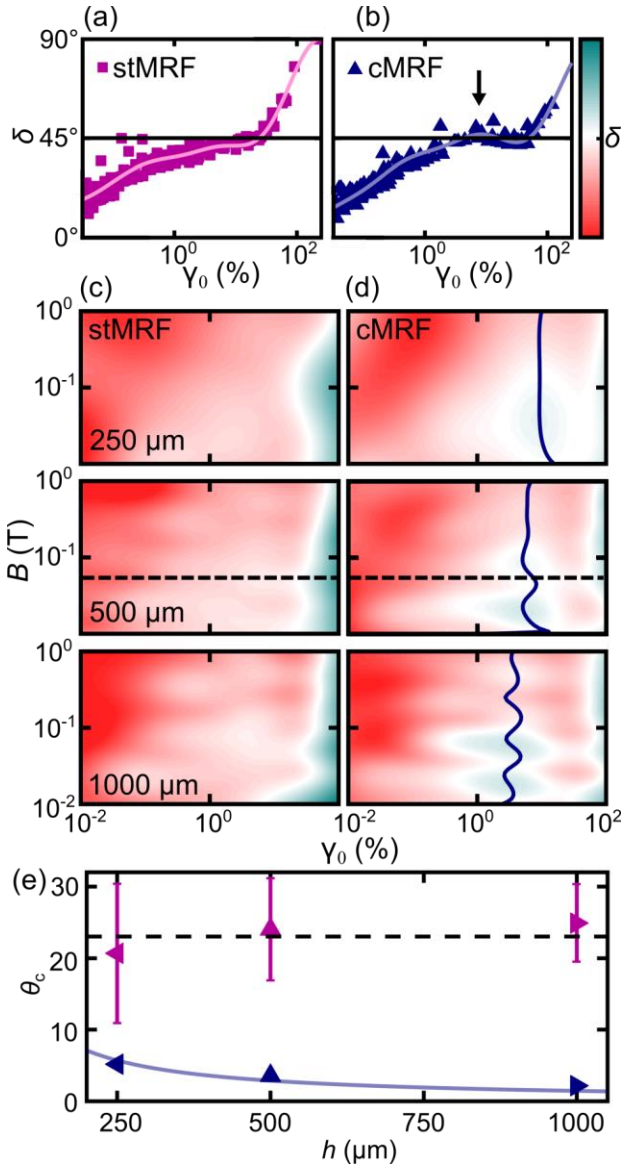

Figure 4.4 (a) The phase lag δ plotted at B = 50 mT vs. γ_0 for the stMRF which crosses over the liquid-solid transition line at $\delta = 45^\circ$ once. (b) δ vs. γ_0 plotted for the cMRF at B = 50 mT, which exhibits two crossover points with a local maximum indicated by the arrow. (c) Surface plots showing δ vs. B and γ_0 for the stMRF are shown at three plate separations h. All data was fit to Gaussian process regression to facilitate visualization. (d) Surface plots of δ vs. B and γ_0 for the cMRF. All fields and heights exhibit a maximum prior to affine failure, which is denoted with a blue line. Location of (a) and (b) on (c) and (d) are

indicated by dashed lines. (e) Critical chain angle θ_c plotted vs. h for both fluids with the theoretical θ_c indicated as the dashed line at 23°. The stMRF is within error of theory, while the cMRF has θ_c that changes with h as expected for slip failure, as shown by the trend line that is a fit to Equation 4.1.

While the stMRF exhibited yield that was consistent with affine failure, we sought to understand the nature of yield for the cMRF. Specifically, we computed the location of the local maximum in δ and converted this to an angle. Importantly, this angle was found to decrease with increasing h, in stark contrast to the stMRF. Hypothesizing that this variation was due to slip, the critical angle of failure should depend on the distance a particle would have to slide to slip loose from the chain, which likely does not vary with h.

In particular, we hypothesized that there is a specific Δx over which a particle must slide to slip apart from a chain. Based on this model, we expect the failure angle to be given by,

$$\theta_c = \tan^{-1}\left(\frac{\Delta x}{h}\right). \quad (4.1)$$

When this was used as a one parameter fit to the data for the cMRF, we found Δx = 25 ± 6.6 μm, which is on the order of the particle size. Collectively, this difference in behavior for the cMRF and stMRF highlighted the difference in their failure mechanisms.

4.5 Summary and Conclusions

A shear-thickening additive was used to synthesize a stMRF that was compared to a cMRF with same volume fraction of iron particles and found to exhibit yield stress improvement of 60% at B = 1 T in flow mode rheology and improvement in crossover stress of 68% at B = 1 T in oscillation-mode rheology. Through detailed study and

comparison with a model, this improvement was attributed to the prevention of slip failure in stMRF which allowed affine failure to determine the yield stress. These results show that shear-thickening additives improve MRF performance and reveal the mechanism of failure for both cMRF and stMRF. In addition to motivating the use of shear-thickening additives in an MRF, these results highlight the importance of considering both the rheology and microstructure when investigating smart fluids. Additionally, these improvements are indicative of better performance in engineering applications where increased yield stress can lead to increased torque or force output. This paradigm could find use in diverse complex fluids such as electrorheological fluids, ferrofluids, and particles on interfaces.

CHAPTER 5: ROLE OF 2D SHEETS IN PRESSURE- AND BOUNDARY-DRIVEN FLOWS

5.1 Current understanding of the influence of anisotropic additives on MRF performance

A fascinating and fruitful avenue of research in advanced MRF development has been the addition of particulate additives along with the standard magnetic microparticles to add new functionality or improve MRF performance.(Ashour, Kinder et al. 1997, Chin, Park et al. 2001, Kumar, Paul et al. 2019, Rendos, Woodman et al. 2020) The majority of work has focused on isotropic nanoparticle additives, which have been shown to improve MRF stability and, if the particles are themselves magnetic, strengthen the MRF when solidified.(Wereley, Chaudhuri et al. 2006, Kang Hyun, Bong Jun et al. 2009, Patel 2011) These successes motivate the study of more specialized nanomaterials as additives, such as anisotropic nanomaterials as anisotropy has been observed to tailor many properties from magnetic to rheological.(López-López, Vertelov et al. 2007, Samouhos and McKinley 2007, de Vicente, Vereda et al. 2010) For example, anisotropic magnetic particles will have a larger magnetic moment along their major axis than comparable spherical particles, which can improve chain strength and increase the yield stress in the solid state.(de Vicente, Vereda et al. 2010)

In contrast with isotropic additives, anisotropic additives in MRF have been studied to a limited extent and, aside from a reduction in sedimentation that can be understood as a jamming phenomenon,(Pu and Jiang 2005, Ngatu, Wereley et al. 2008, Jiang, Zhang et al. 2011, Zhang and Choi 2012, Chen, Zhang et al. 2014, Zhang and Choi 2014, Cvek, Mrlik et al. 2018, Wang, Ma et al. 2018, Xu, Xu et al. 2018, Wang, Zhou et al. 2019) there

has been no theoretical framework put forward to predict or understand the role of these anisotropic additives on MRF performance. Experimentally, the influence of additives on MRF performance is inconsistent, although direct comparisons are often absent. Despite the lack of a coherent picture, the existing experimental evidence gives reason to be optimistic that anisotropic additives can play a major role in MRF performance. For example, graphene oxide (GO) has been explored as an anisotropic plate-like additive due to its stability in aqueous solutions, ease of synthesis, and potential for post-synthetic modification. Specifically, an MRF was prepared with the most anisotropic additive studied so far, GO sheets with an aspect ratio of ~3000 (defined as characteristic width over thickness), and found to have similar shear stress compared to a fluid without GO sheets, albeit with the sheets reducing sedimentation.(Zhang and Choi 2012) However, when magnetic microparticles coated with GO were used to form a MRF, lower yield stresses were observed.(Chen, Zhang et al. 2014) Another study found that MoS_2 sheets provide no improvement in yield stress unless decorated with iron oxide nanoparticles which enabled 60% improvement, although this improvement could be due to the increase in total iron content.(Manzoor, Kim et al. 2018) Evidence from studies on nanowires also suggests that iron content may be the more critical factor in determining performance.(Ngatu, Wereley et al. 2008, Jiang, Zhang et al. 2011) Further complicating the picture, all previous studies on anisotropic additives in MRF have utilized shear-mode rheology while pressure-driven flows and those with complex non-linear shearing strain rate profiles are common in applications. Given the potentially large size of anisotropic additives, it is not clear whether the more complex shearing strain rate profile present in

pressure-driven flows will elicit the same behavior as boundary-driven flows. Hampering our understanding of these results is the lack of a theoretical model to predict the effect of such highly anisotropic additives that might serve to crystallize the apparently contradictory results.

5.2 Overview of our work on anisotropic additives

Here, we explore the influence of highly anisotropic 2D material additives on the performance of MRF by introducing α-$Ni(OH)_2$ 2D sheets with an aspect ratio of 25,000 to an otherwise conventional MRF. By comparing the magneto-rheology of a conventional MRF (cMRF) to that of an MRF containing 2D material (2DMRF) with the same iron content, we find little influence on performance in boundary-driven flow, but a significant influence in pressure-driven flow (Figure 5.1). Strikingly, the addition of the 2D material has a non-monotonic effect on the saturation pressure with increases up to 46% seen at low flow rates and reductions of up to 22% observed at faster flow rates or low magnetic fields. We propose a model based upon the modified Buckingham-Reiner equation that describes pressure-driven flow of a Bingham plastic to explain these results through a comparison between the thickness of the shear-melted region of the MRF and the size of the 2D material. Specifically, when the thickness of the yielded domain is commensurate in size with the 2D material, the MRF is strengthened. Agreement between the model and experiment highlights the value of using high aspect ratio 2D materials in fine tuning MRF and the opportunities inherent to the intersection of the fields of smart fluids and designer 2D materials. This work was published in *ChemPhysChem*.(Rendos, Li et al. 2020)

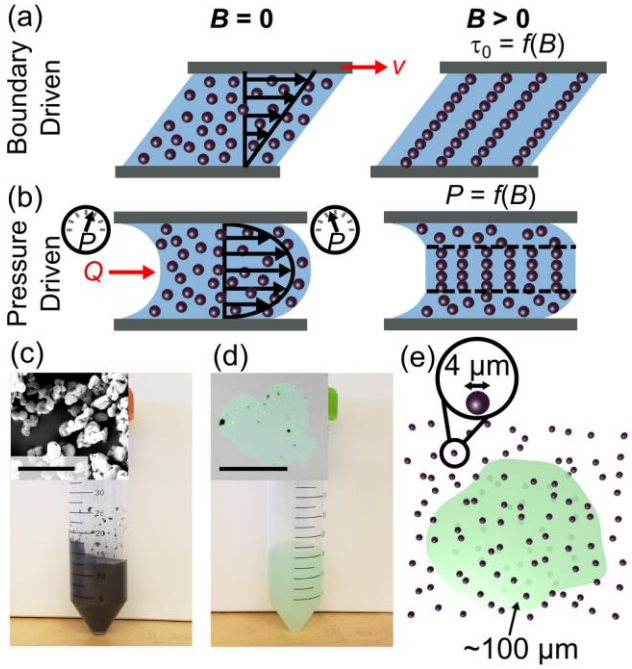

Figure 5.1 (a) MRF are commonly tested in boundary-driven flow with a stationary bottom plate, and top plate with velocity v. When $B > 0$ the chains align and exhibit a characteristic τ_0 which varies with B. (b) MRF in pressure-driven flow with flow rate Q and pressure drop P. When $B > 0$, P varies with B due to formation of chains in the center of the flow. (c) Image of conventional aqueous MR fluid (cMRF) with an inset showing a scanning electron micrograph of magnetic carbonyl iron particles. Scale bar is 20 μm. (d) Image of α-$Ni(OH)_2$ sheets dispersed in water with an inset showing an optical micrograph of a single α-$Ni(OH)_2$ sheet. Scale bar is 100 μm. (e) Scheme of a suspension of 2D material with iron particles that are drawn to scale.

5.3 Results of flow-mode rheology of conventional MRF and MRF with 2D sheets

Two smart fluids were prepared to allow for a direct comparison of bulk properties in order to extract the role of 2D material additives on MRF performance. Specifically, a suspension of 14.2 vol% carbonyl iron microparticles was prepared in water and 0.25 wt% xanthan gum was added to slow sedimentation. The resulting fluid shown in Fig. 5.1 (c) was denoted cMRF. In addition, a suspension of the same 14.2 vol% carbonyl iron microparticles was prepared in water and mixed with α-$Ni(OH)_2$ 2D sheets with a 0.17%

final weight percentage to create 2DMRF. The α-$Ni(OH)_2$ 2D sheets used in 2DMRF and shown in Fig. 5.1 (d) are stable in water and are ~100 μm in size with a 4 nm thickness. It is worth emphasizing that the iron microparticles are much smaller in radius than the 2D material, as shown in the scale schematic in Fig. 5.1 (e). Subsequently, the final 2DMRF formulation required addition of 0.15 wt% xanthan gum to make the zero-field rheology as similar as possible to cMRF. These fluids, namely cMRF and 2DMRF, were prepared to have the same final iron content as this is known to be a key determinant of performance.

Initially, cMRF and 2DMRF were tested using shear-mode rheology as depicted for the 2DMRF in Fig. 5.2 (a), which is the standard approach for characterizing smart fluid performance. Here, fluids are confined between two parallel circular platens, and the top plate rotates relative to the fixed bottom plate. Before applying B, the fluids were characterized by measuring their effective viscosity η_{eff} vs. $\dot{\gamma}$ which is plotted in Fig. 5.2 (b), which confirmed that both fluids have very similar rheological properties and exhibited shear-thinning behavior, which is common for particle suspensions.(Jolly, Bender et al. 1999, Mueller, Llewellin et al. 2009) The τ vs. $\dot{\gamma}$ for each fluid was measured at B = 0.2 T by applying the field and then increasing $\dot{\gamma}$ while measuring τ as shown in Fig. 5.2 (c). The resulting data sets were fit to the Bingham plastic constitutive model and both fluids exhibited similar τ_0. This data collection and fitting process was repeated for both fluids at thirteen B logarithmically spaced between 0.005 and 1 T and repeated four times at each field strength. The resultant values of τ_0 vs. B in Fig. 5.2 (d) revealed that there is little difference between the two fluids, especially at high B where τ_0 began to saturate due to the magnetic saturation of the iron microparticles. Interestingly, in the low B limit, the

fluids differed in a manner that is highlighted in Fig. 5.2 (e) when the ratio of the 2DMRF yield stress τ_0^{2D} to the cMRF yield stress τ_0^c is plotted. We hypothesized that the decrease in τ_0 is due to the large 2D sheets interfering with chain formation at low fields when the magnetic dipole-dipole interaction strength is low. Despite the small differences at low fields, both fluids had very similar high field MR performance when tested in boundary-driven flow, indicating that the 2D material was not playing a major role.

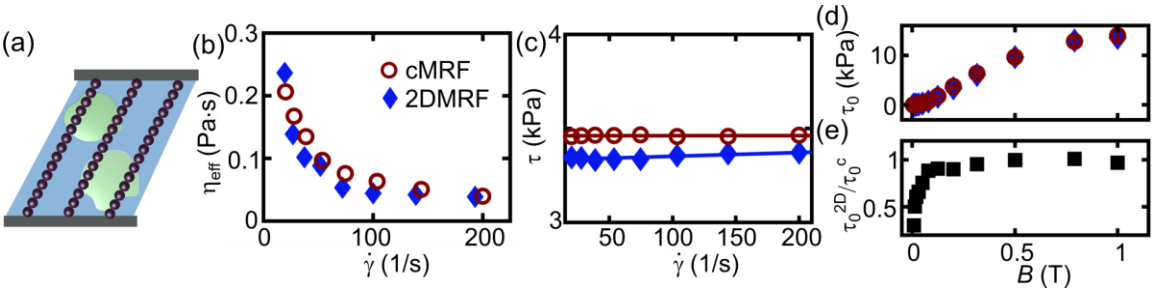

Figure 5.2 (a) Schematic of MR fluid with 2D material (2DMRF) in between the plates of a rheometer. (b) η_{eff} of cMRF and 2DMRF vs. $\dot{\gamma}$. (c) τ vs. $\dot{\gamma}$ with Bingham plastic linear fit for cMRF and 2DMRF at B = 0.2 T. (d) τ_0 vs. B for M1 and M2 using shear rheology and Bingham plastic fit. Each point represents an average of four trials with standard deviation shown as error bars. (e) Plot of 2DMRF yield stress τ_0^{2D} over cMRF yield stress τ_0^c shows τ_0 beginning to differ at low B where the 2DMRF is lower than the cMRF.

5.4 Flow-rate dependent performance of fluids in pressure-driven flow

While the flow mode results were initially surprising, we hypothesized that the lack of an effect at high fields was due to strong particle-particle interactions and flow rotating the sheets such that their faces are parallel with the chains. Indeed, in this case, the two forces that could lead to sheet rotation—namely hydrodynamic forces due to fluid velocity gradients and forces from the particles moving to form chains—are both minimized when the sheets adopt this configuration. While this may be the case for simple boundary-driven flows, these are by no means the only or most common types of flows when considering

smart fluids. For example, another major category of fluid flow is pressure-driven or Poiseuille flows in which a pressure drop *P* drives a flow with total volumetric flow rate *Q*. For simple fluids, such flows adopt a quadratic profile, while for Bingham plastics such as an MRF in an applied field, these adopt a plug-flow with a solidified central region and a toroidal melted region along the edge. This type of flow is not an academic curiosity as smart fluids are very commonly used in this configuration as valves. Thus, while 2D sheets had a minimal effect on simple boundary-driven flow, the question of how these highly anisotropic additives affect more complex pressure-driven flow remained unclear.

In order to realize parabolic flow with a region containing a uniform magnetic field, a custom flow apparatus was developed. Specifically, a syringe pump was used to pump fluid at constant *Q* through a 2 mm inner diameter tube between two permanent magnets that were positioned using micrometers as depicted in Fig. 5.3 (a). Importantly, the magnets were mounted on hinged platforms so they could be rapidly swung into and out of position as a method of engaging or disengaging the field. The pressure up-stream of the resultant high field region was measured using a capacitive pressure sensor and recorded using a DAQ to provide a measure of *P* vs. time *t*. In a typical experiment, a *P* trajectory revealed a sequence of shifts related to the changing experimental conditions. As seen in an example in Fig 5.3 (b), $P \sim 0$ as the syringe pump had yet to be engaged. Once engaged, *P* rose to a constant value that corresponded to the pressure needed to accommodate the programmed *Q*. At a fixed time t_B, the magnets were tilted into position to increase *B* to its set point value. After 20 s, the magnets were disengaged and the syringe pump was switched off. Critically, this process allowed for the determination of the saturation pressure P_0 that

corresponded to the asymptotic pressure while B was engaged, here found to be 108 kPa for cMRF with B = 0.11 T and Q = 6 mL/min.

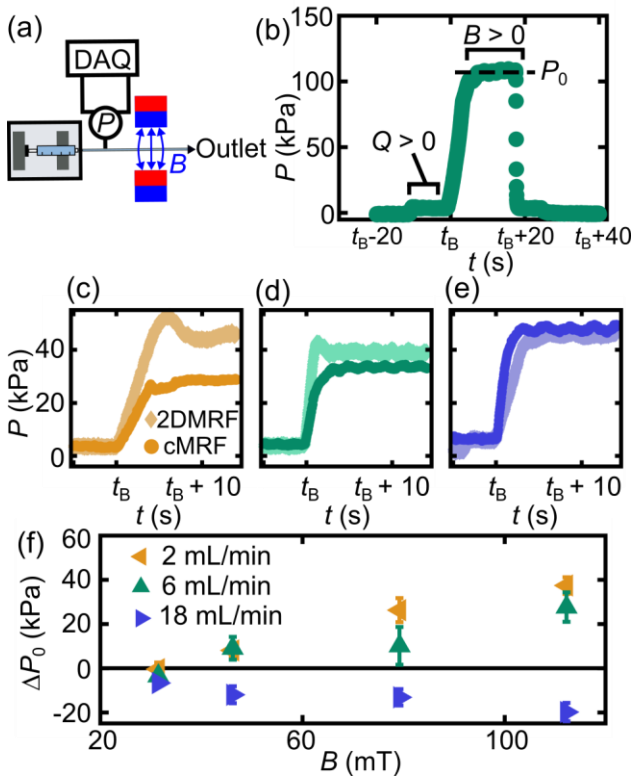

Figure 5.3. (a) Schematic of flow apparatus. Syringe pumps fluid into tube, passes through pressure sensor to measure P which is recorded by a data acquisition system (DAQ) and then flows between two movable magnets with B before exiting the tube. (b) Typical P vs. time t when B = 0.11 T which shows the fluid initially at rest and the resulting pressure increase as the flow rate Q is turned on, and then as B is turned on at t_b. The average pressure observed with $B > 0$ is denoted the saturation pressure P_0. The experiment is completed by sequentially turning off B and Q. (c), (d), (e) P vs. t for Q = 2, 6, and 18 mL/min, respectively. All plots show both results using cMRF and 2DMRF with B = 0.08 T. (f) Change in saturation pressure between the 2DMRF and cMRF ΔP_0 vs. B for both fluids at all B tested.

Having realized a system to quantify performance of MRF in pressure-driven flows, we sought to compare the two fluids to determine the effect of 2D materials. Specifically, the measurement scheme was repeated and plotted in Fig. 5.3 (c), (d), and (e) for Q = 2, 6, and 18 mL/min and at B = 46 mT. In contrast with boundary-driven flow, these flows

exhibited a significant difference between the two fluids, particularly at the lowest flow rate shown in Fig. 5.3 (c) where 2DMRF outperformed cMRF by ~20 kPa. Interestingly, that trend reversed as the flow rate increased and P_0 measured for cMRF surpassed that of 2DMRF at 18 mL/min in Fig. 5.3 (e). In order to further explore this, additional experiments were performed for both fluids at all three values of Q and at B = 0.032, 0.046, 0.08, and 0.11 T. Strikingly, the difference in saturation pressure ΔP_0 between 2DMRF and cMRF in Fig. 5.3 (f) revealed that this flow-rate dependence is further exacerbated at higher fields. Specifically, the addition of the 2D sheets increased P_0 by 40 kPa at the highest B tested, in stark contrast with our results from boundary-driven flow. However, at 18 mL/min, the 2D sheets decreased P_0 by 20 kPa in apparent contrast with the results at low Q. It should be noted that typically MRF in pressure-driven flows are used to modulate pressure drop with applied field so an increase in P_0 can be construed as improvement in performance, which makes the inconsistent results important to understand.

5.5 The role of additive length scale in performance improvement determined by model based on Buckingham-Reiner equation

To understand these apparently conflicting results in pressure-driven flow, we performed a theoretical analysis of the pressure-driven flow environment. Specifically, the Buckingham-Reiner model is typically used to describe a Bingham plastic flowing in a cylindrical pipe.(Bird, Dai et al. 1983) This model predicts an unyielded "plug" at the center of the tube with a yielded region at the edge of the tube with width L_y as shown in the schematic in Fig. 5.4 (a) and relates Q with P_0 through:

$$Q = \frac{\pi P_0 R_T^4}{8\mu_{eff} L}\left(1 - \frac{4}{3}\frac{\tau_0}{\tau_R} + \frac{1}{3}\left(\frac{\tau_0}{\tau_R}\right)^4\right). \quad (5.1)$$

Here, $\tau_R = \frac{P_0 R_T}{2L}$ describes the wall shear stress, R_T is the radius of the tube and L is the length of the tube. It should be noted that if $\tau_0 = 0$, this expression reduces to the standard expression for Poiseuille flow of a simple fluid. The first question to address is whether the MRF in this study behave as Bingham plastics. Fortunately, the boundary-driven experiments in Figure 5.2 provide independent estimates for the Bingham plastic parameters τ_0 and μ_{eff}, which allowed for a theoretical prediction of P_0 based just on these values and the geometry of the custom flow apparatus for a given Q. In Fig. 5.4 (b), the theoretical prediction matches the data for cMRF well, confirming that MRF is behaving as a Bingham plastic. Interestingly, P_0 for the 2DMRF fell above this line, indicating that the cause of this increase is not captured by the Bingham plastic model.

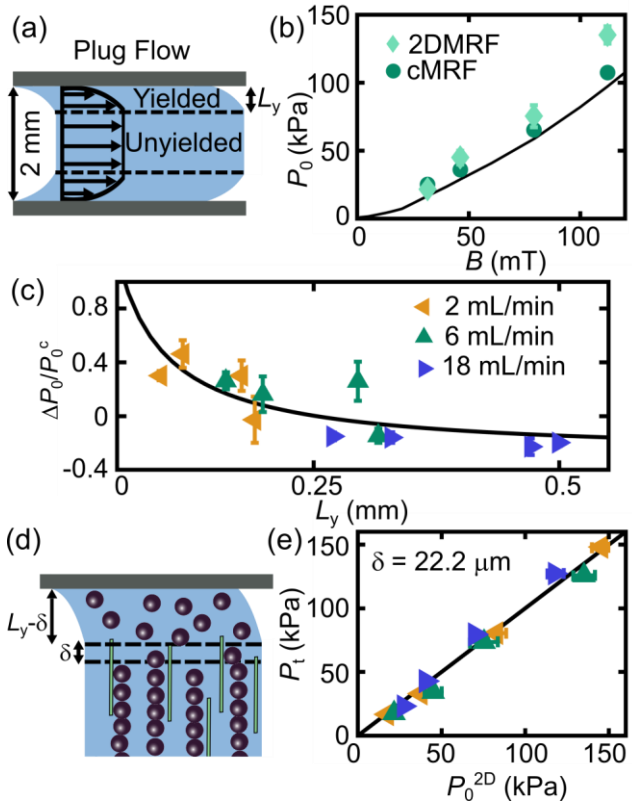

Figure 5.4 (a) Schematic of plug flow exhibited by a Bingham plastic with unyielded region as the plug in the center and the yielded length indicated as L_y. (b) P_0 vs. B for cMRF and 2DMRF at Q = 6 mL/min with Buckingham Reiner analytical solution for Bingham plastic in plug flow plotted as the black line.(c) ΔP_0 normalized by saturation pressure of the cMRF P_0^c vs. L_y and fit to power law. (d) Hypothesized effect of 2D material to decrease L_y by length δ. (e) Plot of theoretical pressure P_t by incorporating $\delta = 22.2\ \mu$m vs. saturation pressure of 2DMRF P_0^{2D} for all three flow rates with line indicating excellent agreement between theory and experiment.

We hypothesized that the change in P_0 associated with the 2D material may be due to the finite length scale associated with the 2D material. In the Buckingham-Reiner model, L_y is an obvious candidate for an important length scale, which can be computed as:

$$L_y = R_T - \frac{2L\tau_0}{P_0}. \tag{5.2}$$

Thus, we sought to determine if the effect of 2D material had a correlation with L_y. To explore this, ΔP_0 for all data was normalized by P_0^c and plotted *vs.* L_y calculated for cMRF

in Fig. 5.4 (c). Strikingly, these data adopted a consistent trend with smaller L_y corresponding to an increase in ΔP_0 and larger L_y converging to a slight decrease in ΔP_0. To fit this data, we performed non-linear least squared fitting to the empirical expression:

$$\frac{\Delta P_0}{P_0^{M1}} = \left(\frac{a}{L_y}\right) - b, \tag{5.3}$$

and find a = 74 $\pm$ 20 μm, b = 0.293 $\pm$ 0.11. Critically, the length scale parameter of 74 μm is on the order of the 2D sheet size of 100 μm. Thus, these empirical results showed that when L_y is commensurate in size with the 2D sheets, P_o increases.

In order to explain the effect of 2D sheets on MRF, we hypothesized that they become stuck in the plug and protruded into the yielded region, effectively increasing the width of the plug by a set distance δ, leading to a decrease in L_y as shown in Fig. 5.4 (d). In order to test this hypothesis, the theoretical pressure drop P_t was calculated for various δ and compared to P_0^{2D} by varying the yield stress and keeping the flow rates and geometric parameters fixed. The mean-squared error between the P_t calculated with Bingham plastic parameters for cMRF and experimental $P_0{}^{2D}$ was calculated to identify the δ that best corresponded to the results from 2DMRF which is δ = 22.2 μm. P_t vs. P_0^{2D} was plotted in Fig. 5.4 (e) for δ = 22.2 μm to show the close correlation between theory and experimental data assuming the yielded region is reduced by this amount which is on the order of the size of the 2D material. The success of this model in recapitulating the experiment data confirmed our interpretation of how the 2D material alters the structure of the fluid in pressure driven flow and suggested the size of the sheet is important when selecting anisotropic additives for smart fluids. We also note that the decrease in P_0 at high

Q agreed with the decrease in τ_0 that was observed in low-field boundary-driven rheology results and averaged to be 22%, which matches the 22 ± 4% average decrease present at 18 mL/min. These results not only confirmed the ability of 2D sheets to positively affect MRF performance, they also provided a guide for understanding the nuanced cases in which the sheets will improve, reduce, or have no effect on performance.

5.6 Summary and conclusions

The detailed comparison of MRF with and without highly anisotropic α-$Ni(OH)_2$ 2D sheets allowed us to tease out the intricate effects of anisotropy and construct a model explaining these influences. In boundary-driven flow, both fluids exhibited nearly identical rheological properties and performance, with the 2D material only leading to small differences in τ_0 at low fields, which we attributed to the large sheets inhibiting particle chain formation. When testing both fluids in pressure-driven flow, the performance was significantly influenced by the 2D sheets. At low flow rates, the 2D material provided up to 46% improvement in performance, however at the highest flow rate, the 2D material caused a 22% reduction in performance. These results were explained by modifying the standard plug-based flow inherent to Bingham plastics. Specifically, we postulated that the addition of 2D material physically reinforces the plug and expands it into the melted region by a distance commensurate with the 2D material size. These results highlight the potential for anisotropic additives to affect MRF performance in varying ways depending on the type of flow and length scales present in the system. Additionally, this work connects the microstructure of the particle constituents to the bulk properties of the fluid which can inform other studies of smart fluids and nanoparticle suspensions more generally.

CHAPTER 6: EFFECT OF ADHESIVE MAGNETIC PARTICLES ON MRF PERFORMANCE

6.1 Prior work on chemically-adhesive chains in MRF

While tuning the particles or soluble additives have been important for increasing τ_0 and reducing sedimentation, the interface between the particles and the medium has received comparatively little attention outside of its role in maintaining colloidal stability. In particular, when the particles are magnetically held together in the solid-like state, particle-particle contacts occur and the particles will chemically and sterically interact. The nature of this interaction and its effect on MRF performance has not been extensively studied but a few key requirements are clear. For MRF to reversibly form in the presence of a magnetic field — or even rearrange upon shear-induced melting — it is crucial that the bonds be reversible. Indeed, reports of iron particles that were polymerized into magnetic fibers showed a 30% decrease in τ_0.(Kuzhir, López-López et al. 2007, López-López, Vertelov et al. 2007) In contrast, reversible adhesion, such as that provided by hydrogen bonding, could provide an additional short ranged force to strengthen solidified particles (Fig. 6.1(a,b)). Indeed, early experiments using guar gum to coat magnetic particles resulted in a τ_0 increase of up to 40% which the authors attributed to hydrogen bonding between particles mediated by the guar gum.(Wu, Zhao et al. 2006) However, these results are complicated by the roughening effect of the guar gum coating. Specifically, the increase in τ_0 was observed to be strongest in cases when the particles were functionalized non-uniformly with sparse amounts of guar gum. Further functionalization that led to more uniformly functionalized particles resulted in a smaller increase in τ_0. Thus, further study is needed to isolate the effect of reversible chemical

adhesion on MRF performance.

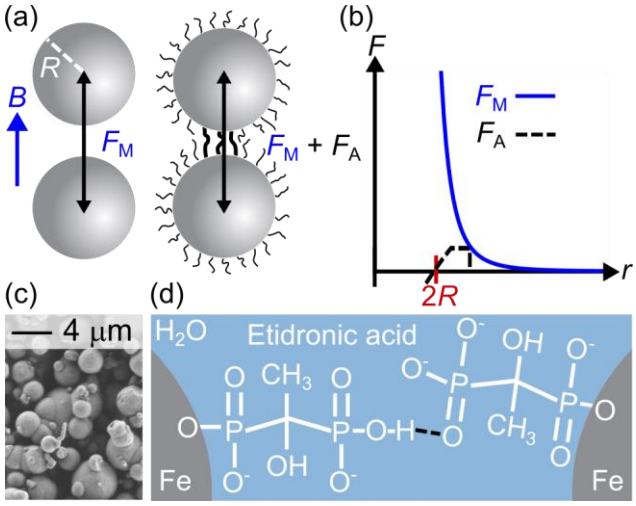

Figure 6.1 (a) When magnetic particles with radius R are aligned with B, they interact through the attractive magnetic dipole-dipole force F_M. Functionalized particles will have an additional attractive chemical adhesion force F_A. (b) F_A is a short-ranged force that is maximum when particles are separated by r and falls to zero as r increases. F_M scales as r^{-4}. (c) Scanning electron micrograph of carbonyl iron particles (d) Bonding scheme for phosphonate-functionalized magnetorheological fluid (pMRF) prepared through etidronic acid functionalization. Hydrogen bonds are indicated with dashed black lines.

6.2 Overview of effect of adhesive force on MRF performance

Here, we explore the influence of adhesive surface functionalization on the performance of MRF through rheological testing. We initially focus on particles functionalized using etidronic acid, which is a small molecule that is expected to produce hydrogen bonding between phosphonate groups. Flow- and oscillation-mode experiments show that this phosphonate MRF (pMRF) exhibits up to a 40% increase in τ_0 and a 100% increase in stiffness relative to uncoated, conventional MRF (cMRF). Interestingly, the relative τ_0 enhancement decreased as φ increased. We propose a model to explain the φ dependence of τ_0 attributing it to the differing structure of particle assembly from isolated chains at low φ to a continuous body-centered tetragonal (BCT) structure at high φ where

the adhesive force F_A is no longer aligned with the applied field. Building on this understanding, we hypothesize that it is possible to chemically switch between non-adhesive and adhesive particles using a second functionalization strategy in which the particles are coated with a thymine-presenting polymer that cross-links in the presence of melamine. Indeed, this functionalization strategy leads to a similar strengthening and stiffening as in the pMRF, but only in the presence of soluble melamine. The consistent results of these two systems along with the chemical tunability of the latter highlight novel routes for imparting stimuli responsiveness in smart fluids by chemically tuning particle interfaces.

6.3 Results from flow-mode and oscillation-mode rheology of MRF functionalized using etidronic acid

In order to determine the influence of adhesive particles on MRF performance, pMRF and cMRF were compared using flow-mode rheology. Measured τ exhibited by each fluid increased with φ, as shown in Fig. 6.2(a) for cMRF, and also increased dramatically with B. To quantify τ_0, τ was measured *vs.* $\dot{\gamma}$ as shown in Fig. 6.2(b) for both the cMRF and pMRF. This data was fit to the Bingham plastic constitutive model, described in Eq. 2.30. By repeating the measurements in Fig. 6.2(b) for logarithmically spaced B between 0.03 and 0.8 T, τ_0 was plotted *vs.* B to compare both fluids. As shown in Fig. 6.2(c) for φ = 2 vol%, pMRF exhibited a higher τ_0 than cMRF for all B tested. For each condition, three trials were conducted and averaged. After repeating this process for all φ, the percent increase in τ_0 due to the adhesive functionalization was calculated and plotted in Fig. 6.2(d). These data clearly show that the adhesive functionalized particles

increased τ_0 by up to 40%, but in a φ-dependent manner with sparse particle suspensions exhibiting greater strengthening. While the nature of the φ-dependence was not clear, the increase in τ_0 validated the hypothesis that additional adhesive force strengthened the solidified MRF.

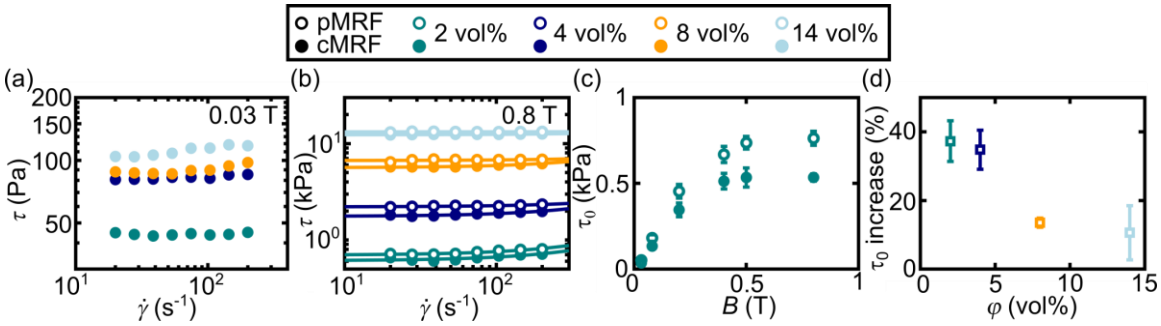

Figure 6.2 (a) Representative plots of τ vs. $\dot{\gamma}$ for conventional MRF (cMRF) when B = 0.03 T for φ = 2, 4, 8, and 14 vol% measured using flow-mode rheology. (b) Comparison of τ vs. $\dot{\gamma}$ between representative curves of pMRF and cMRF for all φ at B = 0.8 T, the highest B tested. Data was fit using the Bingham plastic model from Eq. 2.30 used to quantify the τ_0. (c) τ_0 vs. B for φ = 2 vol% shows the increase in performance of pMRF compared to cMRF at all field strengths. (d) Percent increase in τ_0 of pMRF relative to cMRF averaged over all B for each φ.

Due to the added adhesive force for assembled particles, we hypothesized the solidified pMRF would exhibit higher stiffness than cMRF, which is another important performance metric for MRF applications.(Li, Du et al. 2002, Li, Zhang et al. 2005, Sun, Tang et al. 2019) In order to quantify the stiffness of the assembled particles, oscillation-mode rheology was used. In oscillation mode, shown in Fig. 6.3(a), the rheometer top plate oscillated back and forth in a τ-controlled measurement where τ was applied and the strain γ of the assembled particles was measured so that G' and G'' of the material could be quantified. A representative plot of G' and G'' for the cMRF is shown in Fig. 6.3(b). While high τ behaviour can be used to determine the onset of shear melting, the stiffness of the

material is defined as the plateau G' at low τ. To compare the stiffness for the two fluids, G' *vs.* τ was measured for φ = 2 and 8 vol%. In Fig 6.3(c), pMRF was observed to exhibit higher G' than the cMRF. The stiffness was quantified by fitting the plot of G' in loglog space to a power law with a *y*-offset which represented the extrapolated plateau G_0,

$$\log(G') = a * \log(\tau)^n + G_0 \quad (6.2)$$

where *a* and *n* were additional fitting parameters. Interestingly, the pMRF plateau stiffness G_0^p was about twice as large the cMRF plateau stiffness G_0^c for both φ, as shown by their ratios in Fig. 6.3(d).

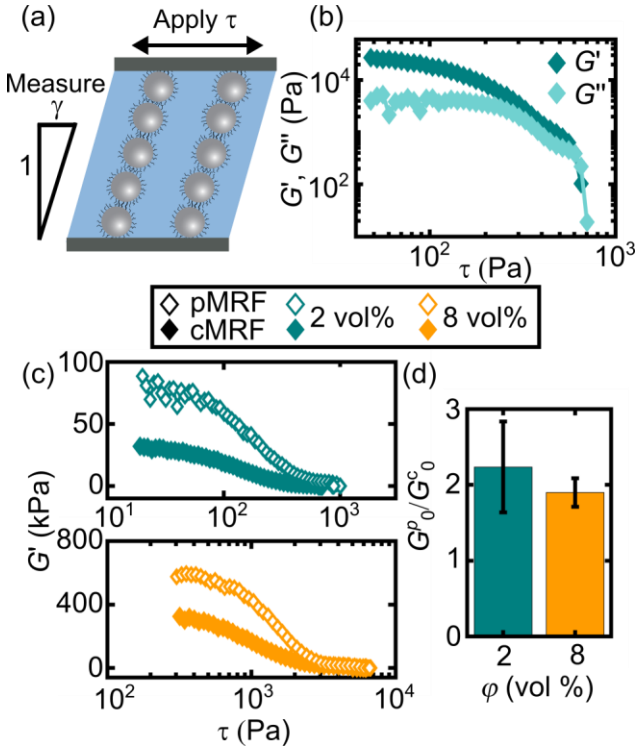

Figure 6.3 (a) Scheme of oscillation-mode rheology. An oscillating τ was applied to the top plate and gradually increased while the strain γ was measured. (b) An example plot of the data gathered from oscillation mode for the cMRF at B = 0.5 T where G' and G'' were determined as a function of τ. (c) Plots comparing G' vs. τ for pMRF and cMRF at φ = 2 and 8 vol%. The pMRF exhibited significantly higher G' plateau at low τ. (d) Plot of the plateau storage modulus for pMRF G_0^p divided by the plateau storage modulus for cMRF

G_0^c for φ = 2 and 8 vol%. Error bars depict the error from the standard deviation of three trials of each fluid at each φ.

6.4 Influence of microstructure on performance

While the flow and oscillation-mode testing revealed that adhesive functionalization strengthened and stiffened the MRF, the strenghening was strongly φ dependent with τ_0 decreasing as φ increased. In order to understand this dependence, we considered how the structure of the particle assembly changes as φ increases. For low φ, MRF is understood to solidify through a series of isolated particle chains as depicted in Fig. 6.4(a) with a height determined by the rheometer gap. As a result, the magnetic dipoles that align with B were also in alignment with F_A so that both magnetic and adhesive contributions were acting in the same direction. However, at higher φ, MRF are known to form colums of BCT solids as shown in Fig. 6.4(b) due to interactions between neighboring chains causing isolated chains to combine.(Tang and Conrad 2000, Chin, Park et al. 2001, Tao 2001) Interestingly, MRF chains have been observed to interact and start forming columnar structures in both simulation and experiment at φ > 5 vol%(Fernández-Toledano, Rodríguez-López et al. 2014, Rodriguez-Lopez, Castro et al. 2015) which indicates that the transition from isolated chains to BCT columns is expected in range of φ tested here. In this BCT structure, the interparticle contacts were no longer in the direction of the applied field, meaning that F_A was also no longer aligned with the applied field. Therefore, as the chains were sheared, the F_A between particles breaks at lower γ than F_M and contributed less to the strength of the assembled particles during failure. This likely explained why the strenthening associated with chemical adhesion decreased as φ increased, whereas the increase in G_0 was similar between the two structures due to the

stiffness being measured at very low γ when the chains or columns are mainly intact.

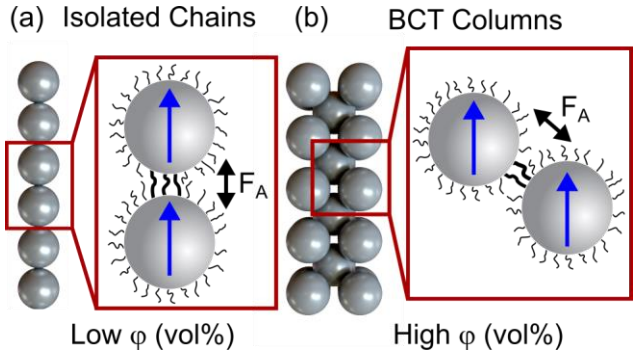

Figure 6.4 (a) Scheme of isolated chains in an MRF at low φ. Within the isolated chains, the particles were aligned with the field due to the dipoles indicated in blue. F_A was also aligned with the field, enabling a stronger contribution from F_A to the strength of the chains. (b) Scheme of body-centered tetragonal (BCT) structure expected for high φ MRF. Due to the structure, F_A was not aligned with the dipoles causing the contribution from F_A to be lower than for isolated chains.

6.5 Leveraging hydrogen bonding to make dynamically linkable MRF

Taking inspiration from the strengthening and stiffening observed for chemically-adhesive paticles, we hypothesized that we could leverage the dynamc tunability of chemistry to add additional stimuli responsiveness to MRF. Specifically, if the chemical adhesion of the particles could be modulated chemically, this could translate to large changes in the stiffness and strength of the solidified MRF. Thus, we synthesized tMRF, which was functionalized to present a thymine group. Without an additional linking molecule such as melamine, this is not expected to interact through hydrogen bonding. However, in the presence of melamine, these particles are expected to exhibit hydrogen bonding (Fig. 6.5(a)). To explore this idea, two systems were prepared, tMRF without melamine and tMRF with melamine (tMRF + mel). In contrast with the pMRF system,

requiring a linking molecule for bonding endowed the system with more tunability and stimuli-responsiveness.

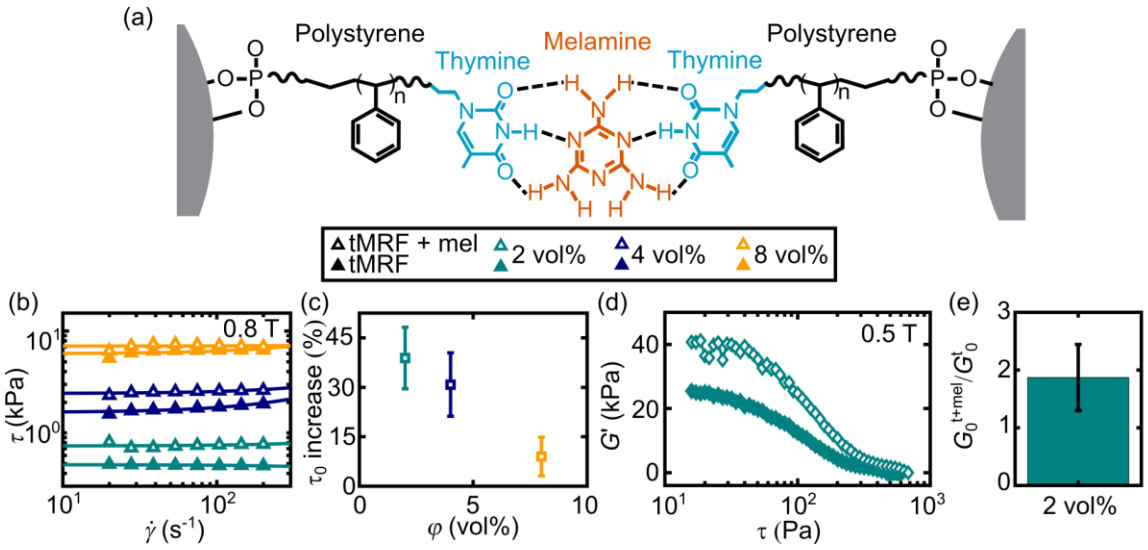

Figure 6.5 (a) Bonding scheme for the thymine-functionalized MRF that was linked using the small molecule melamine (tMRF + mel). The thymine groups were attached to polystyrene-functionalized carbonyl iron particles. (b) Representative curves for τ vs. $\dot{\gamma}$ for the thymine-functionalized MRF (tMRF) and tMRF + mel at B = 0.8 T fit using Eq. 2.30. (c) Percent increase with error propogated from three trials taken for each fluid at B = 0.8 T for φ = 2, 4 and 8 vol%. (d) From oscillation-mode measurements, G' vs. τ for φ = 2 vol% at B = 0.5 T. (e) Plot of the plateau storage modulus for tMRF + mel G_0^{t+mel} divided by the plateau storage modulus for tMRF G_0^t for φ = 2 vol%.

Flow-mode and oscillation-mode rheology were performed for the thymine-based system in order to contrast its behavior to the behavior of the pMRF. In Fig. 6.5(b), examples of τ vs. $\dot{\gamma}$ for the tMRF and tMRF + mel were included for B = 0.8 T and again fit to Eq. 2.30. In all cases, tMRF + mel exhibited higher τ_0 than the tMRF and the percent increase is shown in Fig. 6.5(c) for φ = 2, 4, and 8 vol%. As with the pMRF, the percent increase in τ_0 was about 40% for φ = 2 vol% and decreased with increasing φ, suggesting that the mechansism of strengthening was the same. Additionally, oscillation-mode measurements were conducted for φ = 2 vol%, as shown in Fig. 6.5(d), and were used to

calculate the difference in stiffness between tMRF and tMRF+mel. The plateau stiffness G_0^{t+mel} of tMRF with melamine was twice as large as the plateau stiffness G_0^t of tMRF without melamine, in agreement with the comparison between pMRF and cMRF. Collectively, these results show that the tMRF+mel successfully maintained the same stiffening and strengthing as pMRF, but with a more flexible, dynamically linkable system.

6.6 Summary and conclusions

Taken together, this work shows the potential for increasing performance metrics and introducing tunability of MRF through responsive surface coatings. Specifically, the performance of MRF with chemically-adhesive particles were compared to the performance of MRF formed by non-adhesive particles. In brief, chemically-adhesive particles drastically stiffened the solidified MRF in a manner independent of $\boldsymbol{\varphi}$. While these coatings also strengthened MRF by as much as 40%, this strengthening decreased as the $\boldsymbol{\varphi}$ increased. We attributed this decrease to the topological change between isolated chains and BCT solids as $\boldsymbol{\varphi}$ increased. It should be emphasized that the the fact that a small molecule can impart such a large change on the bulk performance of particles that are trillions of times their mass showcases the importance of tuning particle surfaces. In addition, this work highlights chemical tunability as an underutilized way with which to dynamically tune the properties of MRF and smart fluids more generally. Such chemical interactions could be utilized to locally tune the mechanics of MRF and even tune the temperature dependence of MRF properties.

CHAPTER 7: THE ORIGIN OF THE ELECTRIC FIELD INDUCED MACROSCOPIC CELLULAR PHASE

7.1 Overview of typical particle assembly in electric fields and the electrorheological effect

Electric fields provide a flexible means to manipulate soft matter, however, they interact with materials in electrolytic solutions through numerous distinct phenomena making the outcome of field-directed assembly difficult to predict. Typically, when a suspension of polarizable particles experiences a spatially uniform electric field, their induced dipoles lead them to form isolated chains along field lines, causing solidification through the electrorheological effect where the rheological properties can be tuned by adjusting the field strength.(Furedi and Valentine 1962, Hao 2001, Park and Saintillan 2011) The materials formed during the electrorheological effect are not continuous in that individual chains or columns are not connected to their neighbors. This common particle assembly mirrors the assembly of particles into chains in MRF and produces electrorheological fluids (ERF).

7.2 Prior observations of the cellular phase

In contrast to particle chaining, suspensions have also been experimentally observed to assemble into macroscopic porous structures with particle-rich walls and particle-poor voids,(Trau, Sankaran et al. 1995, Sapozhnikov, Tolmachev et al. 2003, Kumar, Khusid et al. 2005, Agarwal and Yethiraj 2009, Hardt, Hartmann et al. 2020) even though this phase has not been completely recapitulated in simulation.(Almudallal and Saika-Voivod 2011, Park and Saintillan 2011, Tiribocchi, Montessori et al. 2021) Interestingly, these cellular phase structures do form continuous materials in that the walls

form a two-dimensional network that extends across the entire region. Further, the size of the pores – both the voids formed by the cells and the space between particles in the particle-rich walls – can be controlled, indicating that these cellular phases have the potential to become hierarchically structured mesoporous materials. While these porous structures suggest a path to realizing continuous mesoporous solids with extremely low densities, the origin of this phase is not clear even though, and perhaps because, the cellular phase was observed in vastly different systems spanning orders of magnitude in particle size, particle volume fraction, and electric excitation which are all summarized in Table 7.1. While electrohydrodynamic (EHD) flow was identified as the primary mechanism of formation in two instances(Trau, Sankaran et al. 1995, Sapozhnikov, Tolmachev et al. 2003) and electroosmotic (EO) flow in another,(Hardt, Hartmann et al. 2020) the other two examples list the interactions between induced dipoles as the origin of the structure.(Kumar, Khusid et al. 2005, Agarwal and Yethiraj 2009) Overall, the lack of a cohesive and encompassing explanation for the formation of the cellular phase hinders the ability to design macroscopic porous structures.

Table 7.1 Summary of experimental conditions and materials used for previous studies of the cellular phase and this current work.

Paper	Particle type	Particle diameter	Particle volume fraction	Medium	Field strength
Trau – 1995 (Trau, Sankaran et al. 1995)	Barium titanate	100 nm	0.025 vol%	Castor oil	DC: 0.05 V/μm
Sapozhnikov – 2003 (Sapozhnikov, Tolmachev et al. 2003)	Bronze spheres	120 (& 40) mm	3 vol%	Ethanol toluene mixture	DC: 0.66 V/μm
Kumar – 2005 (Kumar, Khusid et al. 2005)	poly-alpha olefin spheres	45 to 87 μm	0.5 – 10 vol%	Corn oil	AC: 0.1 to 3 kHz, 1.6 – 5 V/μm
Agarwal – 2009 (Agarwal and Yethiraj 2009)	Silica	800 nm	0.07 – 4 vol%	Water + dimethyl sulfoxide mixture	AC: 1 MHz, 1 V/μm
Hardt – 2020 (Hardt, Hartmann et al. 2020)	DNA	~350 nm (hydrodynamic diameter) (Wang, Sun et al. 2019)	~0.02 vol%	Dextran and polyethylene glycol	DC: 10-30 V, length across which field is applied is not specified
This work	QDs	17 nm (hydrodynamic diameter) (Cao, Chern et al. 2019)	0.0015 – 0.012 vol%	3.125 mM borate buffer	Typical conditions: DC: 0.01 V/μm AC: 500 kHz, 0.01 V/μm

7.3 Overview of study

Here, we find that a nanoparticle suspension exhibits a macroscopic cellular phase when an AC voltage V_{AC} and DC voltage V_{DC} are simultaneously applied, despite using quantum dot (QD) particles with a diameter and volume fraction both at least an order of magnitude smaller than all prior examples of the cellular phase. Indeed, systematic study revealed that the cellular phase only formed in the presence of both V_{DC} and V_{AC} at volume fraction-dependent critical voltages. The complex interactions required to produce a cellular phase in this system include (1) electrochemistry to generate a DC current, (2) electrophoresis to aggregate particles into a 2D arrangement on one electrode, and (3) an instability driven by the long-ranged repulsive and short-ranged attractive EHD flow that nucleates at regions on the electrode with high local field enhancement. Notably, EO and other purely attractive interactions are competitive with the cellular phase and instead drive the system towards a cluster-phase (*i.e*. pearl chaining). This mechanistic explanation was compared to all previous examples of the electrically-mediated cellular phase to identify a set of unifying factors that appear to always be present, namely that the system adopts an effective 2D arrangement and features an in-plane interaction that is short-range attractive and long-range repulsive. This understanding paves the way towards the concerted formation of hierarchical porous structures that may impact fields including energy storage and filtration.(Mukaibo, Wang et al. 2018, VahidMohammadi, Mojtabavi et al. 2019) This work was published in *Soft Matter*. (Rendos, Cao et al. 2022)

7.4 Observation of nanoparticle cellular phase induced by AC and DC field

As a model system for assembly, the quantum dot (QD) suspension described in Section 3.1.5 was pipetted onto indium tin oxide (ITO)-coated glass and covered with a second ITO-coated glass slide to form a fluid cell as shown in Fig. 7.1 (a). The chamber was held together using a 3D printed frame (Fig. 3.3) and positioned under a 5× magnification epifluorescence microscope to observe it while making independent electrical contact to both ITO-coated slides. More details about the fluid cell assembly can be found in Section 3.4.1.

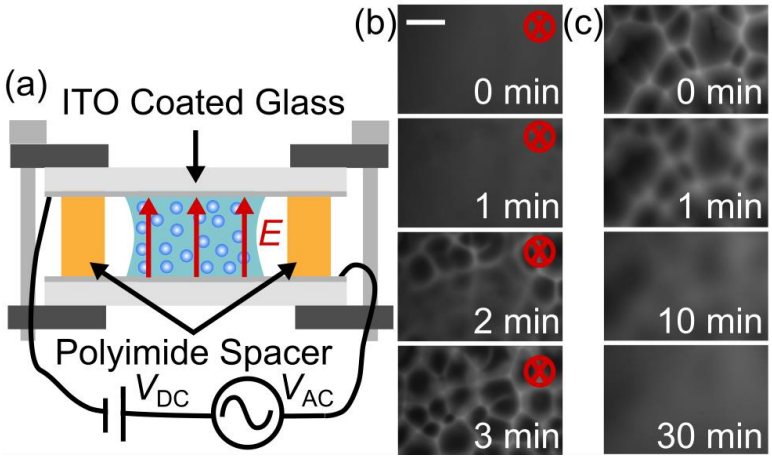

Figure 7.1 (a) Fluid cell consisting of two ITO-coated glass slides separated by a polyimide spacer and containing a suspension of quantum dots (QDs). DC and AC voltages, V_{DC} and V_{AC} respectively, were applied across the fluid cell. (b) Fluorescent micrographs showing the formation of the cellular phase when V_{DC} = 2.2 V and V_{AC} = 2 V were applied to a suspension with volume fraction $\varphi = 6\times10^{-5}$. The scale bar depicts 500 μm. (c) Fluorescent micrographs showing that after V_{DC} and V_{AC} were turned off, the particles diffused back into a homogenous distribution. Reproduced from (Rendos, Cao et al. 2022) with permission from the Royal Society of Chemistry.

Simultaneously applying V_{AC} and V_{DC} across the QD suspension resulted in a cellular phase at strikingly low volume fraction φ, particle size, and field intensities. Specifically, setting

V_{DC} = 2.2 V and V_{AC} = 2 V amplitude at f = 500 kHz, the particles assembled into a cellular phase over the course of a few minutes as shown in Fig. 7.1 (b). To determine whether this process was reversible, the field was subsequently switched off, which led the suspension to gradually homogenize through diffusion, as shown in Fig. 7.1 (c). Additionally, the formation of the cellular phase was reversible over multiple cycles as can be seen in Fig. 7.2 which shows the same fluid cell exhibiting the cellular phase for six on/off cycles.

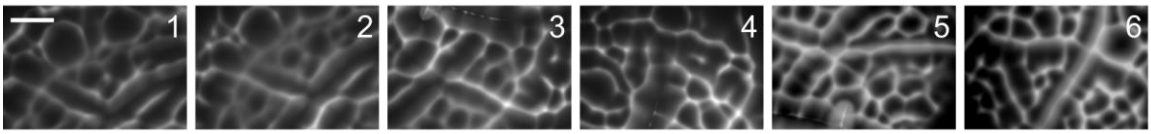

Figure 7.2 Fluorescence micrographs of cellular phase formed at V_{AC} = 2 V and V_{DC} = 2.2 V with QDs at $\varphi = 6\times10^{-5}$ throughout six on/off cycles. The scale bar depicts 500 μm. For each image, the field was applied to the fluid cell, it was allowed to stabilize over the course of 4 min. After each image, the field was switched off for 30 min to allow diffusion to homogenize the particle distribution between trials. It was necessary to store the fluid cell in a 100% relative humidity chamber during the diffusion period to prevent evaporation, so the location on the sample imaged in each cycle was not the same. Reproduced from (Rendos, Cao et al. 2022) with permission from the Royal Society of Chemistry.

Given that this phase has not been previously observed for particles with hydrodynamic diameters < 100 nm, we considered whether this could be specific to these QDs. Thus, we repeated this experiment with two different sizes of commercially available fluorophore-doped polystyrene nanoparticles and again observed the cellular phase (Fig. 7.3), showing that this phase is not restricted to these QDs, or one particular particle size.

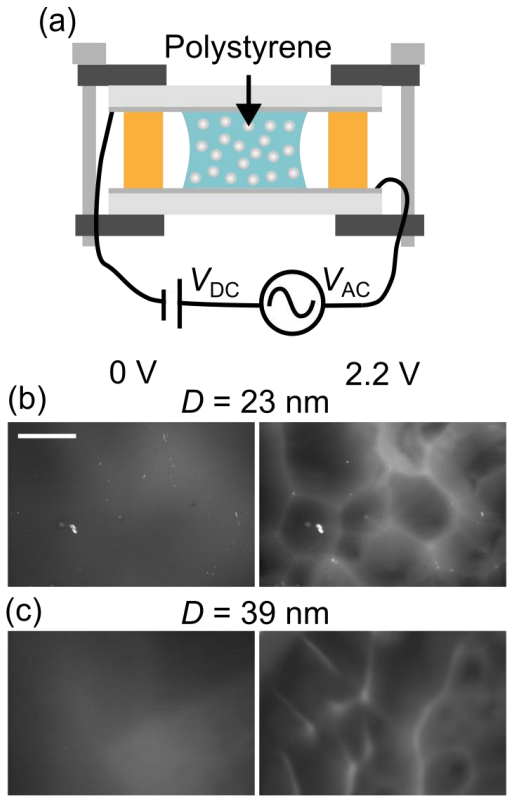

Figure 7.3 (a) Experimental set-up for fluid cell with polystyrene particles. with a diameter of 26 nm at a volume fraction $\varphi = 9\times10^{-5}$. (b) Polystyrene particles with diameter D = 26 nm at a volume fraction $\varphi = 9\times10^{-5}$. (c) Polystyrene particles with D = 39 nm and $\varphi = 1\times10^{-3}$. For both (b) and (c), at the left is a fluorescence micrograph of cell when the field was off and at the right is image of cell after applying AC voltage amplitude V_{AC} = 2 V with frequency f = 500 kHz and turning on DC voltage V_{DC} = 2.2 V for 4 min. Scale bar depicts 500 μm and applies to both (b) and (c). Reproduced from (Rendos, Cao et al. 2022) with permission from the Royal Society of Chemistry.

To explore the mechanism of the cellular phase and determine whether it originated from forces between induced dipoles, we previously computed $\Lambda \sim 0.8$ for this system in Section 2.1.2 which indicated that induced dipole mediated assembly did not occur and that other interactions must have driven the formation of the cellular phase. Another potential mechanism is suggested by the resemblance of the cellular phase to Benárd cells where gravity-driven natural convection from density gradients produces similar cells.(Bergé and Dubois 1984, Eberhard Bodenschatz 2000, Cerisier, Porterie et al. 2005)

Thus, we repeated the experimental conditions shown in Fig. 7.1 with the cell rotated 90° such that gravity pointed along the electrodes and the same cellular structure formed (Fig. 7.4), indicating that natural convection is not responsible for the cellular phase.

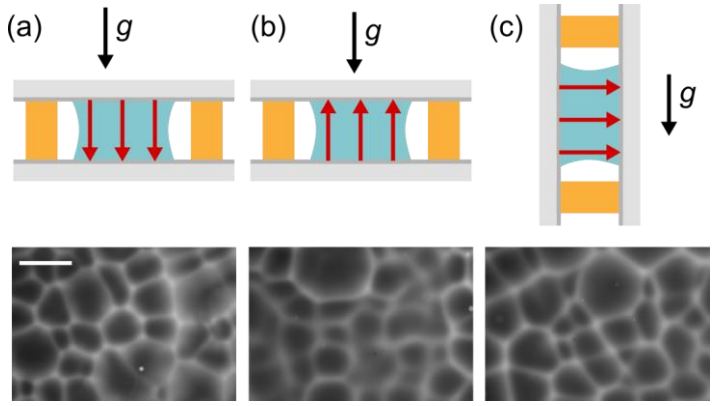

Figure 7.4 Buoyancy experiments performed with the cell in three orientations relative to gravity g: (a) g and applied electric field E in alignment (b) g and E in opposite directions and (c) g and E perpendicular to one another. Each shows a fluorescence micrograph of the cellular phase at V_{AC} = 2 V and V_{DC} = 2.2 V with QDs at $\varphi = 6\times10^{-5}$ where the QDs accumulate on the positive electrode. The scale bar depicts 500 μm. Reproduced from (Rendos, Cao et al. 2022) with permission from the Royal Society of Chemistry.

7.5 Influence of field strength and nanoparticle volume fraction on phase behavior

In order to explore the mechanism of the cellular phase, we examined the contributions of V_{DC} and V_{AC}. Specifically, we performed a series of experiments holding V_{AC} fixed while V_{DC} was incrementally increased from 0 to 2.6 V in steps of 0.2 V. A fluorescence micrograph was taken at each increment after equilibrating for 4 min. The observed gradual transition from a uniform suspension to an ordered cellular phase was apparent and shown in Fig. 7.5 for micrographs of $V_{AC} \geq 1$ V. To analyze these experiments, the fluorescent pattern in each image was manually classified as having (1) a uniform background (no phase) (2) an interconnected series of lines (cellular phase), (3) a series of isolated bright spots (cluster phase) or (4) indeterminate (transition phase). These

classifications for the full series of images are shown in Fig. 7.5, which clearly shows that a minimum V_{DC} of ~1.8 V was required to form the cellular phase.

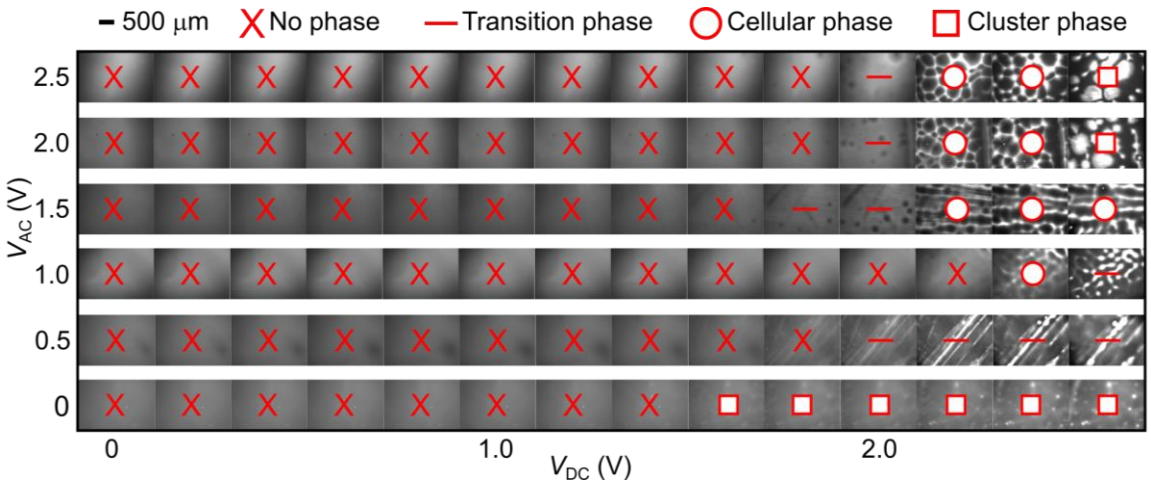

Figure 7.5 Full set of fluorescence micrographs of assembly experiments of QDs at $\varphi = 6\times10^{-5}$ in which V_{AC} was initially set to a value from 0 V to 2.5 V and then V_{DC} was increased from 0 V to 2.6 V in steps of 0.2 V. After each time V_{DC} was increased, the system was allowed to stabilize for 4 min before images were taken. Images are classified as the transition occurs from no phase to either cellular or cluster phase Ambiguous images were classified as transition. Reproduced from (Rendos, Cao et al. 2022) with permission from the Royal Society of Chemistry.

While V_{DC} was required to form the cellular phase, the origin of the ~1.8 V threshold voltage, or the dominant physical effect of V_{DC}, was not clear. The relevance of the DC field is especially noteworthy when one considers that electrolyte ions will accumulate on oppositely charged electrodes, giving rise to an electrode polarization that screens the DC field, thus preventing a strong DC component in the bulk.(Schwan 1968, Ishai, Talary et al. 2013) One process that could maintain a steady-state DC field is a constant flow of ions across the chamber mediated by their electrochemical generation/annihilation at the anode and cathode. Electrochemical reactions at the electrodes could also explain the V_{DC} threshold as highly non-linear currents are common

in electrochemistry due to reaction-specific standard reduction/oxidation potentials and mass transport effects.(Ristenpart, Aksay et al. 2007) To determine whether electrochemical currents were present, two-electrode cyclic voltammetry measurements were conducted on the cell, confirming that electrochemical reactions were present and resulted in an appreciable current when $V_{DC} > 1.5$ V (Fig. 7.6).

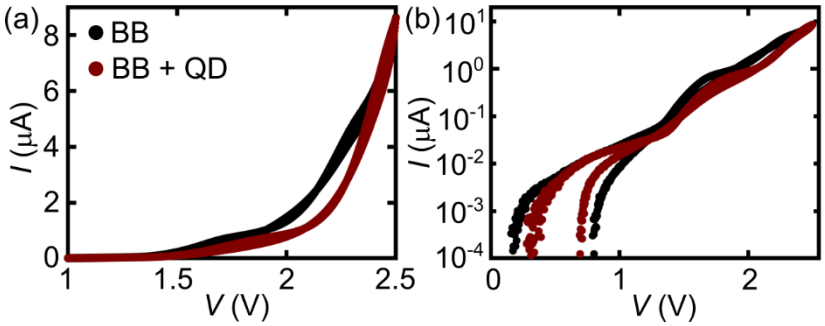

Figure 7.6 Current *I* versus voltage *V* plots from two-electrode cyclic voltammetry electrochemical measurements conducted at a sweep rate of 20 mV/s using the Gamry Reference 600+ Potentiostat/Galvanostat/ZRA on the fluid cell with 3.125 mM borate buffer (BB) solution and QDs in 3.125 mM borate buffer (QD + BB) solution with $\varphi = 6\times10^{-5}$ in (a) linear and (b) log-y scale. Reproduced from (Rendos, Cao et al. 2022) with permission from the Royal Society of Chemistry.

The observed reactions were likely due to a combination of water electrolysis and ITO degradation.(Benck, Pinaud et al. 2014, Simon Geiger 2018) While the current turn-on behavior was commensurate with the onset of the cellular phase, we sought to establish a more definitive link between electrochemical reactions on the electrodes and the cellular phase. Thus, we coated the surface of the ITO electrodes with an insulating layer of poly(methyl methacrylate) (PMMA) to prevent electrochemical reactions from occurring and repeated the assembly experiment. After this treatment, the cellular phase did not form at any voltage (Fig. 7.7), verifying that electrochemistry was required for the cellular phase to form.

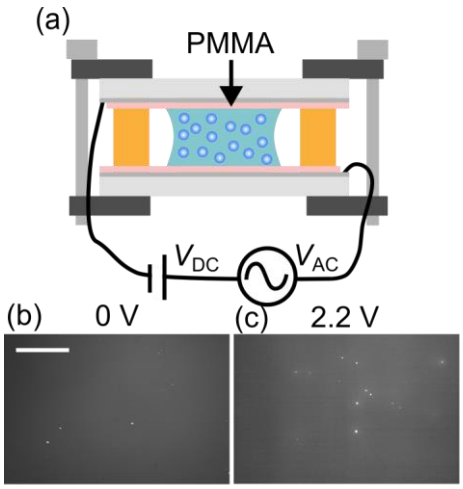

Figure 7.7 (a) Experimental set-up for fluid cell with polymethylmethacrylate (PMMA) coated ITO glass slides made by spin-coating PMMA (molecular weight = 950 kg/mol, diluted to 6% solids weight) onto both ITO glass slides and then baking them on a hot plate for 2 min at 100 ℃. (b) Images of top view when field was off with $\varphi = 6\times10^{-5}$. The scale bar depicts 500 μm. (c) Image after applying V_{AC} = 2 V and turning on V_{DC} for 4 min. Reproduced from (Rendos, Cao et al. 2022) with permission from the Royal Society of Chemistry.

7.6 The role of interparticle interactions in driving spinodal decomposition into the cellular phase as determined by a Cahn-Hilliard analysis

Due to the electrochemical reactions at the electrodes, a steady-state DC field persisted in the chamber and led to electrophoresis of the QDs and a subsequent increase in their local concentration on one electrode. Since these QDs had a slightly negative zeta potential,(Lewinski, Zhu et al. 2010) they will accumulate on the positively charged electrode and form a thin particle-dense film, calculated to be about a monolayer in thickness. In order to determine whether the particles were electrophoretically active, we conducted an experiment with electrodes spaced 1.4 mm apart and imaged the behavior at *V*DC = 4 V from the side of the cell which confirmed the expected movement of the particle to the positive electrode (Fig. 7.8).

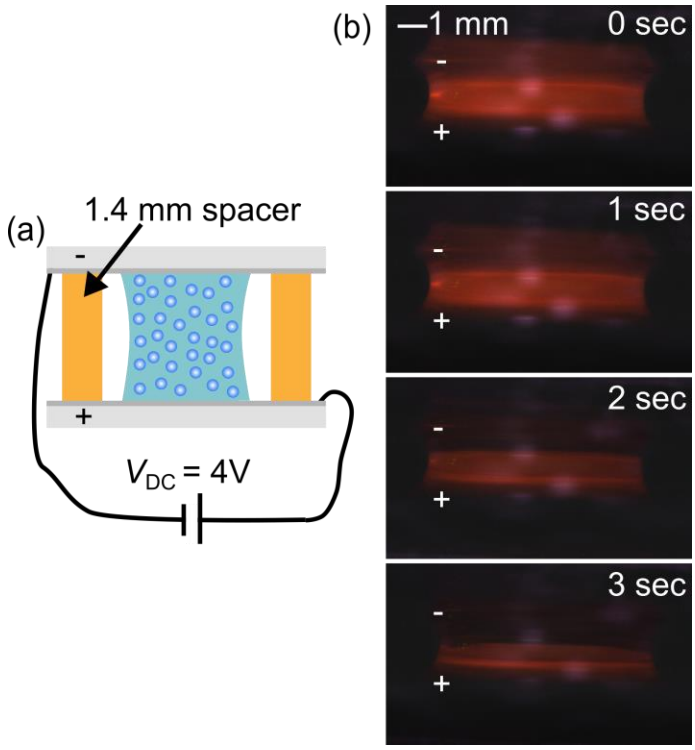

Figure 7.8 (a) Schematic of large fluid cell with 1.4 mm spacer which was used in order to image the quantum dot suspension from the side. In this experiment, V_{DC} = 4 V in order to maintain a similar DC electric field compared to the typical fluid cell. (b) Images of the quantum dot suspension between the negative and positive electrodes as the particles move to the positive electrode over the course of a few seconds. Reproduced from (Rendos, Cao et al. 2022) with permission from the Royal Society of Chemistry.

To understand the fate of this initially uniform film, it is useful to consider that the magnitude of V_{AC} determines whether it will adopt a cellular or cluster phase, as shown in Fig. 7.5. Particles on a substrate will interact through two types of electrically-induced fluid flows: EO flow and EHD flow.(Ristenpart, Aksay et al. 2007, Ristenpart, Aksay et al. 2007, Gencoglu, Olney et al. 2013) While EO flow is a DC phenomenon, EHD flows arise from both V_{AC} and V_{DC}.(Ristenpart, Aksay et al. 2007, Ristenpart, Aksay et al. 2007) Interestingly, these effects are expected to produce contrasting flow fields in which EO draws particles together in the plane while EHD flow, despite being short-range attractive,

will repel particles at long ranges. While a Cahn-Hilliard analysis of these interactions revealed that both interactions can drive a spinodal decomposition, and will do so in a concentration-dependent manner as described in Section 2.2.1, the instigator of the cellular phase was not clear from this analysis alone.

To determine what interaction drove the spinodal decomposition from a film to the cellular phase, we performed a series of experiments at various φ in which V_{DC} was held constant while V_{AC} was gradually increased. First, we prepared a sample with $\varphi = 3\times10^{-5}$, V_{DC} = 1.9 V, and increased V_{AC} from 0.5 to 5.5 V in steps of 0.5 V. To quantify the critical AC voltage V_{AC}^{*} at which the cellular phase forms, the images were analyzed to count the number N of cells in each image (Fig. 7.9).

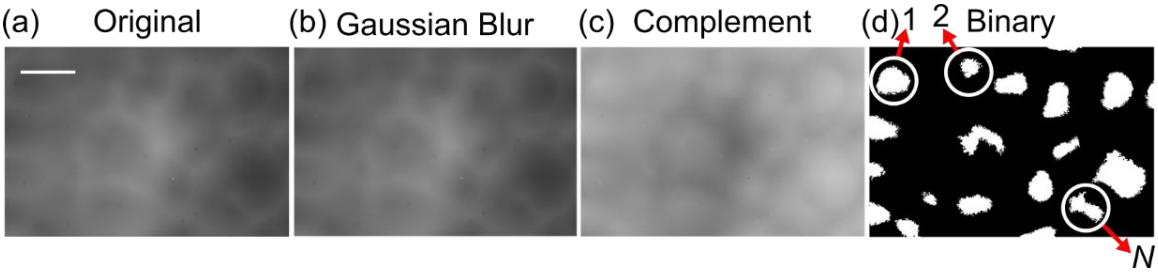

Figure 7.9 (a) Fluorescence microscopy image taken at 5× magnification of QDs with $\varphi = 3\times10^{-5}$, V_{DC} = 1.9 V and V_{AC} = 4 V. The scale bar depicts 500 μm. (b) Image after Gaussian blur was applied. (c) Complement of image, white spots indicate voids in the original image. (d) A binary map of the image enabling identification of the number of cells N. Reproduced from (Rendos, Cao et al. 2022) with permission from the Royal Society of Chemistry.

Then, N vs. V_{AC} was fit to a sigmoid as seen in Fig. 7.10 (a),

$$\frac{N}{N_{max}} = a_1 + \frac{a_2}{1+e^{a_3(V_{AC}-V_{AC}^{*})}}, \tag{7.1}$$

where N_{max} is the maximum number of cells observed in that experiment and a_1, a_2, and a_3 are additional fitting parameters. Eight conditions were tested in triplicate (at four

values of φ and both V_{DC} = 1.9 V and V_{DC} = 2.2 V) over the range of V_{AC}, enabling a Cahn-Hilliard analysis of the cellular phase formation. In this framework, spinodal decomposition is predicted to occur when the interparticle interaction (*i.e*. EO or EHD) leads perturbations to grow faster than they dissipate through diffusion and is outlined in detail in Section 2.2.1. Due to these competing effects, a general relationship is expected wherein the strength of EHD and EO are assigned unknown, but concentration and field independent, pre-factors β_{EHD} and β_{EO}. EHD and EO scale with electric field quadratically and linearly, respectively.(Ristenpart, Aksay et al. 2007) Thus, the data in Fig. 7.10 (b) was fit to,

$$\varphi^{-1} = \beta_{EHD}(V_{AC}^{*} + bV_{DC})^{2} + \beta_{EO}V_{DC}, \tag{7.2}$$

where b reflects that while AC and DC voltages can both give rise to EHD, they may have different intensities.(Ristenpart, Aksay et al. 2007) Using nonlinear least squares fitting, we found β_{EHD} = 0.004 ± 0.001 V^{-2}, b = 9.7 ± 0.8, and β_{EO} = -0.9 ± 0.2 V^{-1}. Critically, since both β_{EHD} and b were positive, this means that EHD promoted the formation of the cellular phase. In contrast, β_{EO} being negative means that EO flow inhibited the cellular phase formation. Interestingly, these results implied that V_{DC} played two competing roles by contributing to both EO and EHD. These results demonstrated that EHD flow was critical to the formation of the cellular phase.

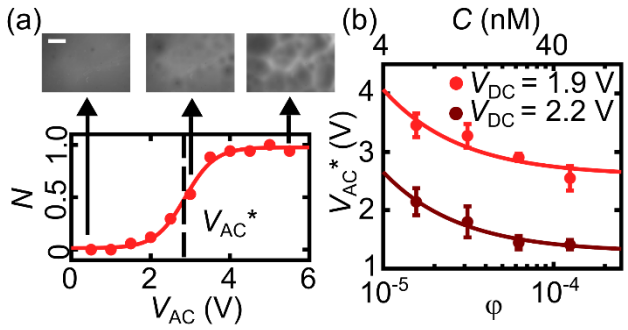

Figure 7.10 (a) Using image processing, the normalized number N of cells for $\varphi = 3\times10^{-5}$ and V_{DC} = 1.9 V vs. V_{AC} are plotted and fit to a Eq. 7.1 to identify the transition voltage V_{AC}^{*}. Representative images displayed with a 500 μm scale bar. (b) V_{AC}^{*} vs. φ and concentration C for V_{DC} = 1.9 and 2.2 V with the lines depicting a single fit to Eq. 7.2. Reproduced from (Rendos, Cao et al. 2022) with permission from the Royal Society of Chemistry.

Given that EHD was identified as an instigator, and EO an inhibitor, of the cellular phase, other features of assembly can be understood by considering where the cells form. Specifically, by performing the assembly experiment with conditions that lead to the cellular phase (V_{DC} = 2.2 V, V_{AC} = 2.0 V, $\varphi = 6\times10^{-5}$), leaving the field off for 40 min to allow the particles to homogenize, and then repeating the same experiment, we found that the structure of the cellular phase was repeatable with voids occurring at the same locations as shown in Fig. 7.11 (a). To explore this further, an experiment was performed where a solution was exposed to conditions that led to a cellular phase (V_{DC} = 2.2 V, V_{AC} = 3.0 V, $\varphi = 6\times10^{-5}$), the system was then allowed to homogenize with the field off, and then exposed to conditions that led to a cluster phase (V_{DC} = 2.4 V, V_{AC} = 0 V). Importantly, Fig. 7.11 (b) showed that many of the cluster phases were co-localized with the centers of the voids of the cellular phase. Together, these results suggested that features of the underlying substrate, likely asperities that enhance local electric field,(Cao and Brown 2021) broke the symmetry of the system and nucleated the phase transition. Furthermore,

the fact that the same location can lead to voids through repulsive EHD flows or clusters through attractive EO flows further suggests that the mode of spinodal decomposition is fundamentally different between EHD- and EO-mediated phases.

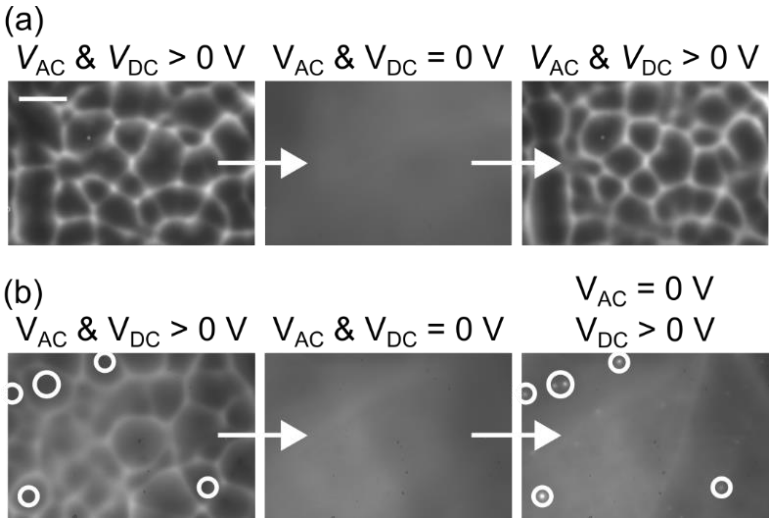

Figure 7.11 (a) From left to right, micrograph of QDs with $\varphi = 6\times10^{-5}$ when V_{DC} = 2.2 V and V_{AC} = 2 V after equilibrating for 4 min, then the field was turned off for 40 min to allow the particles to redistribute, and finally the same voltage was applied for 4 min. Scale bar depicts 500 μm and applies to both (a) and (b). (b) From left to right, micrograph of QDs at $\varphi = 6\times10^{-5}$ after V_{DC} = 2.2 V and V_{AC} = 3 V had been applied for 4 min, micrograph taken after 40 min after the field had been turned off, and then a micrograph taken after V_{DC} = 2.4 V was subsequently applied for 4 min. The location of bright spots where QD concentration is high are indicated by the white circles, these same spots correspond to the location of voids in the left-most micrograph. Reproduced from (Rendos, Cao et al. 2022) with permission from the Royal Society of Chemistry.

These experiments and analysis coalesced into a proposed mechanism for the cellular phase formation involving electrophoresis, EO flow, and EHD flow. Once V_{DC} was applied to the particle suspension, electrochemistry at the electrodes led to a DC current that electrophoretically assembled the particles onto one side of the chamber as shown in Fig. 7.12 (a). Once assembled into a film, EO led to an attractive flow that promoted particle aggregation as shown in Fig. 7.12 (b). However, V_{AC} and V_{DC} also produced an

EHD flow as depicted in Fig. 7.12 (c) that was short-range attractive but repulsive at long ranges. Both flow profiles in Fig. 7.12 (d) were replotted from Ristenpart *et al*.(Ristenpart, Aksay et al. 2007) Depending on which flow dominated, spinodal decomposition in Fig. 7.12 (e) either began through the nucleation of an excess or decrease of particles at the high field regions, which subsequently led to the cluster phase or cellular phase, respectively. This is evident in Fig. 7.10 (a) where small voids of particle-poor areas are seen initially as the cellular phase begins to form. A similar dichotomy of spinodal decompositions has been observed in simulations of colloids with competing interparticle interactions.(Zhao, Misko et al. 2012, Lindquist, Dutta et al. 2017) Interestingly, at V_{DC} > 2.4 V, a transition from a cellular phase to a cluster phase was observed, but this is qualitatively different than the low V_{AC} cluster phase as it occurs at the nodes of the cells. Thus, we attributed this to the vertices of the cells becoming tall enough to span the chamber, at the expense of the structure becoming thinner, at which point particles are recirculated into the voids.

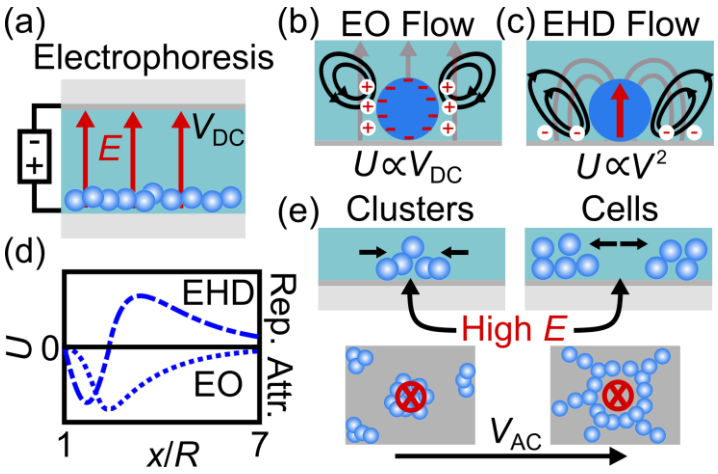

Figure 7.12 Proposed mechanism of cellular phase formation. (a) With application of V_{DC}, electrophoresis moved the QDs to one electrode. (b) Once assembled into a film, electroosmotic (EO) flow produced circulating flows that promote aggregation. (c) Simultaneously, electrohydrodynamic (EHD) flow promoted aggregation at short

distances, but is otherwise repulsive. (d) Flow velocity *U* replotted from Ristenpart *et al*.(Ristenpart, Aksay et al. 2007) vs. distance *x* from a particle of radius *R* for both EO (dotted line) and EHD (dashed line). (e) For small V_{AC}, EO flow dominated and particles aggregated at high field regions causing cluster formation. For larger V_{AC}, EHD dominated and produced voids at the same high field regions, nucleating the cellular phase. Reproduced from (Rendos, Cao et al. 2022) with permission from the Royal Society of Chemistry.

7.7 Control of cellular structure using photolithography

With a greater understanding of the mechanism of the cellular formation, we hypothesized that the cell arrangement could be controlled. Having shown that a polymer coating prevented the formation of the cellular phase, we reasoned that photoresist could serve as a patternable coating to localize assembly. To test this, we patterned a star on the ITO slide connected to the positive lead and performed an assembly experiment. After applying V_{AC} = 2 V and V_{DC} = 2.2 V for 4 min, the cellular structure formed with cells only present centered at the points of the star (Fig. 7.13). Interestingly, this simple method allowed for the location and orientation of five cells to be controlled, suggesting further opportunities for crafting complex macro-porous arrangements with very low particle densities.

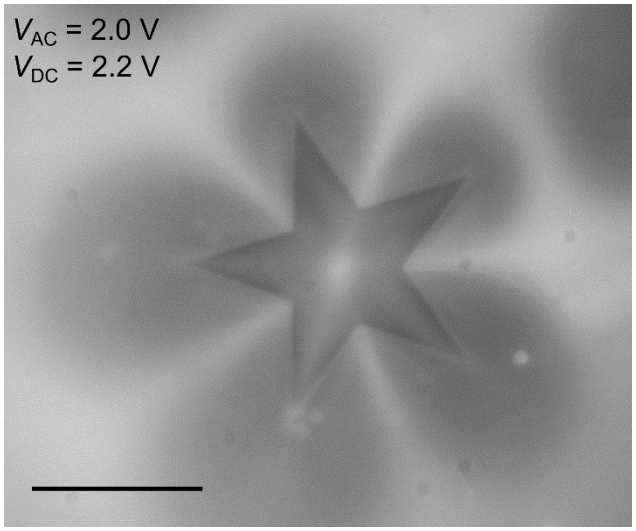

Figure 7.13 Fluorescence micrograph of cells formed at the points of the star pattern where the star is the exposed ITO and the rest is covered with photoresist. Here, V_{AC} = 2.0 V, V_{DC} = 2.2 V, and $\varphi = 6\times10^{-5}$. The scale bar depicts 500 μm. Reproduced from (Rendos, Cao et al. 2022) with permission from the Royal Society of Chemistry.

7.8 Commonalities in systems that exhibit cellular phase particle assembly

Considering the mechanism of formation identified in the present work and the characteristics of prior work that resulted in the cellular phase, two commonalities emerge that unify all observations of the electrically mediated cellular phase. The first commonality is that each system can be effectively reduced to 2D by way of gravity or V_{DC} pulling particles to one side of the chamber,(Trau, Sankaran et al. 1995, Sapozhnikov, Tolmachev et al. 2003, Hardt, Hartmann et al. 2020) or through the formation of chains spanning the entire chamber.(Kumar, Khusid et al. 2005, Agarwal and Yethiraj 2009) The second commonality is that all feature interactions that are short-range attractive and long-range repulsive in the plane of the electrode, either through dipolar interactions of particle chains or through EHD flow. Indeed, a qualitatively similar cellular phase has been observed in suspensions of magnetic particles under the influence of triaxial magnetic

fields that were effectively 2D systems in which the interaction was short-range attractive and long-range repulsive,(Martin, Venturini et al. 2004, Muller, Osterman et al. 2014, Pham, Zhuang et al. 2017) suggesting that these features can contribute towards a more general and complete understanding of the cellular phase.

7.8 Summary and conclusions

We observed an ultra-low density macroscopic cellular phase through the electrically mediated assembly of nanoparticles that were an order of magnitude smaller than previous examples. Additional control experiments helped tease out the factors that contribute to cellular phase formation such as EO and EHD flows and the importance of electrochemistry at the electrode surface. This interaction between electrochemistry, electrophoresis, EO, and EHD resulted in a unique porous structure made of nanoparticles where the characteristic length of the pores was 10,000 times larger than the size of the particles. Importantly, by comparing to prior work, we identified two characteristics that appear to be required to form the cellular phase: particles that are confined in some way to 2D and an interparticle interaction that is short-range attractive, long-range repulsive. This level of understanding is essential to bridging the gap between observing and utilizing the unique structures produced by this assembly process.

CHAPTER 8: CONCLUSIONS AND FUTURE WORK

8.1 Summary of major results

Smart fluids serve as an excellent testbed to explore the importance of interparticle interactions in particle assembly and were used in this dissertation to understand and tune emergent behavior. Throughout Chapters 4–6, we explored ways to influence the microstructure of MRF with either additives or through functionalization of magnetic particles. In Chapter 4, we developed an MRF formulation that prevented slip of the particle chains through a shear-thickening additive which increased MRF performance by 60%. By considering other methods to reinforce particle chains, we introduced highly anisotropic 2D materials as additives in Chapter 5 which resulted in a 45% increase in performance, but only in a pressure-driven flow at low flow rates due to the interplay of the flow profile with the 2D sheets. Moving into Chapter 6, we predicted that an additional adhesion force between particles due to chemical bonds would improve MRF performance, much like the additives which reinforced the particle chains in Chapters 4 and 5. We found that chemically-linked particle chains enabled up to 40% increase in performance at low particle volume fractions and doubled the stiffness of the particle chains. This large improvement was due to hydrogen bonding between functionalized particles and opens additional avenues of tunability in MRF due to the flexibility of colloidal particle functionalization.

In Chapter 7, we studied a different type of smart fluid, an electrically responsive quantum dot suspension that exhibited an unexpected cellular phase with particle-poor voids and particle-rich walls when an AC and DC field were applied simultaneously. This

system allowed us to study and understand the influence of electroosmotic and electrohydrodynamic flows on the arrangement of electrophoretically assembled particles on an electrode. This particle assembly was found to be mainly mediated by the short-range attractive, long-range repulsive particle interactions induced by electrohydrodynamic flow which nucleated voids at high field regions on the electrode causing spinodal decomposition into the cellular phase. Interestingly, when comparing our system to prior work in which a cellular phase was also observed, we identified two main characteristics needed to produce cellular phase assembly: a two-dimensional configuration and short-range attractive, long-range repulsive particle interactions which were present in all cases. Our system was the first to exhibit the cellular phase of particles with a diameter < 100 nm making it a unique, continuous porous structure with voids 10,000× larger than the size of the particles themselves. We also showed the potential to pattern these porous structures through photolithographic patterns. Overall, we were able to understand and tune the emergent behavior of the cellular phase through careful tuning of the interparticle interactions with the applied electric field.

8.2 Implications for designing smart fluids

The understanding gained throughout Chapters 4-7 resulted in important design rules that can be applied to the design of different classes of smart fluids. Importantly, it is clear from Chapters 4 and 5 that smart fluid performance is highly tunable through the use of various additives, not just the magnetic particles that are the main functional component of the fluid. In terms of designing for a specific application, a user may want to balance yield stress and fluid weight to ensure the fluid is strong, but light. In that case, a shear-

thickening additive may be particularly useful as it could be used to maintain the same yield stress as a conventional MRF with 60% fewer iron particles due to the additive providing 60% improvement in performance. Additionally, Chapter 5 revealed a powerful connection between the type of fluid flow and the success of anisotropic additives. Highly anisotropic 2D sheets reinforced particle chains, but only in a pressure-driven flow. From this observation, it is clear that testing the smart fluid in an applicable flow is essential to understanding how the fluid will behave when in use. This is particularly important when considering that MRF are commonly used in pressure-drive flows as tunable valves despite their characterization nearly always being conducted in the boundary-driven flow of a rheometer. We can apply this understanding when developing formulations for MRF used in soft robots with pressure-driven flows, a very recent application of their tunable properties,(Leps, Glick et al. 2020, McDonald, Rendos et al. 2020) which we have contributed to by producing an MRF formulation capable of producing ~10 kPa pressure difference at a magnetic field strength of 0.02 T and was used to successfully actuate a soft robotic device (Fig. 8.1).(McDonald, Rendos et al. 2020) By carefully choosing smart fluid additives and quantifying fluid performance in an applicable flow, smart fluids can be optimized for specific applications.

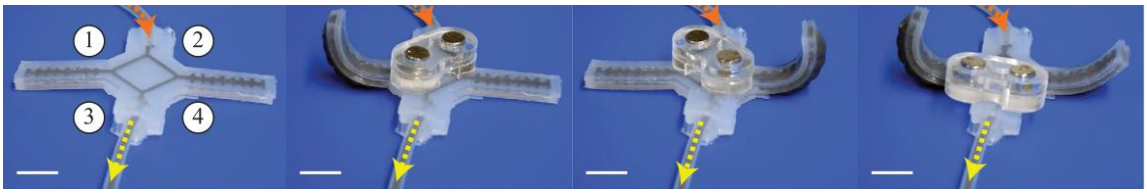

Figure 8.1 Magnetorheological soft robotic actuator reproduced from McDonald *et al.* controlled by permanent magnets.(McDonald, Rendos et al. 2020) Scale bars depict 1 cm and arrows indicate direction of fluid flow.

Within Chapters 4–7, the importance of both experimentation and modeling is highlighted. Modeling guided our understanding of the failure mode in MRF in Chapter 4, the influence of additive length scale in pressure-driven flows in Chapter 5, the contribution of adhesion to particle chain strength in Chapter 6, and finally the onset of spinodal decomposition in the quantum dot suspension in Chapter 7. Not only did simple analytical modeling provide an understanding for the observations made through experiments, but could also allow us to predict the behavior of smart fluids in the future to better guide the design of smart fluids. For example, the spinodal decomposition analysis used in Chapter 7, but described in detail in Chapter 2, can be applied more generally to understand phase behavior in suspensions by interchanging different flow velocities depending on the flow type present. Considering both the microscopic and bulk behavior of smart fluids gives a more complete picture of their behavior and the mechanisms at play.

8.3 Future directions

8.3.1 Multifunctional MRF

Through the studies described in Chapters 4-6, the usefulness of additives and particle functionalization in improving the performance of MRF became apparent. Due to the versatility of colloidal particles, there is a large materials space within which to design field-responsive colloidal materials. Another avenue of research and materials design in the smart fluid space is creating multifunctional smart fluids. Fluids that respond to both magnetic and electric fields, or electro-magneto rheological fluids (EMRF) have been explored to some degree in the literature, but only very to a limited extent and are an exciting space to work within considering the added tunability of these multifunctional

materials.(Hao 2001, Zhurauski, Dragašius et al. 2008, Lee, Noh et al. 2016) Interestingly, the stMRF that contains corn starch could serve as a method of studying the combined effects of electric and magnetic fields since corn starch has commonly been used as the functional component of ERF.(Thurston and Gaertner 1991, Conrad, Li et al. 1995, Yavuz, Tilki et al. 2010) For future study, the pressure-driven flow testing apparatus from Fig. 3.2 could be altered to allow for both electric and magnetic fields to be applied in order to explore this family of materials, test the EMRF in a multi-stimuli mode that is not frequently used in characterizing smart fluids, and study how the alignment of the E and B field affect performance.

Additionally, other external stimuli such as temperature, pH, and light are important in creating multifunctional materials. In Chapter 6, we studied two linked MRF with particles that interacted through hydrogen bonding which strengthened the particle chains. Other bonding schemes could be used in order to provide additional functionality, such as using DNA which is highly programmable. Importantly, DNA has been shown to assemble and link colloidal crystals with bonds that can dehybridize at programmable temperatures,(Senesi, Eichelsdoerfer et al. 2013, Kubiak, Morje et al. 2021) thus providing a methodology to realize dynamic linking and temperature-responsive properties. As such, the understanding gained in Chapter 6 could be used to develop new classes of temperature and field responsive MRF in future work with tunable interparticle interactions.

8.3.2 MRF and MR elastomers for soft robotics

Chapter 5 described a method of testing MRF in a pressure-driven flow, which is particularly relevant to soft robotics as seen in Fig. 8.1. Our work revealed the importance

of the additive length scale in determining the performance of the fluid due to its interaction with the particle chains during flow. The field of soft robotics is actively exploring ways to incorporate magnetically responsive materials into their robot designs due to the advantage provided by having a functional material element.(Bira, Dhagat et al. 2020, Chung, Parsons et al. 2020, Leps, Glick et al. 2020, McDonald, Rendos et al. 2020) Not only are MRF useful in soft robotics, but also magnetorheological elastomers (MRE) that are another class of magnetically responsive materials that exhibit tunable stiffness made by dispersing magnetic particles in an elastomer matrix.(Bastola, Paudel et al. 2020) A potential avenue of future study for designing MR materials for soft robotics is using our extensive background knowledge of the effects of additives on MRF performance to design MRE formulations for soft robotics that exhibit the desired magnetic properties and can also be 3D printed using stereolithography (SLA) printing techniques to take advantage of additive manufacturing techniques that are frequently used in the creation of soft robots. This would require careful experimental testing of viscosity modifiers and additives to realize the desired magnetic and viscoelastic properties, but could be incredibly useful in making materials for soft robotics and other applications of MRE such as tunable vibration controllers and tactile sensors.

8.3.3 Photocrosslinked cellular phase

The cellular phase observed in Chapter 6 is possible because of specific interparticle interactions induced by fluid flow. While the phase is reversible through cyclic application of an electric field, it would be advantageous to solidify this structure in order to not only better understand the 2D nature or cross-sectional structure of the cellular phase,

but also to develop a methodology to designing permanent self-assembled porous structures. Solidifying the cellular phase is an extension of our cellular phase study that could be executed with a photocrosslinkable hydrogel matrix. Using hydrogel materials described by Sen *et al* (Wang, Li et al. 2018) as the medium for particle assembly, the structure could then be crosslinked under UV light. The ability to image cross sections of the cellular phase is an important avenue of future research so that we could investigate ways to further tune the structure. For example, while the volume fraction of particles was low enough that particles could form a monolayer on the electrode, a significant increase in the volume fraction could create 3D structure which would be best understood by imaging from both the top and side of the structure. By exploring methods to control or produce new emergent behaviors in EF, we can better understand the role of interparticle interactions is designing self-assembled materials.

BIBLIOGRAPHY

Agarwal, A. K. and A. Yethiraj (2009). "Low-density ordered phase in brownian dipolar colloidal suspensions." *Physical Review Letters* **102**(19): 198301.

Ahmad, S. (2004). Materials by Design. Futuristic Materials, Allied Publishers Private Limited**:** 76-79.

Almudallal, A. M. and I. Saika-Voivod (2011). "Simulation of a two-dimensional model for colloids in a uniaxial electric field." *Physical Review. E, Statistical, Nonlinear, and Soft Matter Physics* **84**(1 Pt 1): 011402.

Anderson, P. W. (1972). "More is Different." *Science* **177**(4047): 393–396.

Aranson, I. S. (2013). "Active colloids." *Physics-Uspekhi* **56**(1): 79-92.

Ashour, O. N., D. Kinder, V. Giurgiutiu and C. A. Rogers (1997). Manufacturing and characterization of magnetorheological fluids. *Smart Structures and Materials, Proceedings of SPIE***:** 174-184.

Ashtiani, M., S. H. Hashemabadi and A. Ghaffari (2015). "A review on the magnetorheological fluid preparation and stabilization." *Journal of Magnetism and Magnetic Materials* **374**: 716-730.

Asiaban, R., H. Khajehsaeid, E. Ghobadi and M. Jabbari (2020). "New magneto-rheological fluids with high stability: Experimental study and constitutive modelling." *Polymer Testing* **87**: 106512. https://doi.org/10.1016/j.polymertesting.2020.106512

Bastola, A. K., M. Paudel, L. Li and W. Li (2020). "Recent progress of magnetorheological elastomers: a review." *Smart Materials and Structures* **29**(12): 123002. https://doi.org/10.1088/1361-665X/abbc77

Bell, R. C., J. O. Karli, A. N. Vavreck, D. T. Zimmerman, G. T. Ngatu and N. M. Wereley (2008). "Magnetorheology of submicron diameter iron microwires dispersed in silicone oil." *Smart Materials and Structures* **17**(1): 015028. https://doi.org/10.1088/0964-1726/17/01/015028

Belyavskii, S. G., P. G. Mingalyov, F. Giulieri, R. Combarrieau and G. V. Lisichkin (2006). "Chemical modification of the surface of a carbonyl iron powder." *Protection of Metals* **42**(3): 244-252.

Benck, J. D., B. A. Pinaud, Y. Gorlin and T. F. Jaramillo (2014). "Substrate selection for fundamental studies of electrocatalysts and photoelectrodes: inert potential windows in acidic, neutral, and basic electrolyte." *PLoS One* **9**(10): e107942.

Bergé, P. and M. Dubois (1984). "Rayleigh-bénard convection." *Contemporary Physics* **25**(6): 535-582.

Bira, N., P. Dhagat and J. R. Davidson (2020). "A Review of Magnetic Elastomers and Their Role in Soft Robotics." *Frontiers in Robotics and AI* **7**: 588391.

Bird, R. B., G. C. Dai and B. J. Yarusso (1983). "The Rheology and Flow of Viscoplastic Materials." *Reviews in Chemical Engineering* **1**(1): 1–70. https://doi.org/10.1515/revce-1983-0102

Bossis, G., E. Lemaire and O. Volkova (1997). "Yield stress in magnetorheological and electrorheological fluids: A comparison between microscopic and macroscopic structural models." *Journal of Rheology* **41**(3): 687. https://doi.org/10.1122/1.550838

Buck, M. R., J. F. Bondi and R. E. Schaak (2011). "A total-synthesis framework for the construction of high-order colloidal hybrid nanoparticles." *Nature Chemistry* **4**(1): 37-44.

Cao, W. and K. A. Brown (2021). "Theory for hierarchical assembly with dielectrophoresis and the role of particle anisotropy." *Electrophoresis* **42**(5): 635-643.

Cao, W., M. Chern, A. M. Dennis and K. A. Brown (2019). "Measuring Nanoparticle Polarizability Using Fluorescence Microscopy." *Nano Letters* **19**(8): 5762-5768.

Carlson, J. D. (2005). "MR fluids and devices in the real world." *International Journal of Modern Physics B* **19**(7–9): 1463–1470. https://doi.org/10.1142/S0217979205030451

Carlson, J. D. (2016). "What Makes a Good MR Fluid?" *Journal of Intelligent Material Systems and Structures* **13**(7-8): 431-435.

Cerisier, P., B. Porterie, A. Kaiss and J. Cordonnier (2005). "Transport and sedimentation of solid particles in Benard hexagonal cells." *European Physical Journal. Soft Matter* **18**(1): 85-93.

Chen, K., W. L. Zhang, L. Shan, X. Zhang, Y. Meng, H. J. Choi and Y. Tian (2014). "Magnetorheology of suspensions based on graphene oxide coated or added carbonyl iron microspheres and sunflower oil." *Journal of Applied Physics* **116**(15): 153508. https://doi.org/10.1063/1.4898678

Chern, M., T. T. Nguyen, A. H. Mahler and A. M. Dennis (2017). "Shell thickness effects on quantum dot brightness and energy transfer." *Nanoscale* **9**(42): 16446-16458.

Chin, B. D., J. H. Park, M. H. Kwon and O. O. Park (2001). "Rheological properties and dispersion stability of magnetorheological (MR) suspensions." *Rheologica Acta* **40**(3): 211–219.

Chung, H. J., A. M. Parsons and L. Zheng (2020). "Magnetically Controlled Soft Robotics Utilizing Elastomers and Gels in Actuation: A Review." *Advanced Intelligent Systems* **3**(3): 2000186. https://doi.org/10.1002/aisy.202000186

Claracq, J. r. m., J. r. m. Sarrazin and J.-P. Montfort (2004). "Viscoelastic properties of magnetorheological fluids." *Rheologica Acta* **43**(1): 38-49.

Clasen, C. and G. G. McKinely (2004). "Gap-dependent microrheometry of complex liquids." *Journal of Non-Newtonian Fluid Mechanics.* **124**: 1-10.

Conrad, H., Y. Li and Y. Chen (1995). "The temperature dependence of the electrorheology and related electrical properties of corn starch/corn oil suspensions." *Journal of Rheology* **39**(5): 1041-1057.

Coussot, P. (2005). Rheometry of Pastes, Suspensions, and Granular Materials, John Wiley & Sons.

Cvek, M., M. Mrlik, R. Moucka and M. Sedlacik (2018). "A systematical study of the overall influence of carbon allotrope additives on performance, stability and redispersibility of magnetorheological fluids." *Colloids and Surfaces A: Physicochemical and Engineering Aspects* **543**: 83-92.

Davies, G. A. and J. R. Stokes (2008). "Thin film and high shear rheology of multiphase complex fluids." *Journal of Non-Newtonian Fluid Mechanics* **148**(1-3): 73-87.

Davis, L. C. (1992). "Polarization forces and conductivity effects in electrorheological fluids." *Journal of Applied Physics* **72**(4): 1334-1340.

de Vicente, J., D. J. Klingenberg and R. Hidalgo-Alvarez (2011). "Magnetorheological fluids: a review." *Soft Matter* **7**(8): 3701–3710. https://doi.org/10.1039/C0SM01221A

de Vicente, J., F. Vereda, J. P. Segovia-Gutiérrez, M. del Puerto Morales and R. Hidalgo-Álvarez (2010). "Effect of particle shape in magnetorheology." *Journal of Rheology* **54**(6): 1337-1362.

Dickerson, J. H. and A. R. Boccaccini (2012). Electrophoretic Deposition Of Nanomaterials, Springer.

Dickinson, E. (2015). "Colloids in food: ingredients, structure, and stability." *Annual Review of Food Science and Technology* **6**: 211-233.

Dreyfus, R., J. Baudry, M. L. Roper, M. Fermigier, H. A. Stone and J. Bibette (2005). "Microscopic artificial swimmers." *Nature* **437**(7060): 862-865.

Eberhard Bodenschatz, W. P., and Guenter Ahlers (2000). "Recent Developments in Rayleigh-Benard Convection." *Annual Review of Fluid Mechanics* **32**: 709-778.

Eberhardt, J. J., P. J. Hay and J. Joseph A. Carpenter (1985). "Materials by Design - A Hierarchical Approach to the Design of New Materials." *Materials Research Society Symposia Proceedings* **63**: Symposium R – Computer-Based Microscopic Description of the Structure and Properties of Materials. https://doi.org/10.1557/PROC-63-191

Fernández-Toledano, J. C., J. Rodríguez-López, K. Shahrivar, R. Hidalgo-Álvarez, L. Elvira, F. Montero de Espinosa and J. de Vicente (2014). "Two-step yielding in magnetorheology." *Journal of Rheology* **58**(5): 1507-1534.

Ferraro, V. C. A. (1962). Electromagnetic Theory. London, Athlone Press.

Furedi, A. A. and R. C. Valentine (1962). "Factors involved in the orientation of microscopic particles in suspensions influenced by radio frequency fields." *Biochimica et Biophysica Acta* **56**: 33-42.

Gallagher, R., T. Appenzeller, D. Normile and R. F. Service (1999). "Beyond reductionism." *Science* **284**(5411): 79. https://doi.org/10.1126/science.284.5411.79

Geiger, S., O. Kasian, Marc Ledendecker, Enrico Pizzutilo, Andrea Mingers, et al. (2018). "The stability number as a metric for electrocatalyst stability benchmarking." *Nature Catalysis* 1: 508–515. https://doi.org/10.1038/s41929-018-0085-6

Gencoglu, A., D. Olney, A. LaLonde, K. S. Koppula and B. H. Lapizco-Encinas (2013). "Particle Manipulation in Insulator Based Dielectrophoretic Devices." *Journal of Nanotechnology in Engineering and Medicine* **4**(2): 021002. https://doi.org/10.1115/1.4025368

Gerberich, W. W., J. M. Jungk and W. M. Mook (2003). The Bottom-up Approach to Materials by Design. In R.O. Ritchie, M. Sarikaya, and M.A. Meyers (eds.) Nano and Microstructural Design of Advanced Materials. Elsevier Science. https://doi.org/10.1016/B978-0-08-044373-7.X5027-X

Ghaffari, A., S. H. Hashemabadi and M. Ashtiani (2014). "A review on the simulation and modeling of magnetorheological fluids." *Journal of Intelligent Material Systems and Structures* **26**(8): 881-904.

Ginder, J. M. and L. C. Davis (1994). "Shear stresses in magnetorheological fluids: Role of magnetic saturation." *Applied Physics Letters* **65**(26): 3410-3412.

Ginder, J. M., L. C. Davis and L. D. Elie (1996). "Rheology of Magnetorheological Fluids Models and Measurements." *International Journal of Modern Physics B* **10**(23–

24): 3293–3303. https://doi.org/10.1142/S0217979296001744

Glotzer, S. C., M. J. Solomon and N. A. Kotov (2004). "Self-assembly: From nanoscale to microscale colloids." *AIChE Journal* **50**(12): 2978-2985.

Goncalves, F. D., J.-H. Koo and M. Ahmadian (2006). "A review of the state of the art in magnetorheological fluid technologies--Part I: MR fluid and MR fluid models." *The Shock and Vibration Digest* **38**(3): 203+. link.gale.com/apps/doc/A147469827/AONE?u=mlin_b_bumml&sid=googleScholar&xid=216b602a

Guardia, P., A. Labarta and X. Batlle (2011). "Tuning the Size, the Shape, and the Magnetic Properties of Iron Oxide Nanoparticles." *Journal of Physical Chemistry. C* **115**: 390-396.

Han, K., Y. T. Feng and D. R. J. Owen (2010). "Three-dimensional modelling and simulation of magnetorheological fluids." *International Journal for Numerical Methods in Engineering* **84**(11): 1273-1302.

Hao, T. (2001). "Electrorheological Fluids." *Advanced Materials* **13**(24): 1847–1857. https://doi.org/10.1002/1521-4095(200112)13:24%3C1847::AID-ADMA1847%3E3.0.CO;2-A

Hardt, S., J. Hartmann, S. Zhao and A. Bandopadhyay (2020). "Electric-Field-Induced Pattern Formation in Layers of DNA Molecules at the Interface between Two Immiscible Liquids." *Physical Review Letters* **124**(6): 064501.

Hodes, G. (2007). "When Small Is Different: Some Recent Advances in Concepts and Applications of Nanoscale Phenomena." *Advanced Materials* **19**(5): 639-655.

Hong, L., A. Cacciuto, E. Luijten and S. Granick (2006). "Clusters of Charged Janus Spheres." *Nano Letters* **6**(11): 2510–2514. https://doi.org/10.1021/nl061857i

Ishai, P. B., M. S. Talary, A. Caduff, E. Levy and Y. Feldman (2013). "Electrode polarization in dielectric measurements: a review." *Measurement Science and Technology* **24**(10): 102001.

Jia, D., H. Gao, W. Dong, S. Fan, R. Dang and G. Wang (2017). "Hierarchical alpha-Ni(OH)2 Composed of Ultrathin Nanosheets with Controlled Interlayer Distances and Their Enhanced Catalytic Performance." *ACS Applied Materials & Interfaces* **9**(24): 20476-20483.

Jiang, J., G. Hu, Z. Zhang, Y. Meng and Y. Tian (2015). "Stick-slip behavior of magnetorheological fluids in simple linear shearing mode." *Rheologica Acta* **54**(9-10): 859-867.

Jiang, W., Y. Zhang, S. Xuan, C. Guo and X. Gong (2011). "Dimorphic magnetorheological fluid with improved rheological properties." *Journal of Magnetism and Magnetic Materials* **323**(24): 3246-3250.

Jolly, M. R. and J. W. Bender (2006). Field responsive shear thickening fluid. **US Patent. US20060231357A1.**

Jolly, M. R., J. W. Bender and J. D. Carlson (1999). "Properties and Applications of Commercial Magnetorheological Fluids." *Journal of Intelligent Material Systems and Structures* **10**(1): 5–13. https://doi.org/10.1177%2F1045389X9901000102

Jolly, M. R., J. D. Carlson and B. C. Munoz (1996). "A model of the behaviour of magnetorheological materials." *Smart Materials and Structures* **5**(5): 607.

Kang Hyun, S., P. Bong Jun and C. Hyoung Jin (2009). "Effect of Magnetic Nanoparticle Additive on Characteristics of Magnetorheological Fluid." *IEEE Transactions on Magnetics* **45**(10): 4045-4048.

Krauss, G. (2015). Steels: Processing, Structure and Performance. Materials Park, OH, ASM International.

Kubiak, J. M., A. P. Morje, D. J. Lewis, S. L. Wilson and R. J. Macfarlane (2021). "Dynamic Manipulation of DNA-Programmed Crystals Embedded in a Polyelectrolyte Hydrogel." *ACS Applied Materials & Interfaces* **13**(9): 11215-11223.

Kumar, A., B. Khusid, Z. Qiu and A. Acrivos (2005). "New electric-field-driven mesoscale phase transitions in polarized suspensions." *Physical Review Letters* **95**(25): 258301.

Kumar, J. S., P. S. Paul, G. Raghunathan and D. G. Alex (2019). "A review of challenges and solutions in the preparation and use of magnetorheological fluids." *International Journal of Mechanical and Materials Engineering* **14**(1): 13. https://doi.org/10.1186/s40712-019-0109-2

Kuzhir, P., M. T. López-López, G. Vertelov, C. Pradille and G. Bossis (2007). "Shear and squeeze rheometry of suspensions of magnetic polymerized chains." *Rheologica Acta* **47**(2): 179-187.

Landman, U., R. N. Barnett, C. L. Cleveland and H.-P. Cheng (1992). "Small is Different." *International Journal of Modern Physics B* **6**(23–24):3623–3642.

https://doi.org/10.1142/S0217979292001699

Laun, H. M., C. Gabriel and C. Kieburg (2009). "Magnetorheological Fluid in Oscillatory Shear and Parameterization with Regard to MR Device Properties." *Journal of Intelligent Material Systems and Structures* **21**(15): 1479-1489.

Lee, S., J. Noh, S. Hong, Y. K. Kim and J. Jang (2016). "Dual Stimuli-Responsive Smart Fluid of Graphene Oxide-Coated Iron Oxide/Silica Core/Shell Nanoparticles." *Chemistry of Materials* **28**(8): 2624-2633.

Lee, W., A. Chan, M. A. Bevan, J. A. Lewis and P. V. Braun (2004). "Nanoparticle-Mediated Epitaxial Assembly of Colloidal Crystals on Patterned Substrates." *Langmuir* **20**: 5262-5270.

Leps, T., P. E. Glick, D. Ruffatto Iii, A. Parness, M. T. Tolley and C. Hartzell (2020). "A low-power, jamming, magnetorheological valve using electropermanent magnets suitable for distributed control in soft robots." *Smart Materials and Structures* **29**(10): 105025.

Lewinski, N. A., H. Zhu, H.-J. Jo, D. Pham, R. R. Kamath, C. R. Ouyang, C. D. Vulpe, V. L. Colvin and R. A. Drezek (2010). "Quantification of Water Solubilized CdSe/ZnS Quantum Dots in Daphnia magna." *Environmental Science and Technology* **44**: 1841–1846.

Li, W.-J. and T. Fu (2006). "Preparation of movable 3D periodic structures of silica spheres." *Journal of Zhejiang University-SCIENCE A* **7**(S2): 345-349.

Li, W. H., H. Du, G. Chen, S. H. Yeo and N. Guo (2002). "Nonlinear viscoelastic properties of MR fluids under large-amplitude-oscillatory-shear." *Rheologica Acta* **42**(3): 280-286.

Li, W. H., P. Q. Zhang, X. L. Gong and P. B. Kosasih (2005). "Linear Viscoelasticity of MR Fluids: Dependence on Magnetic Fields." *International Journal of Modern Physics B* **19**(7–9): 1198–1204. https://doi.org/10.1142/S0217979205030062

Li, Z., F. Yang and Y. Yin (2019). "Smart Materials by Nanoscale Magnetic Assembly." *Advanced Functional Materials* **30**(2): 1903467. https://doi.org/10.1002/adfm.201903467

Lin, N. Y., X. Cheng and I. Cohen (2014). "Biaxial shear of confined colloidal hard spheres: the structure and rheology of the vorticity-aligned string phase." *Soft Matter* **10**(12): 1969-1976.

Lin, X.-G., F. Guo, C.-B. Du and G.-J. Yu (2018). "The Mechanical Properties of a Novel STMR Damper Based on Magnetorheological Silly Putty." *Advances in Materials Science and Engineering* **2018**: 1-15.

Lindquist, B. A., S. Dutta, R. B. Jadrich, D. J. Milliron and T. M. Truskett (2017). "Interactions and design rules for assembly of porous colloidal mesophases." *Soft Matter* **13**(7): 1335-1343.

López-López, M. T., G. Vertelov, G. Bossis, P. Kuzhir and J. D. G. Durán (2007). "New magnetorheological fluids based on magnetic fibers." *Journal of Materials Chemistry* **17**(36): 3839–3844. https://doi.org/10.1039/B705871C

Lu, Z. and Y. Yin (2012). "Colloidal nanoparticle clusters: functional materials by design." *Chemical Society Reviews* **41**(21): 6874-6887.

Mahendra, S., H. Zhu, V. L. Colvin and P. J. Alvarez (2008). "Quantum Dot Weathering Results in Microbial Toxicity." *Environmental Science & Technology* **42**(24): 9424–9430. https://doi.org/10.1021/es8023385

Manzoor, M. T., J. E. Kim, J. H. Jung, C. Han, S. B. Choi and I. K. Oh (2018). "Two-Dimensional rGO-MoS2 Hybrid Additives for High-Performance Magnetorheological Fluid." *Scientific Reports* **8**(1): 12672.

Mardles, E. W. J. (1940). "Viscosity of Suspensions and the Einstein Equation." *Nature* **145**: 970.

Martin, J. E., E. Venturini, G. L. Gulley and J. Williamson (2004). "Using triaxial magnetic fields to create high susceptibility particle composites." *Physical Review. E, Statistical, Nonlinear, and Soft Matter Physics* **69**(2 Pt 1): 021508.

McDonald, K., A. Rendos, S. Woodman, K. A. Brown and T. Ranzani (2020). "Magnetorheological Fluid-Based Flow Control for Soft Robots." *Advanced Intelligent Systems* **2**(11): 2000139. https://doi.org/10.1002/aisy.202000139

Meeker, S. P., R. T. Bonnecaze and M. Cloitre (2004). "Slip and flow in pastes of soft particles: Direct observation and rheology." *Journal of Rheology* **48**(6): 1295-1320.

Montemayor, L., V. Chernow and J. R. Greer (2015). "Materials by design: Using architecture in material design to reach new property spaces." *MRS Bulletin* **40**(12): 1122-1129.

Morillas, J. R. and J. de Vicente (2019). "On the yield stress in magnetorheological fluids: A direct comparison between 3D simulations and experiments." *Composites Part B: Engineering* **160**: 626-631.

Mueller, S., E. W. Llewellin and H. M. Mader (2009). "The rheology of suspensions of solid particles." *Proceedings of the Royal Society A: Mathematical, Physical and Engineering Sciences* **466**(2116): 1201-1228.

Mukaibo, H., T. Wang, V. H. Perez-Gonzalez, J. Getpreecharsawas, J. Wurzer, B. H. Lapizco-Encinas and J. L. McGrath (2018). "Ultrathin nanoporous membranes for insulator-based dielectrophoresis." *Nanotechnology* **29**(23): 235704.

Muller, K., N. Osterman, D. Babic, C. N. Likos, J. Dobnikar and A. Nikoubashman (2014). "Pattern formation and coarse-graining in two-dimensional colloids driven by multiaxial magnetic fields." *Langmuir* **30**(18): 5088-5096.

Nasilowski, M., P. Spinicelli, G. Patriarche and B. Dubertret (2015). "Gradient CdSe/CdS Quantum Dots with Room Temperature Biexciton Unity Quantum Yield." *Nano Letters* **15**(6): 3953-3958.

Nelson, A. Z. and R. H. Ewoldt (2017). "Design of yield-stress fluids: a rheology-to-structure inverse problem." *Soft Matter* **13**(41): 7578-7594.

Nelson, E. C. and P. V. Braun (2007). "Enhancing Colloids Through the Surface." *Science* **318**(5852): 924–925. https://doi.org/10.1126/science.1148009

Newman, R. C. (1982). "Defects in Silicon." *Reports on Progress in Physics* **45**: 1163. https://doi.org/10.1088/0034-4885/45/10/003

Ngatu, G. T., N. M. Wereley, J. O. Karli and R. C. Bell (2008). "Dimorphic magnetorheological fluids: exploiting partial substitution of microspheres by nanowires." *Smart Materials and Structures* **17**(4): 045022.

Ocalan, M. and G. H. McKinley (2012). "Rheology and microstructural evolution in pressure-driven flow of a magnetorheological fluid with strong particle–wall interactions." *Journal of Intelligent Material Systems and Structures* **23**(9): 969-978.

Olson, G. B. (2000). "Designing a New Material World." *Science* **288**(5468): 993–998. https://doi.org/10.1126/science.288.5468.993

Othmani, M., A. Aissa, C. G. Bac, F. Rachdi and M. Debbabi (2013). "Surface modification of calcium hydroxyapatite by grafting of etidronic acid." *Applied Surface Science* **274**: 151-157.

Park, J. S. and D. Saintillan (2011). "Electric-field-induced ordering and pattern formation in colloidal suspensions." *Physical Review. E, Statistical, Nonlinear, and Soft Matter Physics* **83**(4 Pt 1): 041409.

Patel, R. (2011). "Mechanism of chain formation in nanofluid based MR fluids." *Journal of Magnetism and Magnetic Materials* **323**(10): 1360-1363.

Peng, G. R., W. Li, T. F. Tian, J. Ding and M. Nakano (2014). "Experimental and modeling study of viscoelastic behaviors of magneto-rheological shear thickening fluids." *Korea-Australia Rheology Journal* **26**(2): 149-158.

Pham, A. T., Y. Zhuang, P. Detwiler, J. E. S. Socolar, P. Charbonneau and B. B. Yellen (2017). "Phase diagram and aggregation dynamics of a monolayer of paramagnetic colloids." *Physical Review E* **95**(5-1): 052607.

Pietronero, L. (2008). "Complexity ideas from condensed matter and statistical physics." *Europhysics News* **39**(6): 26-29.

Pu, H. and F. Jiang (2005). "Towards high sedimentation stability: magnetorheological fluids based on CNT/Fe3O4nanocomposites." *Nanotechnology* **16**(9): 1486-1489.

Rendos, A., W. Cao, M. Chern, M. Lauricella, S. Succi, J. G. Werner, A. M. Dennis and K. A. Brown (2022). "Electric field induced macroscopic cellular phase of nanoparticles." *Soft Matter*, Advance Article.

Rendos, A., R. Li, S. Woodman, X. Ling and K. A. Brown (2020). "Reinforcing Magnetorheological Fluids with Highly Anisotropic 2D Materials." *ChemPhysChem* **22**(5): 435–440. https://doi.org/10.1002/cphc.202000948

Rendos, A., S. Woodman, K. McDonald, T. Ranzani and K. A. Brown (2020). "Shear thickening prevents slip in magnetorheological fluids." *Smart Materials and Structures* **29**(7): 07LT02. doi:10.1088/1361-665X/ab8b2e

Ristenpart, W. D., I. A. Aksay and D. A. Saville (2007). "Electrically Driven Flow near a Colloidal Particle Close to an Electrode with a Faradaic Current." *Langmuir* **23**: 4071-4080.

Ristenpart, W. D., I. A. Aksay and D. A. Saville (2007). "Electrohydrodynamic flow around a colloidal particle near an electrode with an oscillating potential." *Journal of Fluid Mechanics* **575**: 83-109.

Rodriguez-Lopez, J., P. Castro, L. Elvira and F. Montero de Espinosa (2015). "Study of the effect of particle volume fraction on the microstructure of magnetorheological fluids using ultrasound: Transition between the strong-link to the weak-link regimes." *Ultrasonics* **61**: 10-14.

Rosensweig, R. E. (1985). Ferrohydrodynamics, Cambridge University Press.

Sacanna, S., D. J. Pine and G.-R. Yi (2013). "Engineering shape: the novel geometries of colloidal self-assembly." *Soft Matter* **9**(34): 8096–8106. https://doi.org/10.1039/C3SM50500F

Samouhos, S. and G. McKinley (2007). "Carbon Nanotube–Magnetite Composites, With Applications to Developing Unique Magnetorheological Fluids." *Journal of Fluids Engineering* **129**(4): 429-437.

Santos, P. J. and R. J. Macfarlane (2020). "Reinforcing Supramolecular Bonding with Magnetic Dipole Interactions to Assemble Dynamic Nanoparticle Superlattices." *Journal of the American Chemical Society* **142**(3): 1170-1174.

Sapozhnikov, M. V., Y. V. Tolmachev, I. S. Aranson and W. K. Kwok (2003). "Dynamic self-assembly and patterns in electrostatically driven granular media." *Physical Review Letters* **90**(11): 114301.

Schwan, H. P. (1968). "Electrode Polarization Impedance and Measurements in Biological Materials." *Annals of the New York Academy of Sciences* **148**(1): 191–209. https://doi.org/10.1111/j.1749-6632.1968.tb20349.x

Senesi, A. J., D. J. Eichelsdoerfer, R. J. Macfarlane, M. R. Jones, E. Auyeung, B. Lee and C. A. Mirkin (2013). "Stepwise evolution of DNA-programmable nanoparticle superlattices." *Angewandte Chemie International Edition in English* **52**(26): 6624-6628.

Shah, K. and S.-B. Choi (2014). "The Field-Dependent Rheological Properties of Magnetorheological Fluids Featuring Plate-Like Iron Particles." *Frontiers in Materials* **1:** 21. https://doi.org/10.3389/fmats.2014.00021

Sherman, S. G. (2016). Magnetorheological fluid dynamics for high speed energy absorbers. Doctoral dissertation, University of Maryland.

Si, H., X. Peng and X. Li (2007). "A Micromechanical Model for Magnetorheological Fluids." *Journal of Intelligent Material Systems and Structures* **19**(1): 19-23.

Spagnolie, S. E. (2015). Complex Fluids In Biological Systems, Springer.

Stocker, T. (2011). Introduction to Climate Modelling, Springer.

Sumpter, B. G., R. K. Vasudevan, T. Potok and S. V. Kalinin (2015). "A bridge for accelerating materials by design." *NPJ Computational Materials* **1**(1): 15008. https://doi.org/10.1038/npjcompumats.2015.8

Sun, S., X. Tang, J. Yang, D. Ning, H. Du, S. Zhang and W. Li (2019). "A New Generation of Magnetorheological Vehicle Suspension System With Tunable Stiffness and Damping Characteristics." *IEEE Transactions on Industrial Informatics* **15**(8): 4696-4708.

Tang, X. and H. Conrad (2000). "An Analytical Model for Magnetorheological Fluids." *Journal of Physics D: Applied Physics* **33**(23): 3026. https://iopscience.iop.org/article/10.1088/0022-3727/33/23/304/pdf

Tao, R. (2001). "Super-strong magnetorheological fluids." *Journal of Physics: Condensed Matter* **13**(50): R979–R999.

Thurston, G. B. and E. B. Gaertner (1991). "Viscoelasticity of electrorheological fluids during oscillatory flow in a rectangular channel." *Journal of Rheology* **35**(7): 1327-1343.

Tian, T. and M. Nakano (2017). "Design and testing of a rotational brake with shear thickening fluids." *Smart Materials and Structures* **26**(3): 035038. https://doi.org/10.1088/1361-665X/aa5a2c.

Tiribocchi, A., A. Montessori, M. Lauricella, F. Bonaccorso, K. A. Brown and S. Succi (2021). "Microscale modelling of dielectrophoresis assembly processes." *Philosophical Transactions of the Royal Society A* **379**(2208): 20200407. https://doi.org/10.1098/rsta.2020.0407

Trappe, V., V. Prasad, L. Cipelletti, P. N. Segre and D. A. Weitz (2001). "Jamming phase diagram for attractive particles." *Nature* **411**: 772–775.

Trau, M., S. Sankaran, D. A. Saville and I. A. Aksay (1995). "Electric-field-induced pattern formation in colloidal dispersions." *Nature* **374**: 437–439.

VahidMohammadi, A., M. Mojtabavi, N. M. Caffrey, M. Wanunu and M. Beidaghi (2019). "Assembling 2D MXenes into Highly Stable Pseudocapacitive Electrodes with High Power and Energy Densities." *Advanced Materials* **31**(8): e1806931.

Vinod, S., R. John and J. Philip (2017). "Magnetorheological properties of sodium sulphonate capped electrolytic iron based MR fluid: a comparison with CI based MR fluid." *Smart Materials and Structures* **26**(2): 025003.

Wang, B., D. Sun, C. Zhang, K. Wang and J. Bai (2019). "Dark-field microscopy for characterization of single molecule dynamicsin vitroandin vivo." *Analytical Methods* **11**(21): 2778-2784.

Wang, G., Y. Ma, G. Cui, N. Li and X. Dong (2018). "Two-dimensional Fe3O4/MoS2 nanocomposites for a magnetorheological fluid with enhanced sedimentation stability." *Soft Matter* **14**(10): 1917-1924.

Wang, G., F. Zhou, Z. Lu, Y. Ma, X. Li, Y. Tong and X. Dong (2019). "Controlled synthesis of CoFe2O4/MoS2 nanocomposites with excellent sedimentation stability for magnetorheological fluid." *Journal of Industrial and Engineering Chemistry* **70**: 439-446.

Wang, S., L. Li, D. Su, K. Robin and K. A. Brown (2018). "Patterning Porosity in Hydrogels by Arresting Phase Separation." *ACS Applied Materials & Interfaces* **10**(40): 34604-34610.

Wang, X. and F. Gordaninejad (2006). "Study of magnetorheological fluids at high shear rates." *Rheologica Acta* **45**(6): 899-908.

Wang, Y., S. Wang, C. Xu, S. Xuan, W. Jiang and X. Gong (2016). "Dynamic behavior of magnetically responsive shear-stiffening gel under high strain rate." *Composites Science and Technology* **127**: 169-176.

Weiss, K. D., T. G. Duclos, J. D. Carlson, M. J. Chrzan and A. J. Margida (1993). High Strength Magneto- and Electro-rheological Fluids, SAE International.

Wereley, N. M., A. Chaudhuri, J. H. Yoo, S. John, S. Kotha, A. Suggs, R. Radhakrishnan, B. J. Love and T. S. Sudarshan (2006). "Bidisperse Magnetorheological Fluids using Fe Particles at Nanometer and Micron Scale." *Journal of Intelligent Material Systems and Structures* **17**(5): 393-401.

Whiteley, J., F. Gordaninejad and X. Wang (2010). "Magnetorheological Fluid Flow in Microchannels." *Journal of Applied Mechanics* **77**(4): 041011. https://doi.org/10.1115/1.4000922

Wu, W. P., B. Y. Zhao, Q. Wu, L. S. Chen and K. A. Hu (2006). "The strengthening effect of guar gum on the yield stress of magnetorheological fluid." *Smart Materials and Structures* **15**(4): N94-N98.

Xu, Z.-D., M. Xu and C.-L. Sun (2018). "Performance Tests and Microchain Model Validation of a Novel Kind of MR Fluid with GO-Coated Iron Particles." *Journal of Materials in Civil Engineering* **30**(5). https://doi.org/10.1061/(ASCE)MT.1943-5533.0002253

Yang, P., M. Yu, J. Fu and H. Luo (2017). "Rheological properties of dimorphic magnetorheological gels mixed dendritic carbonyl iron powder." *Journal of Intelligent Material Systems and Structures* **29**(1): 12-23.

Yavuz, M., T. Tilki, C. Karabacak, O. Erol, H. Ibrahim Unal, M. Uluturk and M. Cabuk (2010). "Electrorheological behavior of biodegradable modified corn starch/corn oil suspensions." *Carbohydrate Polymers* **79**(2): 318-324.

Zhang, W. L. and H. J. Choi (2012). "Graphene oxide added carbonyl iron microsphere system and its magnetorheology under applied magnetic fields." *Journal of Applied Physics* **111**(7): 07E724. https://doi.org/10.1063/1.3677671

Zhang, W. L. and H. J. Choi (2014). "Graphene oxide based smart fluids." *Soft Matter* **10**(35): 6601-6608.

Zhang, X., W. Li and X. Gong (2010). "Thixotropy of MR shear-thickening fluids." *Smart Materials and Structures* **19**(12).

Zhang, X., W. Li and X. L. Gong (2008). "Study on magnetorheological shear thickening fluid." *Smart Materials and Structures* **17**(1).

Zhao, H. J., V. R. Misko and F. M. Peeters (2012). "Analysis of pattern formation in systems with competing range interactions." *New Journal of Physics* **14**(6): 063032. https://iopscience.iop.org/article/10.1088/1367-2630/14/6/063032/pdf

Zhao, P.-h., Y.-z. Fu, H.-l. Li, C.-y. Zhang and Y.-q. Liu (2019). "Three-dimensional simulation study on the aggregation behavior and shear properties of magnetorheological fluid." *Chemical Physics Letters* **722**: 74-79.

Zhurauski, M. A., E. Dragašius, E. V. Korobko and Z. A. Novikova (2008). "Mechanical properties of smart fluids under combined electrical and magnetic fields." *Mechanika* **74**(6). https://mechanika.ktu.lt/index.php/Mech/article/view/15170/7803

CURRICULUM VITAE